Disentangling the photophysics of ionized biomolecules in microsolvated environments

Dissertation
zur Erlangung des Doktorgrades
an der Fakultät für Mathematik, Informatik und Naturwissenschaften
Fachbereich Physik
der Universität Hamburg

vorgelegt von
Melby Johny
melby.johny@cfel.de

Hamburg
2020

Gutachter der Dissertation: Prof. Dr. Jochen Küpper
Prof. Dr. Giuseppe Sansone

Zusammensetzung der Prüfungskommission: Prof. Dr. Jochen Küpper
Prof. Dr. Giuseppe Sansone
Prof. Dr. Francesca Calegari
Prof. Dr. Ulrike Frühling
Prof. Dr. Daniela Pfannkuche

Vorsitzende/r der Prüfungskommission: Prof. Dr. Daniela Pfannkuche
Datum der Disputation: 24.11.2020
Datum der Freigabe: 04.12.2020
Vorsitzender Fach-Promotionsausschusses Physik: Prof. Dr. Wolfgang Hansen
Leiter des Fachbereichs Physik: Prof. Dr. Michael Potthoff
Dekan der Fakultät MIN: Prof. Dr. Heinrich Graener

Abstract

Water is vital for the existence of life on earth, and therefore, it is dubbed as the matrix of life. Furthermore, the hydration environment plays diverse functional, structural, and dynamic roles in molecular cell biology. For instance, the photophysical and photochemical properties of UV absorbing chromophores found in biological systems are sensitive to their local solvation environment. In hydrated systems, the hydrogen-bond network between the chromophores and surrounding water molecules can provide additional relaxation pathways after excitation or ionization of chromophores, crucial for the photostability of the biological system. On the other hand, the abundant solvent environment around biological matter can enhance radiation-induced damage through, e. g., the radiolysis of water. Despite the huge efforts to unravel realistic dynamics, the role of the hydration environment upon the radiation-induced biological damage remains elusive. In the framework of this thesis, a bottom-up approach is used to systematically investigate the role of a single water molecule in the photophysics of a model chromophore, pyrrole, after ionization. This work can be divided into two main parts: the preparation of pure samples of pyrrole and microsolvated pyrrole(H_2O) in the gas phase, and a comparative photophysics investigation on these model systems utilizing time- and position- sensitive detectors.

The preparation of pure and rotationally cold samples of pyrrole and pyrrole(H_2O) is achieved using a combination of a cold molecular beam and the electrostatic deflector. A knife-edge for shaping a molecular beam is implemented to improve the spatial separation of the species in a molecular beam by the electrostatic deflector as well as to reduce the contribution of atomic seed gas in the interaction zone. A pyrrole(H_2O) cluster beam with unprecedented purity of ~100 % is obtained. The extracted rotational temperature of pyrrole and pyrrole(H_2O) after the supersonic expansion is $T_{\text{rot}} = 0.8 \pm 0.2$ K. Also, the number densities and rotational temperature of the cluster beam is significantly improved.

In the photophysics investigation part, we mimicked radiation damage in pyrrole and pyrrole(H_2O), after outer valence- and inner-shell ionization through strong-field ionization and site-specific x-ray ionization, respectively. In the strong-field case, single- and double-ionization of bare pyrrole resulted in fragmentation of the aromatic ring through breaking the C–C or N–C covalent bonds. Albeit, the protective effects in the cluster, a weak enhanced strong-field ionization resulting in the formation of highly charged ionic species is observed only for the pyrrole(H_2O) cluster. In the case of site-specific core-shell ionization, the fragmentation studies on bare pyrrole yielded similar channels as compared to the strong-field ionization scenario. For pyrrole(H_2O), performing a localized x-ray ionization at the aromatic ring resulted in charge- and mass-transfer across the hydrogen-bond. Overall, a hydrogen-bonded single water molecule can facilitate radiation-protection pathways after outer valence- and inner-shell ionization of biomolecules.

Zusammenfassung

Wasser ist essentiell für die Existenz von Leben auf der Erde und wird deshalb auch als Matrix des Lebens bezeichnet. Die Hydrationsumgebung spielt in der molekularen Zellbiologie eine wichtige funktionelle Rolle für Strukturen und Dynamiken. Ein Beispiel sind die von ihrer lokalen Hydrationsumgebung abhängigen photophysikalischen und -chemischen Eigenschaften von im UV-Bereich absorbierenden Chromophoren in biologischen Systemen. In Systemen in wässriger Lösung ermöglicht das Netzwerk aus Wasserstoffbrückenbindungen zwischen den Chromophoren und den Wassermolekülen der Umgebung nach Ionisation oder Anregung der Chromophore zusätzliche Relaxations-Pfade. Diese zusätzlichen Relaxations-Pfade sind einerseits wesentlich für die photochemische Stabilität der Chromophore. Andererseits verstärken Phänomene wie die Radiolyse des Wassers strahlungsinduzierte Schäden an biologischen Systemen, wenn sie sich in einer Hydrationsumgebung befinden. Die zugrundeliegenden Dynamiken sind trotz aufwändiger Forschung bisher schwer fassbar. Im Rahmen dieser Arbeit wird dieser Fragestellung nachgegangen. In experimentellen Studien wird systematisch untersucht welche Rolle ein einziges Wassermolekül in der Photophysik eines Modell-Chromophors, hier Pyrrole, spielt. Hierbei lassen sich die durchgeführten Experimente in zwei Hauptteile untergliedern. Während im ersten Teil eine reine Probe aus gasförmigem von Pyrrole und pyrrole(H_2O) generiert wurde, wurden im zweiten Teil mit zeit- und positions-sensitiven Detektoren photophysikalische Studien an den gewählten Modellsystemen durchgeführt.

Eine reine und rotationskalte Probe aus gasförmigem Pyrrole und pyrrole(H_2O) wurde durch die Kombination eines kalten Molekülstrahls und eines elektrostatischen Deflektors erreicht. Um verschiedene molekulare Spezies räumlich besser trennen und um den Einfluss des atomaren Trägergases in dem Interaktionsgebiet reduzieren zu können, wurde ein sog. "knife-edge" implementiert. Auf diese Weise wurde ein Molekülstrahl aus pyrrole(H_2O) mit 100%iger Reinheit erzeugt. Zusätzlich konnten die Dichte signifikant erhöht und die Rotationstemperatur des Moleküstrahls deutlich reduziert werden. Die ermittelte Rotationstemperatur nach supersonischer Expansion wurde mit $T_{\text{rot}} = 0.8 \pm\ 0.2$ K bestimmt.

Um photophysikalische Prozesse in Pyrrole und pyrrole(H_2O) zu untersuchen, wurden strahlungsinduzierte Schäden an diesen Modellsystemen durch Ionisation mit intensiven Laserpulsen (äußere Valenzschale) und mit Röntgenstrahlung (Innerschalen) imitiert. Bei der Starkfeld-Ionisation wurde bei der Einfach- und Doppel-Ionisation von Pyrrole die Fragmentierung der aromatischen Ringstruktur durch das Brechen der kovalenten C-C oder N-C-Bindungen festgestellt. Bei pyrrole(H_2O) wurden im Cluster sowohl ein schützender Effekt als auch eine leicht verstärkte Starkfeld-Ionisation und dadurch hoch geladene ionische Spezies beobachtet. In den Studien zur lokalisierten Kern-Schalen Ionisation mittels Röntgenstrahlung wurden bei der Fragmentierung reinen Pyrroles im Vergleich zur Starkfeld-Ionisation ähnliche Kanäle detektiert. Im Fall von pyrrole(H_2O) führte die zusätzliche Wasserstoffbrückenbindung mit den umgebenden Wassermolekülen zu einem Ladungs- und

Massentransfer. Auf Basis der durchgeführten Studien lässt sich zusammenfassend sagen, dass ein einzelnes über eine Wasserstoffbrückenbindung gebundenes Wassermolekül nach der Ionisation von Biomolekülen (der äußeren Valenzschale oder innerer Schalen) Pfade begünstigt, welche den Strahlenschutz erhöhen.

Contents

1 Introduction

> *"Water is life's matter and matrix, mother and medium. There is no life without water" [1]*
>
> — Albert Szent-Györgyi

1.1 Motivation

The presence of water is the crucial ingredient for the existence of carbon-based life on our planet earth. The water environment on earth provides a favorable platform for the creation of an initial form of life [1–3]. Prebiotic molecules are claimed to be formed under a physiochemical environment by the interaction of water with carbon and minerals present in the rock surface. Water being a universal solvent, has the essential properties to dissolve ions and provides a flexible environment for the primary chemical reactions, like the formation of amino acids and peptides [4–6]. On the other hand, the hydrophobic interactions between non-polar side chains of peptides with water molecules provide the primary thermodynamic driving force for the initial stages of molecular assembly [3, 5]. Therefore, the water acted as a matrix for the creation, and evolution of life on earth [1, 3].

Water is an integral part of biological matter, i. e., almost 70-80 % of the cell is comprised of water. Water also plays diverse functional, structural, and dynamic roles in molecular cell biology [7, 8]. The hydration environment, for instance, has a significant role in the assembly and the dynamics of proteins by the interaction with water molecules through a network of hydrogen bonds [9, 10]. The key factors that determine the active structure of the protein are the solute-solvent interactions (e. g., van der Waals, electrostatic, hydrogen-bond) and the active solvation facilitated by the surrounding water molecules [1, 3, 7, 9]. The hydrogen bonds are actively created and broken within the dynamical water environment around proteins [3, 9, 10]. However, the timescales and mechanisms behind the complex solvation dynamics is not fully understood so far [3, 9–11].

The function of a protein strongly depends on its structure, and this one of the major reasons behind the quest for determining the structure-function relationship, for instance, in the field of spectroscopy [12–15], diffractive-imaging of molecules [16–20], or pharmacological medicine [21, 22]. Solvation effects are known to have a strong influence on the structure and function of complex biological systems [7, 23, 24]. The photophysical and photochemical properties of strong ultraviolet (UV) absorbing chromophores found in proteins are fairly sensitive to their local hydration environment [25, 26]. For example, the photophysics of the chromophore of the green fluorescent protein (GFP) is strongly determined by its hydration environment [27, 28], and the proposed mechanism for its fluorescence is an excited-state proton transfer process [29]. Hydrogen-bonded water molecules facilitate additional relaxation pathways after photoexcitation of chromophores, which are essential for the photostability of biological matter.

Recently, the influence of the hydration environment upon the interaction of high-energy

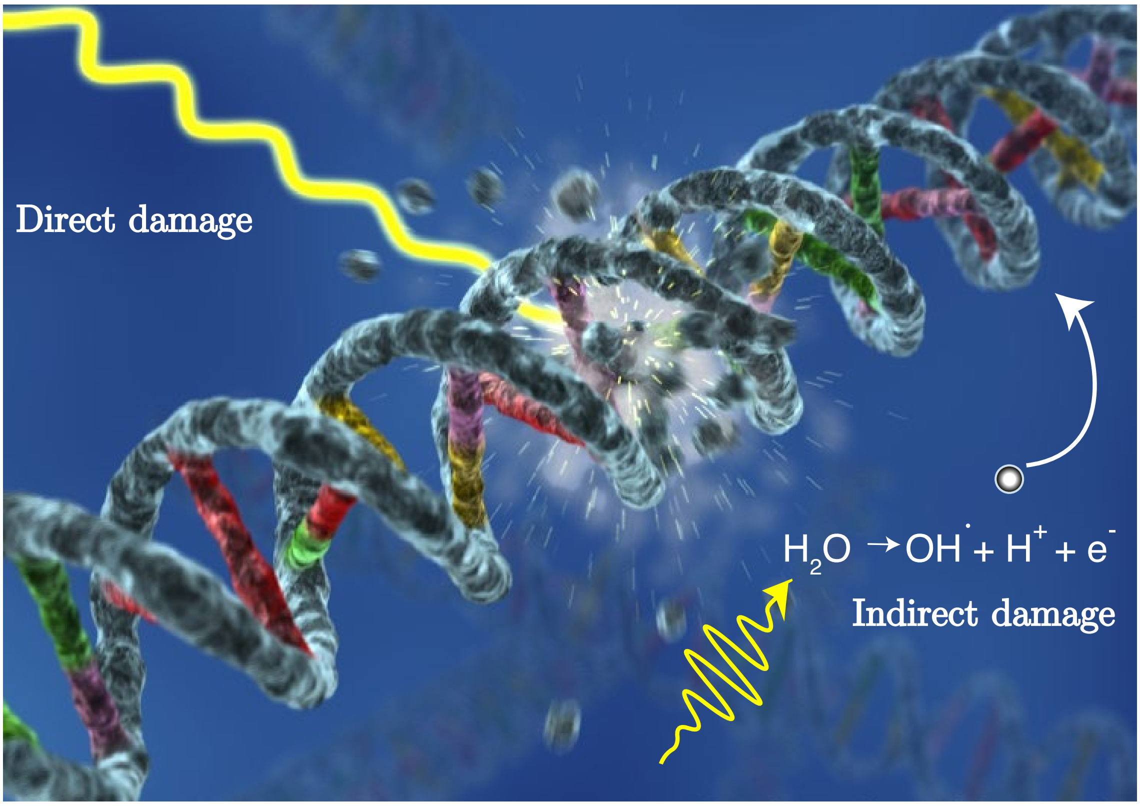

Figure 1.1. A schematic representation of radiation-induced damage of a DNA strand through the direct ionization pathway, as well as the indirect pathway due to reactive species, such as electrons and radicals, is shown. The radiolysis of water medium, surrounding the biological matter, is one of the major reasons for the creation of these reactive species. The figure is adopted from reference [30].

ionizing radiation (e. g., UV-rays, x-rays, γ-rays, charged particles) with living cells have caught significant attention [31–33]. Such studies can provide remarkable implications to understand the mechanisms underlying radiation therapy, as well as an insight into the development of methodologies to improve the biological effectiveness of radiation therapy [31, 32]. Deoxyribonucleic acid (DNA) lesions such as cross-links, base releases, and single- and double-strand breaks are the major radiation-induced damage effects in biological matter [32, 34, 35]. These dangerous damages are difficult to self-repair and can trigger harmful genome mutations, or even cell death [31, 32]. An artist's rendering of the radiation-induced damage of a DNA strand is shown in Figure 1.1. The mechanism for radiation-induced biological damage is broadly classified into two pathways. The first one is due to damage through direct interaction with ionizing radiation. The second one, so-called indirect damage, is due to interaction with various reactive secondary species originating from the ionization of the biological medium. The radiolysis of water is an unavoidable phenomenon that occurs during the interaction of ionizing radiation with biological matter, which is present in an aqueous environment. Reactive species, such as ions, radicals, and aqueous electrons, orginate from the radiolysis of water [31, 36–38]. These species can cause further bio-molecular damage, either through excitation or ionization [32, 34, 35]. The low-energy secondary electrons are known as efficient candidates to induce DNA strand breaks [32, 34, 39]. The role of solvation effects on the fragmentation of biomolecules after ionization, or excitation, has been studied in bulk [40–45] and in a microhydration environment [46, 47]. As a general observation, there exist numerous studies claiming the solvation environment can provide additional relaxation pathways to prevent radiation-induced damage of biomolecules [42, 46, 48], while the other set of experiments claims that it can trigger further fragmentation of biomolecules [40, 41, 43–45, 49]. Despite huge efforts, it is still under discussion whether the hydration effects inhibit or enhance radiation-induced biological damage. Therefore, a systematic investigation of the role of a solvent on the photophysics of a biologically relevant molecule is required. Furthermore, an investigation of the photophysics of the biomolecule solvated by many water molecules is a complex endeavor and a retrieval of an in-depth knowledge of the underlying molecular relaxation mechanisms is limited.

To overcome this limitation, in this thesis, a bottom-up approach is adopted to understand how the photophysics of an isolated molecule is influenced by the vicinity of a single water molecule. The performed studies in the gas phase have the potential to bridge the gap between isolated molecules and solvated molecules. The significance of the hydrogen bonding network on the photophysical properties of biomolecules can be explored in detail as well. Here, a prototypical biologically relevant chromophore hydrogen-bonded to a single water molecule is taken as a model system to mimic the photophysics of a protein in an aqueous environment. The model system is a singly hydrogen-bonded pyrrole(H_2O) cluster, and it represents the strongest interaction between the biomolecule, pyrrole, and surrounding water molecules in aqueous solution. The pyrrole(H_2O) cluster has a well-defined structure with the water molecule hydrogen-bonded to the N-H site of the pyrrole [50]. The heterocyclic aromatic molecule, pyrrole, is a strong UV-absorbing chromophore found, e. g., in hemes and chlorophylls [51, 52]. It is also a subunit of indole, the chromophore of tryptophan, a principal UV-absorber found in proteins [25, 52, 53]. The photophysics of these chromophores is sensitive to their local hydration environment [26], or even in the presence of a single water molecule [25, 26, 54–56]. In addition, photoexcitation of these chromophores also triggers an ultrafast internal-conversion process to the ground state, essential for the photo-stability of proteins in their natural environment [52–54].

An ultimate goal for the photophysics investigation of the model system is imaging its relaxation pathways in real-time, i. e., by simultaneous recording of the electron and nuclear dynamics to obtain so-called quantum molecular movies. The potential to record dynamics of the molecule with high spatial (picometer) and temporal resolution (femtosecond) can provide a completely new and deeper insight into how the chemical reaction occurs in real-time [18, 19, 57–60]. In the field of photophysics or photochemistry, an understanding of phenomena like bond breaking, bond formation, folding- and isomerization dynamics, as well as charge transfer, or dissociation dynamics is of significant importance [61, 62]. The invention of ultrafast lasers and ultrafast diffraction imaging techniques using x-rays or electron beams [16–20, 62–65] provides a potential route to study dynamical structural changes far from the equilibrium structure of the molecule. A crucial ingredient required to achieve the aforementioned goal is a pure sample of the model cluster. Additionally, it is important to systematically investigate the photophysics of isolated and microsolvated biomolecules to find suitable observables for future dynamical photophysics studies.

The experiments presented in this thesis are classified into three sections, namely, the preparation of cold and pure samples of microsolvated clusters in section 1.2, the investigation of microsolvated clusters after strong-field ionization in section 1.3, and the site-specific soft x-ray ionization in section 1.4. In doing so, we aim to elucidate and compare the radiation-induced damage incurred in the bare pyrrole monomer and the pure microsolvated pyrrole(H_2O) dimer, after valence-ionization as well as core-shell ionization of the pyrrole moiety. Such a systematic study is a crucial step toward the dynamic photophysics studies foreseen in the future.

1.2 Preparation and manipulation of a cold molecular beam of clusters

One of the strong requirements to perform the aforementioned studies is to prepare isolated and controlled samples in the gas phase. Molecules prepared in molecular beams provide a unique advantage to study their intrinsic properties under collision-free conditions as well as in an isolated environment.

In 1943, Otto Stern was awarded the Nobel Prize in Physics for his contributions to the field of molecular beams and discovery of the magnetic moment of the proton [66]. A cold molecular beam is generated by the expansion of molecules seeded in rare gas from a reservoir at higher pressure into a vacuum [67–74]. During the expansion process, a large part of the internal energy of a molecule is transferred to its translational degree of freedom and thereby, cooling the rotational, vibrational, and electronic degrees of freedom [67, 68, 73, 74]. In an expanded molecular beam, molecules are in their electronic and vibrational ground states with the rotational temperature of a few Kelvin [67, 73, 75–78]. The invention of pulsed nozzles, such as the Even-Lavie valve, enabled us to use a higher stagnation pressure for seed gas before the expansion into a vacuum as compared to continuous flow nozzles [71, 79]. Pulsed molecular beam methods helped to achieve rotational temperatures less than a Kelvin and also higher peak densities for molecules [72, 73, 79]. These internally cold molecules provided opportunities to perform high-resolution spectroscopy, determine the structure of molecules and molecular complexes, study collisions, and investigate quantum effects in a wide range of ultra-cold molecular systems [80–84].

The molecular beam method opens up possibilities to study weakly bound clusters, such as the van der Waals clusters and the hydrogen-bonded clusters [67, 68, 75]. Clusters are efficiently formed during the early phase of beam expansion, through a low-energy collision between clustering molecules and rare-gas atoms present in the molecular beam [67, 68, 70, 73, 75]. The cluster size and its distribution are determined by the vapor pressure of the sample present in the reservoir before the supersonic expansion, as well as the expansion conditions [70, 73, 75, 85]. Hence, the clustering, which is a complex process, can be controlled to some extent. However, the molecular beam expansion always comprises of an ensemble of species, including the seed gas, monomers of molecules, and molecular clusters of different sizes [73, 76, 77]. A prerequisite condition for experiments performed in this thesis is the preparation of a pure molecular beam of the monomer and size-selected molecular cluster. The size-selection and the spatial separation of individual species are feasible in a cold molecular beam, for instance, by using additional beam manipulation techniques, such as electrostatic deflection [86].

The manipulation of the molecular beam with external electric and magnetic fields can be used to achieve quantum-state selectivity and spatial control [86–91]. Manipulation of the trajectory of species in a molecular beam is familiar to us through the famous Stern-Gerlach experiment demonstrating the deflection of silver atoms in inhomogeneous magnetic fields [90]. Another famous example in this context is the use of an electrostatic quadrupole focuser during the discovery of microwave amplification by stimulated emission of radiation (MASER) [92], to focus only ammonia molecules with a population inversion into a microwave cavity. Over the past years, many experiments demonstrated that neutral molecules could be deflected, focused, accelerated, decelerated [84, 86, 89, 93, 94], or even trapped in space using external electric fields [93, 95]. Other methods to deflect molecules are possible by using microwave- [96] and optical fields [97–99]. It is only possible to manipulate the transverse and longitudinal motion of molecules using the aforementioned methods. However, molecules can rotate freely in the gas phase, even in a cold molecular beam, i. e., they have isotropic orientations. To fix the molecules in space, the alignment and orientation of molecules are required, which is feasible using a cold molecular beam [91, 99–104].

The electrostatic deflection is an efficient method for the manipulation of large polar molecules and to achieve sub-Kelvin rotational temperatures [86]. Quantum-state and conformer selection as well as spatial separation of clusters can be achieved using an electrostatic deflection [76, 86, 105–110]. The electrostatic deflector, an electrostatic analogue to the inhomogeneous magnetic field used in the Stern-Gerlach experiment, is employed throughout this thesis for the spatial separation of the seed gas, monomers, and clusters present in the expanded molecular beam. Clusters of different sizes have different dipole moments, and they can be separated in space using an inhomogenous electric field inside the deflector based on their effective-dipole-moment-to-mass ratios [76, 86]. In general, cluster selection ensures that the cluster of the desired size is dominant or at least enhanced in the deflected part of the molecular beam. It is necessary to implement additional skimming techniques to achieve better contrast or desired level of purity of ∼100 % for the selected cluster. It is feasible to shape the molecular beam using skimmers, knife edges, razor blades, slits, slit-skimmers, or gratings to select a specific part of the beam [67, 111–114]. The knife-edge skimming technique can be implemented to provide better contrast and column density for the selected cluster. Furthermore, it has an advantage to significantly reduce the amount of signal originating from the seed gas. The pyrrole(H_2O) cluster beam with a purity of ∼100 % is achieved in this thesis, using the combination of an electrostatic deflector and the knife-edge.

Preparing cold and pure molecular beams of size-selected clusters can be advantageous for advanced experiments aimed at imaging the structure and the dynamics of the microsolvated cluster in the molecular frame. Furthermore, the cold molecular beam of clusters provides the possibility to control the orientation of the cluster in the laboratory frame by laser alignment or mixed-field orientation [104, 115, 116].

1.3 Photophysics of microsolvated clusters after strong-field ionization

Radiation-induced damage to biological matter is a ubiquitous phenomenon in nature. Ionization and excitation are similar from the perspective of radiation damage; both can lead to molecular fragmentation. Photophysics investigations are substantial to elucidate many relaxation mechanisms observed in our nature, after photoexcitation or ionization.

Biological matter undergoes radiation-induced damage upon interaction with ionizing radiation or high-energy charged particles [31, 32], as discussed earlier in the Motivation section. The secondary effect of ionizing radiation is one of the key reasons for radiation damage occurring in biological systems [32, 34, 35]. These secondary effects are known to cause outer-valence ionization in molecules [31, 32]. Various attempts were made either on isolated molecules or solvated molecules to mimic the radiation damage through outer-valence ionization. This was performed either by a direct deep UV-radiation or by using low-energy electrons [40–46]. In this context, the role of the water environment on the radiation damage of biomolecule, whether it has a protective or catalytic effect, remains elusive. A systematic study through the comparison of fragmentation processes after valence ionization of an isolated biomolecule and the biomolecule in the presence of a single water molecule can help to answer existing uncertainties. In the framework of this thesis, a strong-field ionization strategy is adapted to perform outer-valence ionization. In order, to mimic the radiation damage on biological systems, fragmentation studies are performed on the model systems, pyrrole and pyrrole(H_2O), after single and double outer-valence ionization. Overall, water acted as radiation protection agent for the biomolecule after valence ionization. These studies have implications on the relevance of hydrogen-bonded water molecules in the photophysics of biological systems.

In the strong-field ionization regime, there exists the phenomenon of multiple electron ejection and Coulomb explosion from highly-charged cationic states as a consequence resulted due to the interaction of atoms, molecules, and clusters with very high intense fields [117, 118]. The phenomenon of enhanced valence ionization was investigated both theoretically and experimentally for diatomics, triatomic, and small hydrocarbons in the strong-field regime, and the attributed reason is the charge resonance enhanced ionization (CREI) occurring around critical internuclear distances [119–123]. Interestingly, an enhanced inner-shell ionization and the creation of highly-charged atomic ions were observed for large (with tens to hundreds of units) van der Waals or hydrogen-bonded clusters in the strong-field regime [117, 118, 124–130]. In this case, the proposed mechanisms are either the coherent electron motion model (CEMM) or the ionization ignition model (IIM) [119, 128]. However, the responsible mechanism for inner-shell ionization is still an open question [117, 118, 130, 131]. The charge-localization effects in the strong-field regime can cause multiple ionization of the system and can enhance radiation-induced damage of biomolecules, though it is a weak phenomenon. The photophysics of pyrrole and pyrrole(H_2O) are investigated in this thesis, from the perspective of enhanced ionization, to unravel their effects on radiation-induced damage of biological systems. Furthermore, such studies provide a simple model system to investigate the relevant mechanisms for inner-shell ionization in the strong-field regime.

Within the context of this thesis, Coulomb explosion Imaging (CEI) is used as an experimental technique to image the 3D momenta of all ionic fragments originating from strong-field ionization of molecules/clusters. The term Coulomb explosion is used for the process of fragmentation owing to Coulomb force driven charge repulsion after multiple ionization of a molecule. Coulomb explosion imaging technique was initially developed to determine the structure of the molecule through the Coulomb explosion of multiply charged cation formed by colliding a fast molecular beam of ions on to a thin foil of metal [132, 133]. Coulomb explosion can be induced by intense radiation sources, for example, ionization by intense femtosecond laser pulses or x-ray ionization. Earlier, Coulomb explosion after strong-field ionization was demonstrated as an experimental probe to measure the dynamics of wave packets of I_2 [134, 135]. Nowadays, Coulomb explosion imaging is a widely used experimental technique to study the structure and fragmentation dynamics of molecules, provided the dissociation occurs rapidly after ionization, and an axial recoil-frame approximation holds for the fragmentation process [132, 134].

1.4 Photophysics of microsolvated clusters after x-ray ionization

In 1895, Wilhelm Conrad Röntgen discovered x-rays as a new type of electromagnetic radiation [136]. x-rays cover the electromagnetic spectrum in the wavelength region of a few nm to a few pm [137–139]. The small wavelength of x-rays makes them suitable to image the structure of matter through diffraction with atomic resolution [18, 138]. For example, they were used to determine the double-helix structure of the DNA [140]. In addition, x-rays can be used for localized ionization in a molecule due to their element-specific absorption cross-sections [137, 138]. The element specificity of x-rays can be efficiently employed to induce and study site-specific dynamics in a molecule or cluster [141–

143]. Ionization using x-rays provide a direct handle to trigger and control localized chemical dynamics, unlike the scenario of strong-field ionization, where controlling the dynamics is not straightforward. Soft x-rays were extensively used over the last decade, to study ultrafast relaxation processes in molecules or clusters after core-shell ionization. Specifically, relaxation processes like Auger decay [144, 145], Interatomic (molecular) Coulomb decay [143, 146–149], or charge rearrangement processes like electron- and proton-transfer mediated charge separation [142, 150–152] are investigated in molecules or clusters. One of the challenges to unravel the complex relaxation pathways is the simultaneous detection of all fragmentation products originated after ionization.

Advanced coincidence imaging techniques through simultaneous detection of ions and electrons, were developed for extensive investigation of the fragmentation dynamics of molecules. Few of these major techniques only emerged over last the decades, namely, Photoion-Photoion Coincidence (PIPICO) [141, 153–155], Photoelectron-Photoion-Photoion Coincidences (PEPIPICO) [156–159], or Auger-Electron-Photoion-Photoion Coincidences (AEPIPICO) [158]. Additional attempts were performed to get structural information off molecules together with their dynamics after ionization, for example, by measuring the Recoil-Frame Photo Angular Distributions (RFPAD) [160–162] and Molecular-Frame Photo Angular Distributions (MFPAD) [103, 163, 164].

In the context of this work, soft x-rays are used for site-specific core-shell ionization of both pyrrole and pyrrole(H_2O) cluster. The intention is to study the influence of the water molecule on the radiation damage of core-shell ionized pyrrole, a prototypical biomolecule. Both pyrrole and pyrrole(H_2O) are ionized at the nitrogen atom, the site at which the water molecule is hydrogen-bonded to the pyrrole moiety. The photophysics investigation on this model cluster envisages probing the inter-molecular relaxation mechanisms occurring across the hydrogen bond and thereby the role of hydrogen bonding networks in biology.

1.5 Outline of this thesis

The main objective of this thesis is to perform a systematic investigation of the influence of the local solvent environment on the photophysics of a biologically relevant prototypical molecule. The microsolvated pyrrole(H_2O) is the model system for the photophysics studies aiming at bridging the gap between the isolated, and hydrated biomolecules in general. To realize that, two main goals are accomplished in this thesis. First, a pure molecular beam of size-selected pyrrole(H_2O) cluster is prepared. Second, the pure beam is utilized to study how the fragmentation dynamics after outer-valence and inner-shell photoionization changes in comparison to bare pyrrole.

An overview of the structure of the thesis is described here. The fundamental concepts required to follow this thesis are provided in chapter 2. The chapter starts with a brief description of molecular beams, cluster formation, and fundamentals of dc-Stark effect methodology utilized for the cluster selection. The principles of strong-field and inner-shell ionization mechanisms are described. Also, an overview of 3D momenta imaging techniques, together with various ion imaging analysis, is mentioned.

In chapter 3, the implemented experimental methodology to improve the spatial separation of the species in a molecular beam by the electrostatic deflector is described. A combination of a knife-edge and an electrostatic deflector is utilized to enhance the contrast for separation of different molecular species from each other, as well as from atomic seed gas, in a molecular beam. Also, an increase in the column density of the selected molecular-beam part in the interaction zone is discussed.

In chapter 4, the generation of the cold and pure beam of pyrrole(H_2O) cluster is shown. The spatial separation of pyrrole and pyrrole(H_2O) clusters from the other atomic and molecular species in a supersonically-expanded beam is demonstrated. The separated pyrrole(H_2O) cluster beam has a purity of $\sim$100 %, a remarkable achievement for cluster selection to date. Monte-Carlo simulations are performed to quantitatively support the experimental results, and to extract the rotational temperature of pyrrole and pyrrole(H_2O).

In chapter 5, the fragmentation studies after strong-field ionization of pyrrole and its microsolvated pyrrole(H_2O) cluster are performed. To mimic the radiation damage through outer-valence ionization, both species are ionized by intense 800 nm femtosecond laser pulses. Overall, the hydrogen-bonded single water molecule strongly reduces the fragmentation probability after single and double ionization, and thus water acted as the radiation protection agent for ionized pyrrole.

In chapter 6, the phenomenon of enhanced ionization in the strong-field regime is studied. A comparative study of pyrrole and pyrrole(H_2O) has been performed. An enhanced ionization leading to the formation of highly charged carbon species is only observed for the case of pyrrole(H_2O). The formation of core-shell ionized carbon atoms, through strong-field ionization of pyrrole(H_2O) using laser pulses with a peak intensity of $\sim 1 \times 10^{14}$ W/cm^2, is discussed. Moreover, these experiments open up the necessities for an extensive theoretical framework that can explain enhanced inner-shell ionization phenomena observed in molecular complexes.

In chapter 7, an experiment to investigate the photophysics after soft x-ray ionization of pyrrole and pyrrole(H_2O) is described. The goal is to study the role of the single water molecule in the radiation damage processes in biological systems after core-shell ionization. In order to mimic the direct radiation damage effects biomolecule, a site-specific inner-shell ionization was performed at the nitrogen atom present in the pyrrole moiety of the cluster. The fragmentation products were measured in a coincidence using a double-sided velocity map imaging spectrometer for simultaneous detection of electrons and ions.

Finally, in chapter 8, a summary of the research work performed in this thesis is given. Also, my contributions towards alternative approaches for studying solvation effects are briefly described. An outlook of ongoing and prospected projects to continue the work presented in this thesis is also given.

2 Fundamental Concepts

This chapter gives an overview of the fundamental concepts necessary to understand the experimental, theoretical, and numerical methods used in this thesis. Additional details on the concepts discussed in this chapter are available on standard textbooks [67, 68, 70, 112, 137, 138, 165–168].

2.1 Cluster formation in molecular beams

Molecular-beam methods are extensively used in gas phase studies (e. g., physical chemistry and molecular physics) to prepare an ensemble of isolated molecules or molecular complexes. They provide unique advantages to gain fundamental insight into mechanisms and dynamics of elementary molecular and chemical processes [67, 68, 112, 165]. In this thesis, a supersonic beam is used for the generation of a neutral bimolecular hydrogen-bonded cluster of a biomolecule with water.

A brief description of the supersonic molecular beam expansion is given, before going into details of the physics of cluster formation. The supersonic expansion enables the preparation of internally cold and isolated gas-phase molecules. A supersonic beam is formed by a high-pressure expansion of molecules seeded in a carrier noble gas through an orifice into a vacuum [71–74]. During the expansion through an orifice, at a short distance from the exit, molecules undergo collisions with the carrier gas and transfer their internal energies into kinetic energy resulting in a fast highly directional molecular beam [71, 74]. The expanded molecular beam has a very narrow angular and velocity distribution. The translational velocity depends on the stagnation pressure and carrier gas properties. The width of the velocity distribution determines the translational temperature, which is generally a few Kelvin [74, 84]. Further inelastic collisions with the carrier gas during the expansion help to significantly cool the internal degrees of freedom, i. e., the rotational (efficient cooling) and vibrational (relatively good cooling) degrees of freedom [73, 75]. Typically, the rotational temperature of the molecules is a few Kelvin, while the vibrational temperature is of a few tens of Kelvin [77, 78]. In a cold molecular beam expansion, low-energy collisions that enable efficient cluster formation are favorable [73]. This is utilized for the formation of hydrogen-bonded clusters.

Next, the physics of cluster formation is discussed. The binding energy of hydrogen-bonded molecular clusters (dimers) is typically around a few hundred meV [75, 169]. Hence, for the molecular cluster formation, low-energy three-body collisions are required, where a collision with a third body carries away kinetic energy and thereby stabilizes the formed cluster [67, 68]. In a conventional gaseous reservoir at equilibrium conditions, the number of hydrogen-bonded complexes formed is relatively low, as the high energy of the molecules does not favor low energy collisions necessary for cluster formation. In principle, the probability for the cluster formation can be increased by reducing the temperature until the process is limited by the condensation point. However, the vapor pressure of the sample also drops drastically with decreasing temperature, and this results in a reduced number density of the clusters. Only a small amount of molecular complexes is created in a gas cell reservoir under equilibrium conditions, even in the most favorable conditions [75, 170]. The concentration of the formed clusters can be increased by moving into a regime of non-equilibrium conditions, i. e., by using molecular beam methods (e. g., in a supersonic expansion of a molecular beam) [68, 74]. The low-energy collisions are feasible during the expansion process, enabling the cluster formation. Although formed clusters are stabilized and cooled *via* collisions with the carrier gas, typically achieved rotational temperatures are much smaller than 10 K [76, 77]. An elevated rotational temperature for the cluster beam is due to the energy dissipated during the cluster formation [70], and hence, achieving a sub-Kelvin rotational temperature for a cluster beam is a difficult task.

Additionally, the extent of the cluster formation can be controlled by choice of the nozzle size, carrier gas, and stagnation conditions, i. e., the temperature and pressure [70, 75, 85, 171]. The cluster size distribution is broadly classified into two regimes: small cluster and large cluster regime. In a smaller cluster regime, the distribution follows roughly an exponential decay $\mathbf{e}^{-N}$, where N is the number of monomer units that formed the cluster [70, 172]. For a large cluster regime, the clustering trend follows a log-normal distribution [70, 173]. The cluster expansion is optimized for a small cluster regime for experiments performed in this thesis. However, a molecular beam expansion always results in an ensemble of monomers and clusters of different sizes [76, 86].

In brief, the molecular clusters formed in a supersonic expansion are internally cold. In a higher pressure expansion, i. e., using stagnation pressure of around 80-100 bar, typically achieved rotational temperature for clusters is a few K [76, 108, 110]. This ensures that only a few rotational states are populated, which makes it easier for spectroscopic analysis for example. In this thesis, the generated rotationally cold molecular beam enabled us to perform the spatial separation of size-selected clusters using the dc-Stark effect.

2.2 Species selection and separation using the Stark effect

The spatial separation of size-selected molecular clusters can be achieved by utilizing the different permanent dipole moment of each molecular species, which can interact with external fields, such as the electric field [76, 86, 108, 174]. In this thesis, an electrostatic deflector [86] is employed to manipulate the trajectories of the different molecules in a molecular beam based on the phenomenon of the dc-Stark effect [86, 175]. The following section is classified into two subsections. The subsection 2.2.1 describes the rotational eigenstates of the molecule in the absence of an electric field and how it gets modified in the presence of a static electric field. The method of species selection using an electrostatic deflector is described in the subsection 2.2.2.

2.2.1 Molecules in electric fields

In quantum mechanics, the total energy W of a molecule can be obtained by solving the Schrödinger equation [176]

$$W\,\Psi = \hat{H}\,\Psi, \tag{2.1}$$

where $\hat{H}$ is the total molecular Hamiltonian in the center-of-mass frame of the molecule, and Ψ is the molecular wave function. Following the Born-Oppenheimer approximation [177] and Eckart condition [178], the total molecular Hamiltonian $\hat{H}$ can be written as a combination of rotational ($\hat{H}_{\text{rot}}$), vibrational ($\hat{H}_{\text{vib}}$), electronic ($\hat{H}_{\text{el}}$), and nuclear spin ($\hat{H}_{\text{ns}}$) contributions.

$$\hat{H} = \hat{H}_{\text{rot}} + \hat{H}_{\text{vib}} + \hat{H}_{\text{el}} + \hat{H}_{\text{ns}} \tag{2.2}$$

The molecules in a supersonic expansion are internally cold as mentioned in Section 2.1, which ensures that they are typically in their electronic and vibrational ground state. Hence, the electronic and vibrational terms are not elaborated. Furthermore, the nuclear spin term is neglected for simplicity. The remaining term is the field-free rotational Hamiltonian of the molecule [167], and it is represented as

$$\hat{H}_{\text{rot}} = \hat{H}_{\text{rigid rot}} + \hat{H}_{\text{d}}, \tag{2.3}$$

where $\hat{H}_{\text{rigid rot}}$ is the Hamiltonian of the rigid-rotor molecule, and the Hamiltonian $\hat{H}_{\text{d}}$ compensates for the centrifugal distortions in the structure of the molecule [167]. The first and most important term of the total rotational Hamiltonian, the rigid-rotor part, is given by

$$\hat{H}_{\text{rigid rot}} = \frac{\hat{J}_x^2}{2I_x} + \frac{\hat{J}_y^2}{2I_y} + \frac{\hat{J}_x^2}{2I_z}, \tag{2.4}$$

where $\hat{J}_i$ represents the total angular momentum operator on the i^{th} axis of the molecule, and I_i corresponds to the moment of inertia around the molecular-fixed axis with $i = x, y, z$. The rotational constant of the molecule is defined as $B_i = \hbar^2/2I_i$.

Next, the interaction of a rigid rotor molecule with an external static electric field is described. The modification in the rotational Hamiltonian can be written as

$$\hat{H}_{\text{rigid rot, }\epsilon} = \hat{H}_{\text{rigid rot}} + \hat{H}_{\text{Stark}}, \tag{2.5}$$

where $\hat{H}_{\text{Stark}}$ represents the interaction between the molecule and static electric field, also known as the dc-Stark effect [175]. The interaction of a polar molecule with a static electric field leads to energy shifts and hybridization of the wave function. The Hamiltonian for Stark effect is given by

$$\hat{H}_{\text{Stark}} = -\overrightarrow{\mu}\,.\,\overrightarrow{\epsilon} = -\epsilon \sum_{i=x,y,z} \mu_i \Phi_{iZ}, \tag{2.6}$$

where $\overrightarrow{\mu}$ is the permanent dipole moment of the molecule in the molecular-fixed frame, and

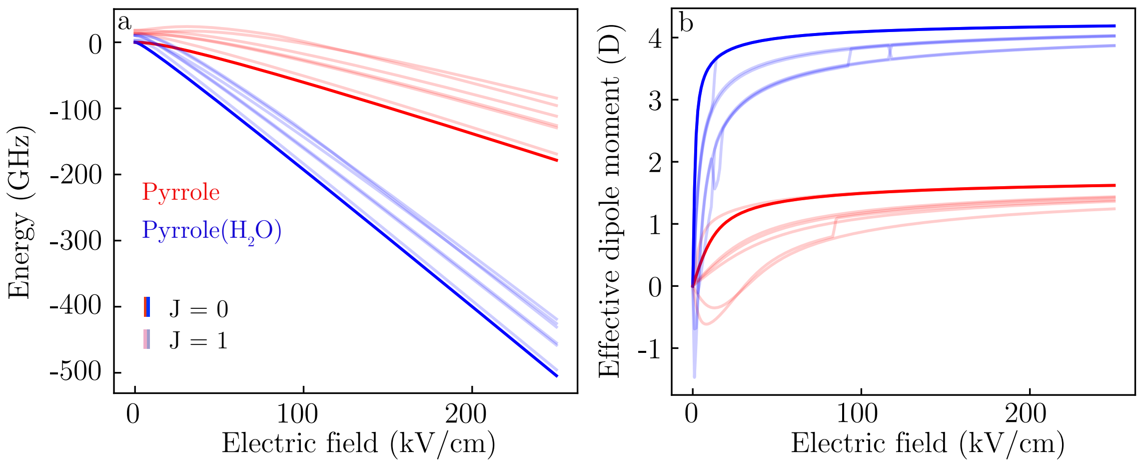

Figure 2.1. a) The plot for Stark energy of pyrrole (red) and pyrrole(H_2O) (blue) as function of electric field strength for $J = 0$ and $J = 1$ states calculated using CMIStark [179]. b) The effective dipole moment of both the species, derived from the first derivative of energy shift with respect to electric field strength.

$\overrightarrow{\epsilon}$ is the static electric field applied in the laboratory-fixed frame. The term μ_i represents the dipole moment components in the molecule-fixed axes x, y, z. The molecular-fixed frame can be related to the laboratory-fixed frame (X, Y, Z) *via* a coordinate transformation using the direction cosine matrix Φ_{iZ}, which represents the projection of molecular axes onto the direction of the applied electric field, which is the Z-axis [166]. The eigenvalues of the rotational Hamiltonian incorporating the Stark interaction are obtained by matrix diagonalization on the basis of the symmetric-top wave functions. In this thesis, the Hamiltonian and Stark energy W_{Stark} of the molecules are calculated using the CMIStark [179] program package. The Stark energy depends on the electric-field strength, enabling the manipulation of the motion of molecules using inhomogeneous electric field. The effective dipole moment μ_{eff} along the space-fixed electric field direction can be calculated as the first derivative of the energy

$$\mu_{\text{eff}}(\epsilon) = -\frac{dW_{\text{Stark}}}{d\epsilon}. \tag{2.7}$$

The energy shift due to the Stark effect as a function of the electric field strength for $J = 0$ and $J = 1$ rotational states of pyrrole (red) and pyrrole(H_2O) (blue) is shown in Figure 2.1 a. The lowest rotational state ($J = 0$) of both species shows the largest reduction in the Stark energy with increasing electric field strength. The shaded lines for the rotational quantum number $J = 1$ belong to various quantum states represented by $|JK_aK_cM\rangle$, where K_a, K_c are the pseudo quantum numbers used for asymmetric top molecules, and M refers to the projection of $\hat{J}$ onto the laboratory-fixed axis [86, 179]. As a general trend for pyrrole and pyrrole(H_2O), the energy of quantum states is lowered for an increasing field strength. The corresponding effective dipole moments for $J = 0$ and $J = 1$ rotational states of both species at these electric field strengths are shown in Figure 2.1 b. The states can be classified as weak-field seeking ($\mu_{\text{eff}} < 0$) and strong-field seeking states ($\mu_{\text{eff}} > 0$). The molecules in weak-field seeking states increase their energy with an increment in field strength, while strong-field seeking states decrease their energy with an increment in field strength. As can be seen from Figure 2.1, pyrrole(H_2O) has a larger Stark energy and effective dipole moment than pyrrole monomer. At low electric field strengths, i. e., < 50 kV/cm, both weak- and strong-field seeking states exist for pyrrole and pyrrole(H_2O). At certain field strengths, the weak-field seeking states turn into strong-field seeking states, and this is due to avoided crossings between neighboring states of similar symmetry [86, 179, 180]. At very large field strengths, the effective dipole moment converges to the permanent dipole moment of the molecule [181]. We used electric field strengths around 100 kV/cm in our experiments, for which most of the rotational states are strong-field seeking.

2.2.2 Electrostatic deflector

The strong dependence of the Stark energy and effective dipole moment of the molecule on the electric field strength provides the possibility to manipulate or control the trajectories of molecules in a molecular beam. In this thesis, an electrostatic deflector is used for this purpose. The deflector consists of two closely spaced electrodes at different static potentials to generate an inhomogenous electric field in one direction [86, 105]. The force $\overrightarrow{F}$ exerted on molecules in this inhomogenous electric field [86, 182] is given by

$$\overrightarrow{F} = -\overrightarrow{\nabla} W = \mu_{\text{eff}}.\overrightarrow{\nabla}\epsilon, \tag{2.8}$$

where $\overrightarrow{\nabla}\epsilon$ is the gradient of the applied electric field. The molecules with different effective dipole moments will experience different forces inside an electrostatic deflector and, hence, follow different trajectories. This is utilized for the spatial separation of pyrrole and pyrrole(H_2O) in our experiments [108]. The amount of deflection depends on the effective-dipole-moment-to-mass ratio for a given gradient of the electric field [86]. The absolute value of the inhomogenous electric field created between the deflector electrodes for an applied voltage of 14 kV is shown in Figure 2.2. Two different deflector geometries were used in this thesis. An a-type deflector, as shown in Figure 2.2 a, was used in chapters 5 and 6, whereas a b-type deflector (Figure 2.2 b) was used in chapters 3, 4 and 7. The dashed circles represent the diameter and the position of the molecular beam for each deflector geometry. For this in-coupling position, the molecules in high-field seeking states experience a force in the $+Y$ direction inside the a-type deflector. In the b-type deflector, however, they will experience a force in the $-Y$ direction, for the demonstrated position of the molecular beam. As a remark, the b-type deflector enables using significantly stronger electric fields as well as stronger deflection without molecules crashing into the device itself. A detailed overview of the comparison between these two geometries and the advantages of using the b-type deflector can be found elsewhere [86, 183, 184]. Also, the electrostatic deflector has been successfully used for the quantum-state selection [105], and the spatial separation of nuclear-spin isomers [185], conformers [107], or molecular clusters [76, 108, 110].

Next, a discussion about the performed simulations to calculate the trajectories of

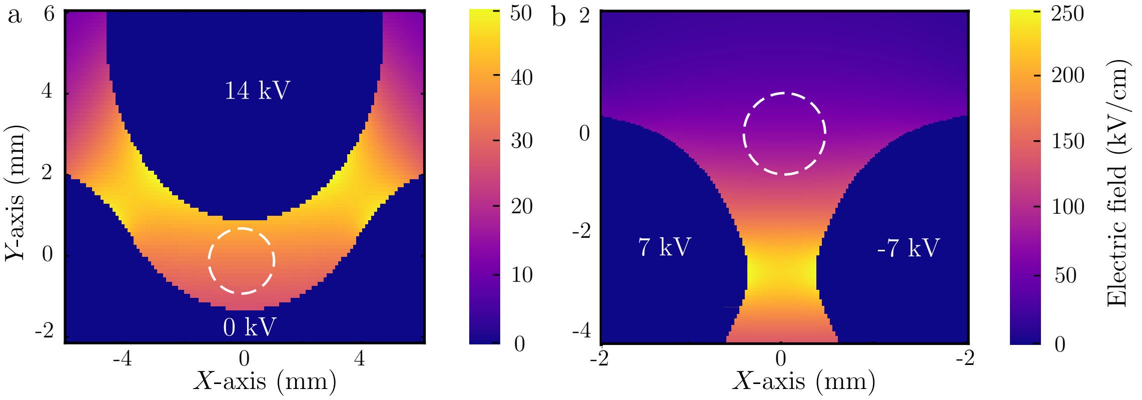

Figure 2.2. The inhomogenous electric field created inside an electrostatic deflector for an applied voltage of 14 kV. The molecular beam propagates in the Z direction. The diameter and in-coupling position of the molecular beam is marked by the dashed circle. a) The electric field inside an a-type geometry of the deflector. b) The electric field created inside a b-type deflector.

molecules inside our molecular setup containing an electrostatic deflector is given. In this thesis, Monte Carlo trajectory simulations are performed for the individual $|JK_aK_cM\rangle$ quantum states using a basis-set approach. For this, we used Stark energies and effective dipole moments calculated using CMIStark [179] as the input. We moreover used the deflector geometry, electric field and field gradient inside the deflector, which we obtained from finite element simulations [186]. Using all these pieces of information, we computed the force and acceleration experienced by molecules in each quantum state in the inhomogeneous field of the deflector. We assumed that the molecules propagate adiabatically in the field, i. e., molecules stay in a single well-defined adiabatic quantum state [86]. The field-free trajectories of molecules before and after the deflector are also calculated, in addition to the trajectory inside the deflector, to simulate the profile of the molecular beam in the interaction zone. For the simulations, the geometrical constraints of the deflector and mechanical apertures in the molecular beam setup are incorporated. As a first step, we fit the simulations to an experimental molecular beam profile for a deflector voltage of 0 kV (field-free), to determine the spatial and velocity spreads of the initial molecular beam. In this step, we also account for the imperfect alignment of the molecular beam machine. Afterwards, we perform trajectory simulations for the deflector voltage used in the experiment. We take all $|JK_aK_cM\rangle$ quantum states up to a maximum value for J into account, for which the population of the rotational state is negligible. A maximum of $J = 15$ was used for the simulations performed for pyrrole and pyrrole(H_2O) in chapter 4, with which we take into account greater than 99.95% of the total rotational state population. The probability distribution of rotational state population N of a molecule with the rotational temperature of T_{rot} is given by the Boltzmann distribution [86]

$$N(T_{\text{rot}}) \sim \exp\left(\frac{-W}{k_{\text{B}} T_{\text{rot}}}\right), \tag{2.9}$$

where W is the Stark energy, k_B is the Boltzmann constant, and T_rot is the rotational temperature. Finally, we fit the rotational temperature of the initial molecular beam by minimizing the root mean square error (RMSE) between the simulation and experiment.

2.3 Molecules in ionizing fields

Ionization of matter is one of the ubiquitous consequences of light-matter interaction. Ionization results in the removal of one or more bound electrons from an atom or molecule when the deposited energy is greater than the binding energy. The mechanism for ionization strongly depends on the electric field strength and frequency of the radiation used for the process. In this thesis, the fragmentation dynamics of the molecules after strong-field and site-specific x-ray ionization are investigated in chapters 5 and 6 and chapter 7, respectively. An overview of ionization mechanisms in both scenarios is given in the following section.

2.3.1 Strong-field ionization

The ionization mechanisms caused by laser fields can be broadly classified into perturbative and strong-field ionization. For perturbative ionization, the electric field is weak as compared to the Coulomb field binding the nuclei and electrons [187]. In the strong-field regime, however, the strength of the electric field becomes comparable to the Coulomb potential, and this can lead to distortion of the binding potential [188]. The strong-field ionization is employed in this thesis in chapters 3 to 6, and is the focus of the following section.

A schematic representation for the field-free and field-dressed binding potential is shown in Figure 2.3. If the energy of the photons used for ionization is lower than the ionization potential (I_p) of the molecule, the ionization under the strong-field regime can occur mainly by three mechanisms. The first mechanism is multi-photon ionization, as shown in Figure 2.3 a, where multiple photons are absorbed simultaneously to overcome the ionization barrier [187, 189, 190]. For the case of multi-photon ionization, electrons are ejected with finite kinetic energy into the continuum. The absorption of an excess number of photons than required to ionize the molecule leads to the process of above-threshold ionization (ATI). In such a scenario, the additional number of photons is absorbed by the electron [189, 191] and results in equally spaced ATI peaks in the kinetic energy spectra of electrons, which are separated by the energy of a single photon. If the electric field strength of the laser is increased, the molecular potential gets distorted, resulting in tunnel ionization as represented in Figure 2.3 b, where the electron can tunnel out through the field-suppressed ionization barrier [188, 192]. At very high electric field strengths, the binding potential of the molecule is heavily distorted such that the electron is completely unbound, and hence escapes into the continuum. This situation is called over-the-barrier ionization and is shown in Figure 2.3 c. The ionization mechanism in the strong-field regime

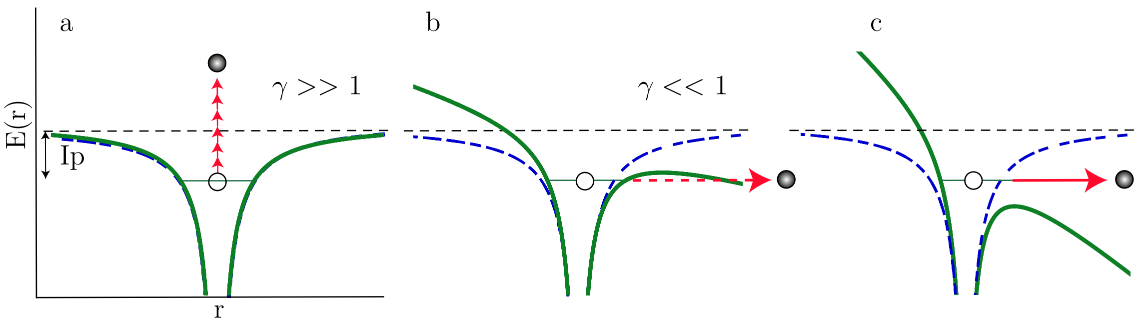

Figure 2.3. The schematic representation for different cases of strong-field single ionization. The dashed blue line shows the field-free binding potential and the green curve corresponds to the field-dressed potential. The dashed black line represents the ionization potential for the field-free case. a) Multi-photon ionization, b) Tunneling ionization, and c) Over-the-barrier ionization.

can be characterized using the Keldysh parameter γ given by [193, 194]

$$\gamma = -\frac{T_{\text{tunnel}}}{T_{\text{osc}}} = \sqrt{\frac{I_\text{p}}{2U_\text{p}}}, \tag{2.10}$$

where T_{tunnel} is the time required for an electron to tunnel through the barrier; T_{osc} is the oscillation period of the laser field of frequency ω, given by $T_{\text{osc}} = \frac{2\pi}{\omega}$; I_p is the ionization potential and U_p is the ponderomotive energy, which is the cycle-averaged quiver energy of an electron in the oscillating field. The value of γ increases for shorter wavelengths and weaker fields, where the electron essentially does not have the time to tunnel into the continuum. The multi-photon ionization dominates in the regime, where $\gamma >> 1$, and the mechanism can be described through perturbation theory [187, 190]. Conversely, the value of γ decreases for longer wavelengths or stronger fields. The ionization occurs through tunneling mechanisms for $\gamma << 1$. The theoretical models describing the tunnel ionization process and the rate of ionization for atomic-like species are given by the ADK model [195] or the KFR theory [190, 193, 196, 197]. They are commonly known as the strong-field approximation, and later this was extended to incorporate the case of molecular ionization and the effects of the molecular orbitals. A detailed overview of these attempts can be found elsewhere [188, 190, 194]. The experiments performed in this thesis are in a regime of γ~1, and hence, neither the pure tunneling nor pure multi-photon mechanisms are valid. This intermediate regime is called non-adiabatic ionization [188, 190], where the ionization mechanism is a mixture of both.

In general, strong-field ionization with an intense laser field can singly as well as multiply ionize the molecule. The molecule can undergo fragmentation in both scenarios. In the case of multiple ionization, the highly-charged parent ion undergoes fragmentation due to Coulomb repulsion, and imaging the recoil directions of these fragments can provide information about the underlying fragmentation dynamics.

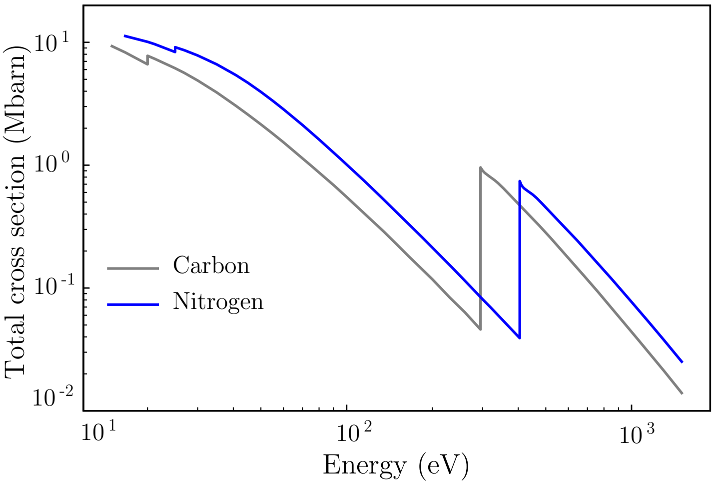

Figure 2.4. The calculated total x-ray absorption cross-sections for carbon (grey) and nitrogen (blue) as function of the photon energy. The data is taken from reference [198].

2.3.2 Site-specific soft x-ray ionization

In chapter 7, soft x-rays were used to perform site-specific core-shell ionization of molecules. Single core-shell ionization of atoms occurs after the absorption of high energy photons, whose energy is greater than the binding energy of inner-shell electrons. The total x-ray cross-section for atomic species is determined by its electronic structure and by the photon energy [137]. As a general rule for soft x-rays, the total absorption cross-section scales approximately as Z^4, where Z is the atomic number [138]. For a given atom, the absorption cross-section reduces with an increase in photon energy, except at photon energies just above the absorption edges [199]. This general trend for the absorption cross-section as function of the photon energy roughly scales as E^{-3}, where E is the energy of the photon.

The calculated total x-ray absorption cross-sections for carbon (grey) and nitrogen (blue) atoms are shown in Figure 2.4 [198]. In general, the absorption cross-section of the nitrogen atom is larger than that of the carbon, and the cross-section reduces with increasing the photon energy. The sharp absorption edges around photon energies of ~280 eV and ~410 eV correspond to energies exceeding the ionization potentials for the 1*s* orbitals [199]. Hence, the x-ray absorption cross-section is strongly element-specific, and tuning of the photon energy can be efficiently used to perform localized ionization within the molecule [137, 138].

The mechanism for core-shell ionization after single x-ray photon absorption is shown in Figure 2.5 a, where an electron is directly transferred into a continuum from an inner shell. Further indirect ionization can occur by the inelastic second-order interactions of the ejected photoelectron with other bound electrons of the same atom. These can be broadly classified as shake-up and shake-off processes [138, 200]. In a shake-up process, a valence electron is transferred into an unoccupied orbital, and the photoelectron thereby loses a finite amount of kinetic energy. During a shake-off process, a valence orbital is ionized and finally resulted in two electrons in the continuum. These secondary processes lead to the release of low-energy electrons with an energy similar to that of photoelectrons released

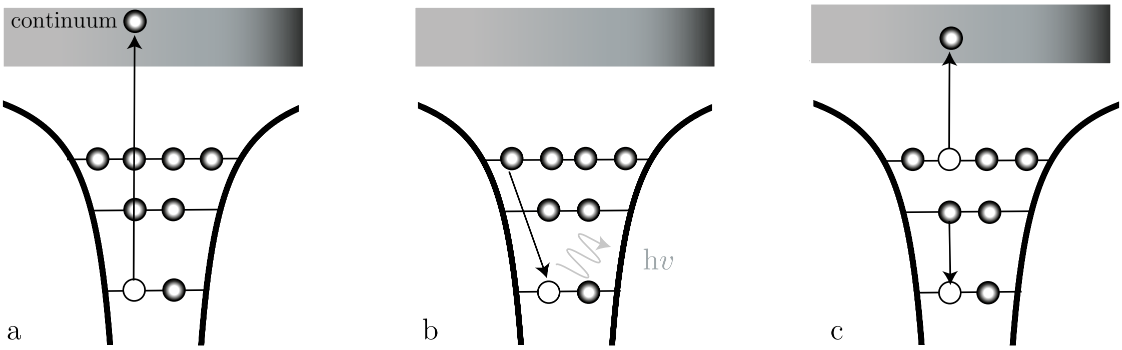

Figure 2.5. The schematic representation of x-ray ionization and relaxation processes. The black arrow represents the transition from one energy level to another, and the empty black circle denotes the vacancy created. a) The direct core-shell single ionization of the system results in the transfer of an electron into the continuum. b) Radiative relaxation process through fluorescence decay. c) Non-radiative relaxation process mediated by Auger decay resulted in a di-cationic state.

during outer-shell ionization.

After x-ray ionization, the unstable core-ionized species typically relax *via* two competing processes, i. e., either by fluorescence [139, 199] or Auger decay [201]. Fluorescence is a radiative relaxation process, where the vacancy created in the inner-shell is filled by an electron from the outer-shell, thereby emitting a photon as shown in Figure 2.5 b. On the other hand, an Auger decay is a non-radiative relaxation process resulted in the ejection of a second electron and is represented by Figure 2.5 c. In this process, the transition energy of the electron filling-up the inner-shell vacancy is transmitted *via* Coulomb interaction to ionize an outer-valence-shell. Therefore, Auger-decay results in the formation of a di-cationic state [139, 200]. The excess energy carried by the released Auger electron can cause further ionization or excitation of a valence orbital through a shake-off or shake-up process [139, 200]. This cascade effect result in the formation of multiply charged ions. The probability of fluorescence or Auger decay processes depends on the atomic number. The fluorescence is the dominant relaxation pathway for heavier atoms [139, 199], while for atoms with $Z < 10$, Auger decay dominates [139, 201]. Additional relaxations observed for the core-shell ionized molecules or molecular clusters are inter-atomic (molecular) coulomb decay (ICD) [143, 146–148, 151], proton-transfer mediated charge separation (PTMCS) [48, 202] and electron-transfer mediated decay (ETMD) [48, 151, 202], where two charge-separated molecular sites are formed.

2.4 Imaging the 3D momenta of ions

Coulomb explosion imaging is a widely used experimental technique to study the structure and fragmentation dynamics of molecules [132, 134]. The interaction of high-intense laser fields or x-rays with atoms, molecules, and clusters, can lead to multiple electron ejection, and thereby Coulomb explosion from highly charged cationic species. Measuring the 3D velocity vectors of the emitted ions and electrons can give insight into the underlying fragmentation dynamics. In this thesis, the Coulomb explosion imaging is explicitly used as a probe to study the fragmentation processes of cationic states of pyrrole and pyrrole(H_2O), as described in chapters 5 to 7.

2.4.1 Velocity map imaging spectrometer

Ion imaging techniques are widely used for imaging momenta vectors of ions produced through the photodissociation of the molecules, and thereby, following the chemical dynamics leading up to this process. In this thesis, a velocity map imaging spectrometer (VMIS) is employed- an experimental technique initially described by Eppink and Parker [203]. A schematic representation of a conventional VMIS is shown in Figure 2.6. It consists of three plates, which are the repeller, extractor, and ground plates. The electric field created by this electrostatic lens is used to map ions with the same initial parallel momenta into the same position on a 2D plane of a position-sensitive detector. Ions are produced by a focused laser beam in the interaction region, which is defined by the space between the extractor and the repeller electrode, also known as the extraction region. A specific set of voltages are applied to the extractor and repeller plates, to create the gradient field in the extraction region, which ensure that in velocity mapping the impact position of the charged particle on the detector plane is in first order independent of the exact position at which they originated in the interaction region. The third electrode is typically grounded or has the same potential as the flight tube so that accelerated ions fly in a field-free region, known as the drift-tube region, before they arrive at the detector. The flight time for the ions to reach the detector is proportional to $\sqrt{\frac{m}{q}}$, where m is the mass, and q is the charge of the ion. After velocity map imaging of the ions, the resulting radius on the detector plane is $R = \mathrm{M} \cdot v_r \cdot \mathrm{t_{tof}}$, where M is the magnification factor for the obtained image, v_r is the initial transverse velocity of the formed ion, and $\mathrm{t_{tof}}$ is the time-of-flight of the ion.

In a typical velocity map imaging experiment, a position-sensitive detector is used. One such option is a micro-channel plate (MCP) detector in combination with a fast phosphor screen, and corresponding images are commonly readout using charge-coupled device (CCD) or complementary metal-oxide-semiconductor (CMOS) cameras. These cameras are not fast enough to resolve the time-of-flight differences between different ion species, which typically are in the range of hundreds of nanoseconds to a few microseconds, and identification of the velocity map images of ions with different mass-to-charge ratios is difficult. Hence, the ions should be filtered out according to their arrival time on the detector $\mathrm{t_{tof}}$, to obtain the velocity map image of an ionic fragment with a specific mass-to-charge ratio. For this purpose, in typical experiments, the MCP is gated using a fast switch with a temporal gating window of a width of around 100 ns. As a consequence, this gating technique limits a simultaneous measurement of the velocity vectors of all created ions of different mass-to-charge ratios, which originated from the same ionization event. Though the combination of VMIS with a position-sensitive detector is a very powerful technique for measuring ions of

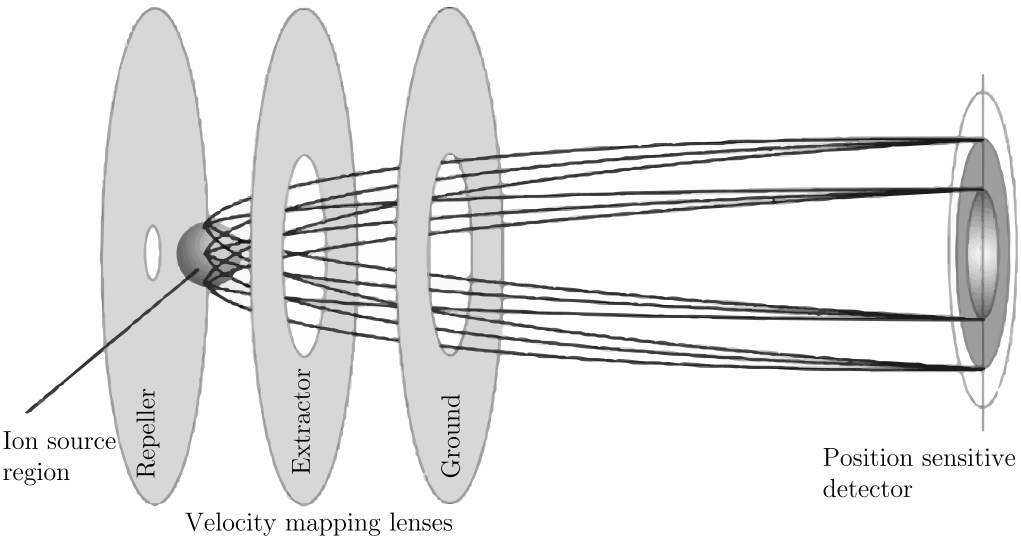

Figure 2.6. A schematic representation of a conventional velocity map imaging spectrometer, and it comprises of repeller, extractor, and ground plates. A position-sensitive detector is used to detect charged particles, and the electric field created by the VMIS lenses ensures that particles with the same initial parallel momenta are mapped to the same position on the 2D plane of the detector.

the same mass-to-charge ratios, on the other hand, it lacks the necessary time-sensitivity to distinguish ions of different mass-to-charge ratios. Also, imaging the velocity vectors of an ion on to the detector plane results in the crushing of the 3D-momenta sphere (so-called Newton's sphere) of the created ions onto a 2D-plane of the detector. Conventionally, the component of the velocity vector towards the detector plane (Z-component) can be retrieved from the velocity map image using an inverse Abel transform [204], provided there exists a cylindrical symmetry for the measured ion distribution (for example, linear polarization for laser beam), and the symmetry axis is parallel to the detector plane. However, in many experiments, we do not have such a well-defined symmetry axis. For instance, this can be due to the choice of laser polarization, the structure of the molecule, or even when the molecules are aligned or oriented in space.

2.4.2 Time and position sensitive detectors

The simultaneous measurement of the time-of-flight spectra and the velocity map images of all the ions created from an ionization event can be achieved on a shot-by-shot basis using time- and position-sensitive detectors. In such detectors, the component of the velocity vector towards the detector plane can also be directly measured using the temporal information, thereby enabling direct imaging of the 3D-momenta of ions. Hence, these time-stamping detectors provide the unique advantage of simultaneous determination of 3D-momenta of ions with different mass-to-charge ratios and are extremely beneficial for situations where one can not perform inverse Abel transform. Two such type detectors are used in this thesis in chapters 5 to 7: one is the delay-line detector [205], and the other is

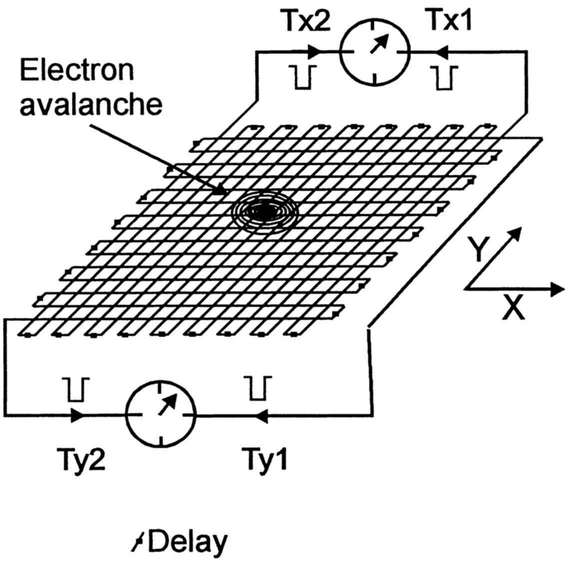

Figure 2.7. The working principle of a delay line anode is schematically represented. The X and Y position of a particle hit, i. e., where the electron cloud from the MCP hits the anode, is retrieved from the signal propagation time along the wires. The figure is taken from reference [205].

Timepix3 Camera [206].

A combination of MCP and delay-line anodes can be used for achieving the time and position information of a detected ion. The time-of-flight information of the hit is retrieved by directly measuring the MCP current as a function of time. The position information of the hit is obtained using an arrangement of orthogonal double-wires called the delay-line anode (Lecher-lines). A schematic representation of the function of the delay-line anode is shown in Figure 2.7. The delay line anodes are attached behind the MCP to collect the secondary electrons produced by a particle hit on the detector. The time-delay between current pulses measured at the two ends of the delay-line anode gives information about the position of the hit. For instance, the X position of the hit is proportional to $T_{x1} - T_{x2}$. A quadratic delay-line detector, with two sets of delay-line anodes that are oriented perpendicular to each other, is used to determine the X and Y positions of a hit on the detector as shown in Figure 2.7. For more detailed information, see reference [205]. The combination of MCP and delay-line anodes provides an excellent time resolution of ~100 ps [205]. The delay-line detector is limited to handle only a few hits per ionization event, i. e., one should work in a coincidence regime. The hexagonal version of anode pairs (three-sets of anode pairs) shows a slight improvement for multi-hit handling capability.

Next, an event-driven time-stamping fast optical camera Timepix3 with the potential for the time- and position-sensitive detection of the hits is discussed. For this, we implemented the Timepix3 camera to image ions, which were detected by the MCP-phosphor screen combination, as shown in the Figure 2.8 a. The detector is mounted outside the vacuum, and light flashes from the fast phosphor screen are focused on the sensor chip. The detector consists of a light-sensitive silicon sensor (256×256 pixels, each pixel of size

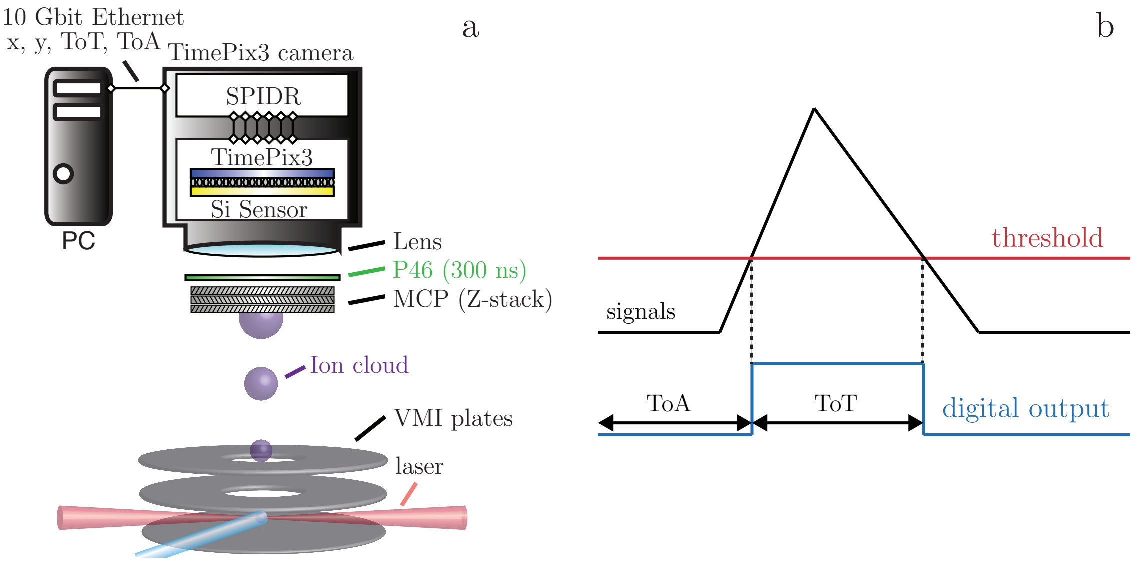

Figure 2.8. a) A schematic representation of the Timepix3 camera in combination with VMIS and MCP-phosphor screen is shown. b) The hit position (x,y) is imaged onto the Timepix3 Si sensor, which also records the time-of-arrival (ToA) and time-over-threshold (ToT) based on a threshold value set for the pixels.

55×55 µm^2) bound to a Speedy PIxel Detector Readout (SPIDER) chip for the time- and position-sensitive detection of the hits. Each pixel of the sensor acts independently as a fast digitizer, where a threshold value can be applied. If the detected signal overcomes the set threshold value, the timing information is recorded as time-of-arrival (ToA) and time-over-threshold (ToT), as represented in the Figure 2.8 b. The ToA gives the time it takes for the signal to overcome a predefined threshold value, whereas ToT is the duration of time signal stayed above the threshold value. The ToA can be used to determine the time-of-flight-information, and the ToT represents the amplitude of the signal. We utilized the home-built Pymepix [207] software for data handling and centroiding. A nominal time-resolution of 1.5 ns can be achieved using the Timepix3 camera [206]. A significant advantage of this detector over the delay-line anode is that it can handle multiple hits, and hence, measurements with higher counter rates are feasible. Another type of available event-driven detector is the Pixel Imaging Mass Spectrometry (PImMS) camera, which uses monolithic CMOS technology, and offers a time resolution of 12.5 ns [208, 209]. As a general remark, the sensor-based detectors only work in combination with a fast phosphor screen such as P46 or P47 [206–208].

2.5 Analysis of ion imaging data

In this thesis, the implementation of the aforementioned experimental methodologies described in the subsection 2.4.2 enabled us to simultaneously measure the 3D-momenta of all ionic products formed from the fragmentation of the cationic states of molecules, created after strong-field or soft x-ray ionization. To elucidate the correlated ions originated from

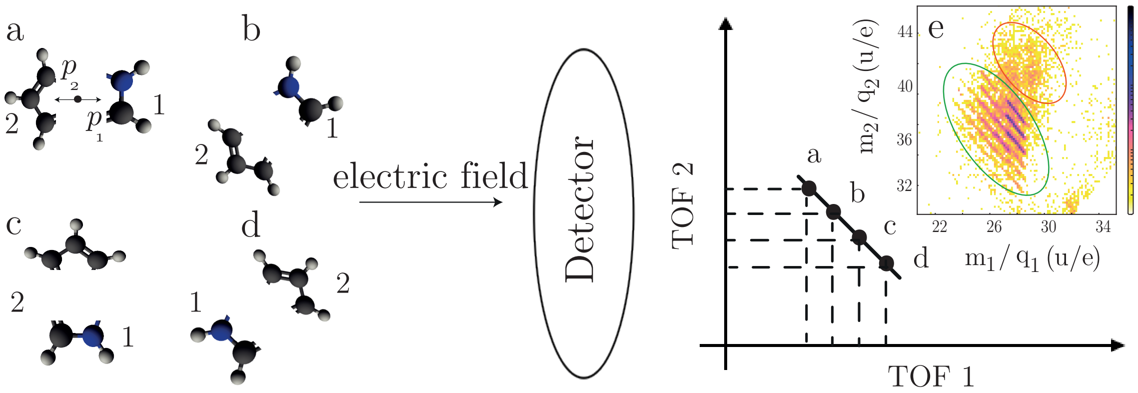

Figure 2.9. A schematic representation of the photoion-photoion coincidence (PIPICO) map for a specific fragmentation channel of pyrrole, for the four different orientations a), b), c), and d) of the molecule. e) An example of experimentally measured PIPCO spectrum of pyrrole. The region outlined in green color represents the real coincidences, whereas the region outlined by red color denotes the false coincidences.

the same ionization event, it requires to perform specialized data analysis. Two types of such analysis techniques were performed based on the signal level. The first one is the coincidence analysis, and the second one is the covariance analysis. A brief overview of these analysis techniques is described in this section, and the results of these analyses are given in chapters 5 to 7.

2.5.1 Coincidence map imaging

The coincidence map imaging technique is restricted to experimental conditions, where typically on an average at a maximum of one molecule is ionized in a given laser shot, known as the coincidence regime. A time-of-flight coincidence matrix can be built between two ions for all possible ion pair combinations on a shot-by-shot basis. A coincidence spectrum gives information about the ion pair, which is created from the same dissociation pathway after Coulomb explosion of molecules. Hence, it is a powerful technique to disentangle different fragmentation channels of a molecule.

A schematic representation of a Coulomb explosion channel of pyrrole and corresponding photoion-photoion coincidence (PIPICO) spectrum is shown in Figure 2.9. The figure shows a schematic of an axial two-body Coulomb explosion process of pyrrole, for the four different orientations a), b), c) and d) of the molecule. An extraction electric-field is used to direct the ions to the detector surface. The time-of-flight (TOF) of the ionic fragment depends on the mass-to-charge ratio of the fragment, as well as the orientation of its momentum vector (p) with respect to the detector plane. For the orientation of the molecule shown in a), the Coulomb exploding lighter ionic fragment (ion 1, $m/q = 28$ u/e) has a momentum vector (p_1) towards the detector and the heavy ionic fragment (ion 2, $m/q = 39$ u/e) has the momentum vector (p_2) initially pointing away from the detector plane. Hence, ion 1 will have a shorter TOF than ion 2, and the resulting PIPICO island is represented by the marked point a. Similarly, averaging of all different orientations of the molecule leads to a diagonal line in the PIPICO spectrum, as indicated in Figure 2.9. The slope and shape of a coincidence line (in m/q units) are determined by the mass-to-charge ratio of the fragments, as well as the angle between the momentum vectors of these ionic fragments [210]. For example, an experimental coincidence island corresponding to the Coulomb explosion of pyrrole is shown in Figure 2.9 e, and more details are mentioned in chapter 7. A sharp straight line coincidence between two ions (the region marked by green color) represents a recoil-frame Coulomb explosion process, where the total momentum is conserved. The washed-out coincidence lines are due to the correlation between two ions, which originated from a multi-body fragmentation process. A false coincidence island typically appear as a blob in the spectrum, as represented by the marked region in red color Figure 2.9 e. The real coincidences can be identified by checking the conservation of the total momentum in the recoil-frame for a given ion pair. In a two-body fragmentation process, the sum of the momenta of the two ions which fly in opposite directions should be a value within a small width around zero. On the other hand, for multi-body fragmentation channels, the conservation of momentum between the two detected fragments is no longer valid, and the width of the coincidence line (in m/q units) is directly proportional to the momenta of the undetected fragments.

2.5.2 Covariance map imaging

Covariance mapping is a widely used technique to obtain a statistical correlation between two random variables [211]. Covariance map techniques were applied previously to investigate the complex fragmentation dynamics of molecules after Coulomb explosion [212, 213]. This analysis is of great significance when the experimental conditions are far off from the coincidence regime, and the method is also well known to correct for false correlations. Covariance analysis can be performed on the time-of-flight [212] or velocity map image data of ions [213], which are measured on a shot-to-shot basis after the Coulomb explosion of molecules. Mathematically, the covariance matrix between two random variables x and y, measured n times, is given by,

$$\mathrm{cov}(x,y) = \frac{1}{n}\sum_{i=1}^{n}(x_i - \bar{x})(y_i - \bar{y}) = \frac{1}{n}\sum_{i=1}^{n}(x_i y_i) - \bar{x}\bar{y} \tag{2.11}$$

where x_i and y_i are i^{th} observables of variables x and y, whose expected (mean) values are $\bar{x}$ and $\bar{y}$ respectively. The above equation can be written in terms of expectation values as,

$$\mathrm{cov}(x,y) = \langle xy \rangle - \langle x \rangle \langle y \rangle. \tag{2.12}$$

The first term of the above equation (2.12) is a measure of how often the variables are observed to be correlated. However, it is required to mention that this might include events that are not correlated in reality (so-called false coincidences). The second term $\langle x \rangle \langle y \rangle$ measures how often both variables are observed independent to each other, and thereby, provides an estimate of the number of false coincidences. The subtraction of the second term from the first term yields the total covariance matrix, which is immune to false correlations. The positive value for the elements in the covariance matrix represents the real correlations between two variables, which are created from the same fragmentation process, in our case. Also, the area under each correlated island in a covariance map encodes the probability of that correlated channel (e. g. a specific fragmentation channel from Coulomb explosion of a molecule) to occur in a given laser shot [211, 212]. For the experiments performed in this thesis in chapter 6, a simple covariance analysis is performed using the equation (2.12). The contributions from the fluctuations or noise that add up to the desired signal can be removed by performing a partial covariance analysis [211]. The partial covariance analysis is more significant, for instance, in an experiment performed using a Free-Electron-Laser (FEL) source, where the shot-to-shot fluctuations are severe as compared to standard laser-based experiments.

3 Knife edge skimming for improved separation of molecular species by the deflector *

3.1 Introduction

Molecular-beam methods are important in physical chemistry and molecular physics as they provide unique opportunities to obtain fundamental insight into mechanisms and dynamics of elementary molecular and chemical processes. Furthermore, industrial applications using molecular beams range from the fabrication of thin films to the production of artificial structures such as quantum wires and dots.

Supersonic expansion of a gas into vacuum provides extreme cooling, in the case of atomic or seeded molecular beams typically from ambient or elevated temperatures down to $\sim$1 K [67]. This approach is used for a large variety of experiments. In many applications the molecular beam is shaped by skimmers, knife edges, razor blades, slits, slit-skimmers, or gratings to select only the most intense part of the beam [67, 111–114]. Furthermore, molecular beams can be manipulated by electric and magnetic fields which allow, e. g., the separation of the molecules from a seed gas [86, 93].

Spatial separation of different species is achieved by the electrostatic deflector [68, 86, 214]. Experiments are in this case typically performed at the edge of the deflected molecular beam to maximize the separation or to reduce the amount of signal originating from the seed gas. However, at this position of the beam profile the column density of molecules is rather low. In this note, we present the combination of a knife edge with the electrostatic deflector, which allows for a better separation of the different species of a molecular beam as well as an increase in column density in the interaction region.

3.2 Experimental setup

A schematic of the experimental setup is shown in Figure 3.1. A pulsed molecular beam was provided by expanding a few millibar of indole and a trace of water in 80 bar of helium through a position-adjustable Even-Lavie valve [73]. The valve was operated at a temperature of 110 °C and at a repetition rate of 250 Hz. Two transversely, in X–Y, adjustable conical skimmers (Beam Dynamics, model 50.8 with $\varnothing = 3.0$, model 40.5 with $\varnothing = 1.5$ mm) were placed 6.5 cm and 30.2 cm downstream from the nozzle, respectively.

---

[*] This chapter is based on the publication "*Knife edge skimming for improved separation of molecular species by the deflector*" by Sebastian Trippel, Melby Johny, Thomas Kierspel, Jolijn Onvlee, Helen Bieker, Hong Ye, Terry Mullins, Lars Gumprecht, Karol Długołęcki, and Jochen Küpper, *Rev. Sci. Instrum* **89**, 096110 (2018), *arXiv*:1802.04053. I contributed to the implementation of the experimental setup, recorded the data, analyzed the data, prepared figures for the manuscript, and contributed to the preparation of the manuscript.

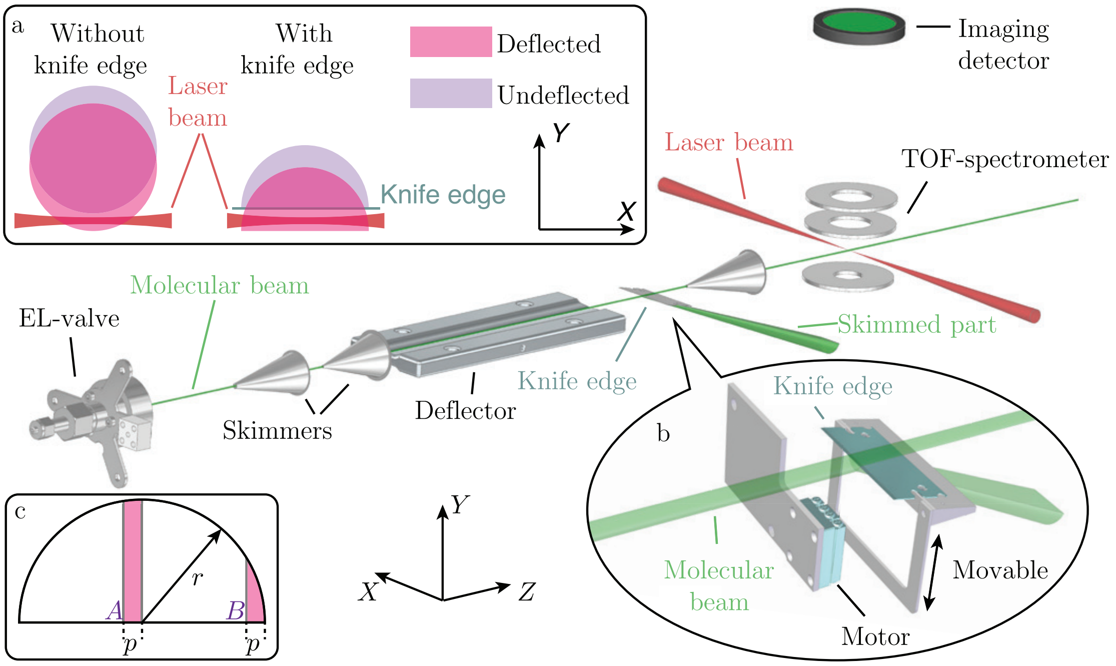

Figure 3.1. Schematic of the experimental setup and the definition of the coordinate system. The molecular beam, provided by supersonic expansion of indole, water, and helium from the Even-Lavie valve on the left passed two skimmers before entering the deflector. The knife edge and an additional skimmer were placed behind the deflector. In the center of a TOF mass spectrometer the molecular beam was crossed by the laser beam propagating along X, i. e., from front to back. a) Sketch of the cross sections of the molecular beam and the laser beam to illustrate the working principle of the knife edge. b) Zoom into the knife edge region, showing the mechanical setup and motorization. c) Definition of the volumes A and B, the beam radius r, and the width p used for the theoretical limit; see text for details.

The transversely adjustable electrostatic deflector was located 4.4 cm behind the tip of the second skimmer. Using the b-type electrostatic deflector [183], the molecular beam was dispersed according to the specific quantum states of the molecular species [76, 86, 214]. The vertically, Y, adjustable knife edge was placed 1.3 cm behind the end of the deflector.

For the measurements with knife edge its vertical position was chosen such that the undeflected molecular beam was cut roughly in its center. For the measurements without knife edge it was moved vertically out of the molecular beam. A third, transversely adjustable skimmer (Beam Dynamics, model 50.8 with $\varnothing = 1.5$ mm) was placed 2.5 cm downstream of the front of the knife edge. The molecular beam entered a time of flight mass spectrometer (TOF-MS) centered 17.6 cm downstream of the last skimmer, where the molecules and clusters were strong-field ionized by a laser pulse with a pulse duration of 30 fs, centered at a wavelength of 800 nm, and focused to $\varnothing \approx 50$ µm. Figure 3.1 a shows a cross section, in the X–Y plane, of the molecular beam to schematically illustrate the working principle of the knife edge. On the left, a molecular beam profile defined by the shape of a round skimmer is depicted. Its deflected part is shown by a vertical shift. On the right, the corresponding profiles are depicted for the case with the knife edge. The laser probes the molecules in the deflected part of the beam, resulting in a higher column density compared to the case without knife edge. Figure 3.1 b highlights the region of the setup where the knife edge was located. It depicts the knife edge with its holder which was mounted on a motor (SmarAct SLC-1750-S-UHV) which allows to position the knife edge vertically. The molecular beam is indicated by the green cylinder which is cut into halves by the knife edge.

3.3 Results

We used the separation of indole and indole-water clusters to demonstrate the advantage of using the knife edge in combination with the electrostatic deflector. Figure 3.2 a shows the measured vertical density profiles of the undeflected and deflected molecular beam when the knife edge was used. The TOF mass spectrum was gated on specific masses, which corresponded to either parent ions or specific fragments, to obtain each individual profile. The undeflected (0 kV) profile of the signal corresponding to the indole mass of $m = 117$ u is shown in dark blue. All molecules and clusters were deflected downwards when voltages of ±10 kV were applied to the deflector electrodes, as all quantum states were high-field seeking at the electric field strengths experienced inside the deflector [86]. The deflection profiles for the gates set to the masses of indole, indole(H_2O), indole(H_2O)$_2$ and (indole)$_2$ are shown in red, black, green, and orange, respectively. The profiles for indole(H_2O), indole(H_2O)$_2$, and (indole)$_2$ were multiplied by a factor of five. The indole(H_2O)$_3$ cluster was not observed in the mass spectrum. Furthermore, the profile of indole$\cdots H_2O$ had the same shape as the one for (indole)$_2$ and is not shown in the figure. Several edges were observed in the profiles which correspond to various molecules and fragments. Going from left to right, the outermost edge at -1.25 mm is attributed to indole(H_2O) because this cluster showed the largest Stark effect of all molecules and clusters to be considered and was, therefore, deflected the most [76, 86]. The shape of this edge matches the corresponding edge in the indole-ion profile, which confirms that the indole(H_2O) ion was fragmenting to indole ion with a probability of ~53 %. The edge at -0.9 mm in the indole-cation signal was attributed to the indole monomer, since indole had the second largest Stark effect. The edge on top of the indole(H_2O) profile at -0.6 mm was produced by indole(H_2O)$_2$ clusters which fragmented into indole(H_2O) with a probability of ~64 %. A better separation of C_8H_7N–H_2O from indole and higher clusters was observed in comparison to our previous experiments on this system without the knife edge [76, 86]. Furthermore, the edge for the indole(H_2O)$_2$ cluster has now been observed for the first time.

Figure 3.2 b shows the measured deflection profiles for indole corrected by the known fragmentation probabilities to account for the fragmentation for the case with and without knife edge (Knife) and the deflector switched on (red) and off (blue). The profiles for the case without knife edge were shifted by 0.975 mm to the left to match the edges on the

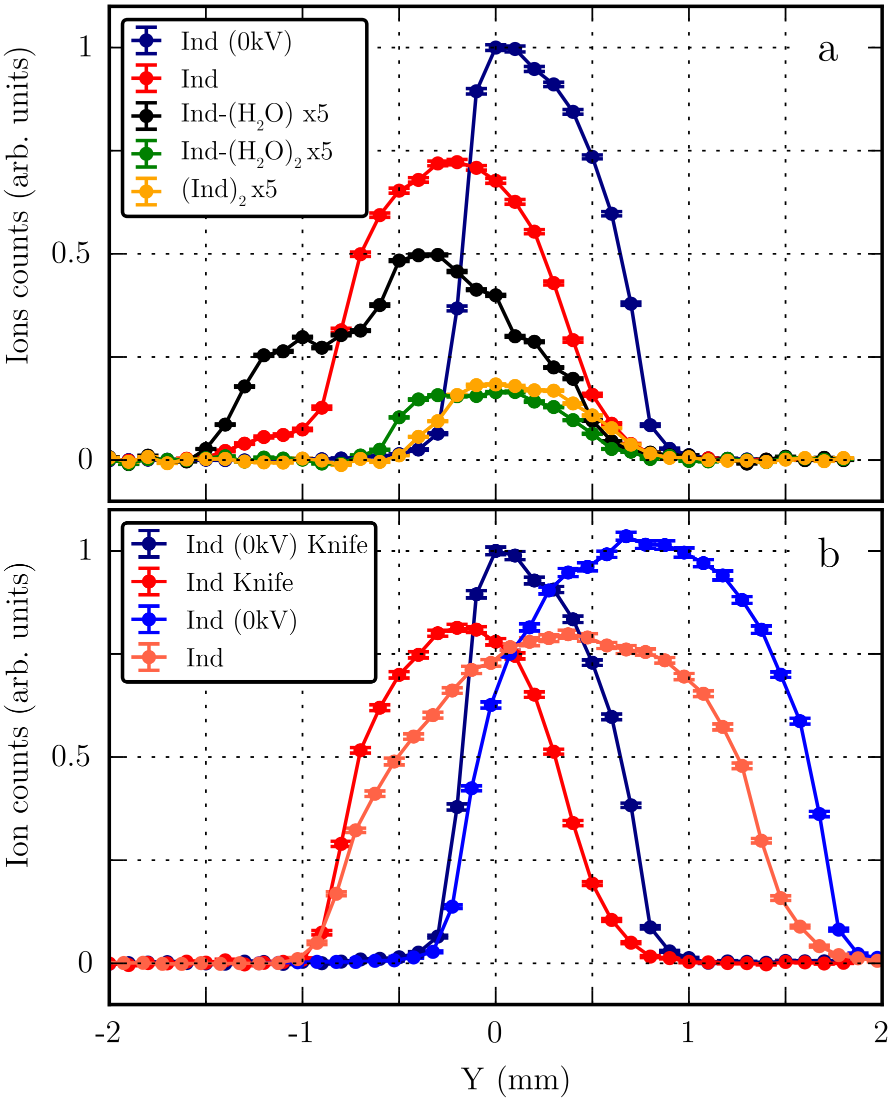

Figure 3.2. (Color online) a) Column density profile of indole (Ind) in dark blue, and deflection curves of various species (colored). b) Column density profiles with the deflector switched on (red) and off (0 kV, blue) with and without knife edge (Knife).

left side for a better direct comparison. In both cases – deflector on and off – the left edge was steeper for the measurements with knife edge. This is attributed to the higher column density as a result of the knife edge. Placing the probe laser at -0.7 mm in the deflected profile results in an enhancement factor of $R = 1.5$ at this position. The measured molecular beam diameter of $r = 2$ mm matches exactly the expected radius from geometry arguments assuming a point source for the molecular beam. The distances between the valve and the third skimmer and the interaction region are 53.4 cm and 71 cm, respectively. This results in a magnification factor of $71.0/53.4 = 1.33$, in excellent agreement with the ratio between the measured molecular-beam diameter and the skimmer diameter given by $2.0/1.5 = 1.33$. The deflected part of the molecular beam is, therefore, also expected to be far out of the geometric helium profile. Additional broadening mechanisms for the molecular beam, such as the finite temperature or deviations from a point source are not taken into account. The influence of these contributions to the purity of the molecular beam are beyond the scope of this manuscript.

3.4 Discussion

The maximum enhancement factor R for the increase in column density can be estimated, assuming an uniform molecular beam emitted from a point source and a uniform deflection force, from the molecular beam radius r in the interaction region and the width of the, for the interaction with the molecules relevant, volume p. For $p \ll r$ the enhancement factor is given by $R = A/B = 3/4\sqrt{2r/p}$, see Figure 3.1 c. Taking the radius of our measured molecular beam profile of $r = 1.0$ mm and the diameter of the ionization laser $p = 50$ µm resulted in an expected enhancement factor of $R \approx 4.7$. We attribute the reduced experimentally observed enhancement factor of $R = 1.5$ to the following reasons: The experimental molecular beam profile was not collimated and, therefore, the edges of the profiles are not infinitely steep. Secondly, the important volume for the interaction of the molecules with the ionization laser was unknown and might be broader than the measured diameter in intensity. A third contribution to the reduced enhancement is attributed to the fact that the deflector acts as a thick lens for the dispersion of the molecular beam which leads to a softening of the edges. A further contribution could be a misalignment of the knife edge with respect to the propagation direction of the probe laser.

3.5 Conclusion

The combination of the knife edge with the electrostatic deflector is of general use for all molecular beam experiments that benefit from a strong separation of molecular species or a strong separation from the seed gas. The presented approach is also especially useful for applications with low count rates or restricted measurement times, e. g., beamtimes at large facilities such as free electron lasers (FELs), synchrotrons, or high-power-laser facilities, where typically only a few days of beamtime are available for the measurements. Furthermore, for probing a collimated molecular beam with $r = 2$ mm by the generally small x-ray beams, e. g., $p = 5$ µm, a theoretical enhancement factor of $R > 20$ is obtained, in line with preliminary results from a recent beamtime at the LCLS.

4 Spatial separation of pyrrole and pyrrole(H_2O) *

4.1 Introduction

Studies of solvation effects of biologically relevant aromatic molecules provide details on the influence of the molecule's local environment on its function and on the nature of molecular interactions, as well as insights into the functions of complex biological systems [23]. Prototypical model chromophores such as imidazole and pyrrole were used to build synthetic polyamide ligands for the recognition of the Watson–Crick base pairs in the DNA minor groove [215]. Furthermore, pyrrole is a model of tryptophan's indole chromophore, one of the strongest near-UV absorbers in proteins. Similarly, pyrrole is responsible for the photoconversion mechanism in the phytochrome enzyme [51] and it is a promising building block for organic dye-sensitized solar cells [216] as well as biological sensors [217].

A key reason for the intriguing photophysics of the above-mentioned chromophores is the excited $^1\pi\sigma^*$ state, which is repulsive along the N-H-stretching coordinate [53, 218, 219]. The photophysics and photochemistry of these molecules is fairly sensitive to the environment [56]. In a bottom-up approach, spectroscopic and theoretical investigations were performed for micro-solvated clusters to get fundamental insights into their photophysical and photochemical properties [55, 218, 220]. Recently performed experiments have provided evidence for ultrafast intermolecular relaxation processes in electronically-excited microsolvated tetrahydrofuran-water [149] and indole-water [221] clusters. This reflects one of the proposed efficient mechanisms for radiation damage processes of biomolecules via auto-ionization caused by secondary electrons [32]. Time-resolved experiments, such as photoion and photoelectron spectroscopy, aiming at the investigation of the photophysics and photochemistry of pyrrole, were performed to study the dynamics of H elimination from the N-H site of the molecule mediated by the excitation of the $^1\pi\sigma^*$ state [52, 218, 222, 223].

For pyrrole(H_2O) clusters theoretical calculations predict that an electron is transferred across the hydrogen bond without photodissociation of the pyrrole moiety [56, 219]. Hence, detailed investigations of the photophysics of pyrrole(H_2O), and their comparison with the existing observations for indole(H_2O) [218, 220], promises to unravel these fundamental processes in the intermolecular interactions as well as the radiation damage of biological systems.

Advanced experiments aiming at unraveling these ultrafast dynamics often rely on pure samples of the individual species. Such controlled samples were previously exploited in

---

[*] This chapter is based on the publication "*Spatial separation of pyrrole and pyrrole-water clusters*" by Melby Johny, Jolijn Onvlee, Thomas Kierspel, Helen Bieker, Sebastian Trippel, and Jochen Küpper, *Chem. Phys. Lett* **721**, 149 (2019), *arXiv*:1901.05267. I contributed to the experiment, recorded the data, analyzed the data, performed simulations, discussed the results with some authors, and wrote the manuscript.

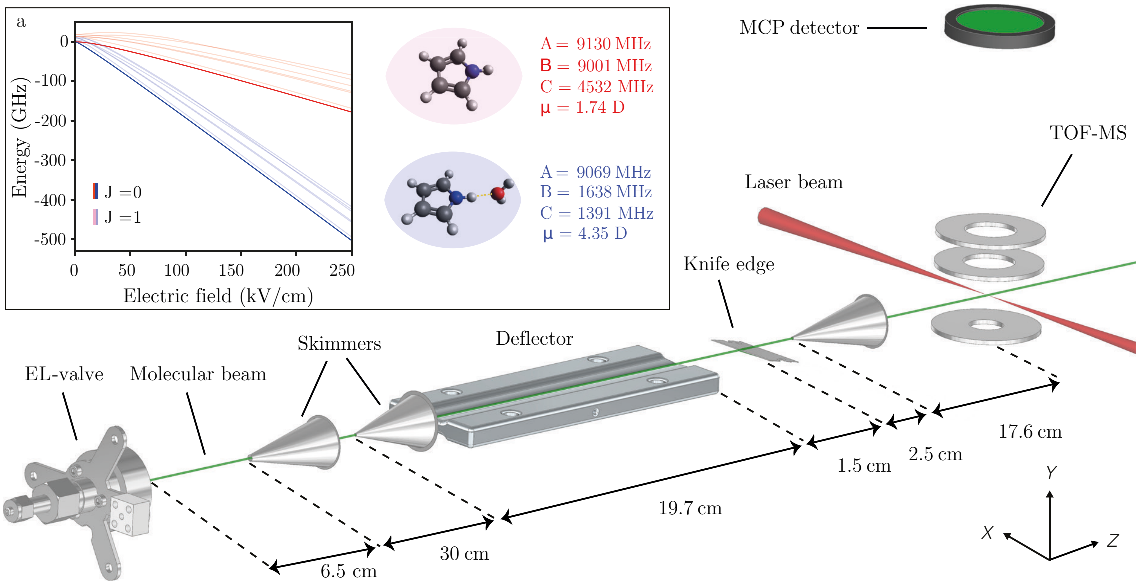

Figure 4.1. Schematic representation of the experimental setup and the definition of the coordinate system. (a) Stark energies and molecular constants of pyrrole (red) and pyrrole(H_2O) (blue).

investigations of the photophysics of indole [162] and indole(H_2O) clusters [221] following site-specific soft x-ray ionization and are even amenable to coherent-x-ray-diffraction studies [65]. These experiments relied on the spatial separation of individual species by the electrostatic deflector [86], which was previously demonstrated for the separation of indole(H_2O) from indole [76, 86, 224].

Here, we demonstrate the spatial separation of pyrrole, a sub unit of indole and tryptophan, and the microsolvated pyrrole(H_2O) cluster. The structure of pyrrole and pyrrole(H_2O) was studied using microwave spectroscopy [50, 225] and it was concluded that the singly-hydrogen-bonded pyrrole(H_2O) cluster has a well defined structure, with the water attached to the N-H site of pyrrole [50, 219].

4.2 Experimental setup

A schematic representation of the experimental setup is shown in Figure 4.1. An Even-Lavie valve [73] was used to generate a pulsed molecular beam by supersonic expansion of a few millibar of pyrrole (Sigma Aldrich, > 98 %) and traces of water seeded in ~80 bar of helium into vacuum. The valve was operated at a repetition rate of 250 Hz and was heated to $65\,^\circ$C. The expanded molecular beam was then skimmed twice using conical skimmers (Beam Dynamics, model 50.8, $\varnothing = 3.0$ mm & model 40.5, $\varnothing = 1.5$ mm), which were placed at distances of 6.5 cm and 30.2 cm downstream the nozzle, respectively. An inhomogeneous electric field created by the so-called b-type deflector [183] was used to disperse the molecular beam according to the species' effective-dipole-moment-to-mass ratio [86, 214, 226]. The molecular beam was cut by a vertically adjustable knife edge placed 1.5 cm downstream of the exit of the deflector, which allowed for an improved separation of all species present in the molecular beam [224]. The experiments were conducted by placing the knife edge at a height where it cut off the undeflected (0 kV applied on deflector electrodes) molecular beam at the center of the vertical column density profile. The molecular beam was further skimmed by a conical skimmer (Beam Dynamics, model 50.8 with $\varnothing = 1.5$ mm) placed 4 cm downstream of the exit of the deflector. The transverse positions of the valve, skimmers, and the deflector were adjustable using motorized translation stages. A laser pulse with a duration of ~30 fs, a wavelength centered at 800 nm, focused to $\varnothing \approx 50$ µm, and directed perpendicular to the molecular beam ionized molecules in the extraction region of a time-of-flight mass-spectrometer (TOF-MS) placed 17.6 cm downstream of the last skimmer. The peak intensity of the laser pulse was $\sim 2 \times 10^{14}$ W/cm^2. The ions generated due to the strong-field ionization were detected using a micro-channel plate (MCP), operated in single-shot readout.

4.3 Results and discussions

Figure 4.1 a shows the structure, rotational constants [50, 225], permanent dipole moment [50, 225], and the Stark energies of pyrrole (red curves) and pyrrole(H_2O) (blue curves) for the $J = 0,1$ rotational states. The Stark energies were calculated using CMIstark [179] within the rigid-rotor approximation, as justified by previous experimental and theoretical work on the indole(H_2O) cluster [76, 116]. Pyrrole has a ~64 % smaller Stark-energy shift than pyrrole(H_2O) for the $J = 0$ rotational state at an electric field strength of $E \approx 200$ kV/cm. This enabled full spatial separation of pyrrole(H_2O) from pyrrole in a cold molecular beam using the electrostatic deflector.

The molecular beam species underwent fragmentation following the strong-field-ionization process. Hence contributions of ionic fragments from larger clusters in specific mass gates were observed in our spectra. A ~28 % probability of pyrrole(H_2O) fragmenting into pyrrole$^+$ was experimentally obtained for our specific laser pulse properties. A detailed description of the fragmentation ratios and utilized mass gates for the specific ion signals is presented in the Supplementary Information. The fragmentation-corrected vertical column density profile for undeflected pyrrole is shown as black dots in Figure 4.4 a. The undeflected profiles of pyrrole(H_2O) and other species in the TOF-MS spectra had similar shapes and are not shown. In addition, the fragmentation corrected deflection profiles of both, pyrrole (red dots) and pyrrole(H_2O) (blue dots), are shown for voltages of ±7 kV applied across the deflector. All quantum states are strong-field seeking at the relevant electric field strengths experienced by the investigated molecules and clusters inside the deflector. Therefore, all species are deflected downward, in the negative Y direction [183]. The experimental deflection profile of pyrrole(H_2O) shows the strongest deflection, down to $Y = -1.8$ mm, whereas pyrrole was only deflected down to $Y = -1.2$ mm. Significant deflection of H_2O is not expected due to its small effective dipole moment [185]. Larger cluster species, e. g.,

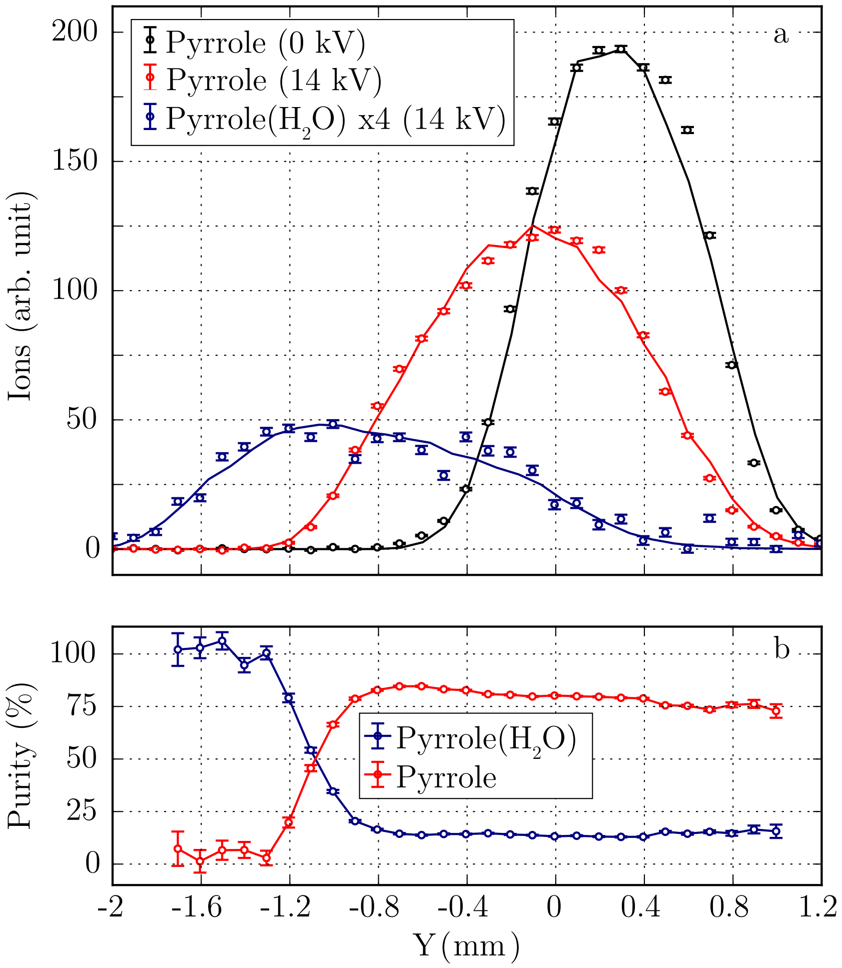

Figure 4.2. a) Measured vertical column density profiles for the undeflected (0 kV) pyrrole (black dots), deflected (14 kV) pyrrole (red dots) and pyrrole(H_2O) (blue dots). Solid lines are the corresponding simulated profiles. b) Purity of pyrrole (red) and pyrrole(H_2O) (blue).

pyrrole(H_2O)$_2$ and pyrrole)$_2$, are also deflected less than pyrrole and pyrrole(H_2O); these deflection profiles are shown and discussed in the Supplementary Information.

The solid lines in Figure 4.4 a are simulated profiles obtained from the results of Monte-Carlo trajectory calculations that take into account the geometrical constraints of the mechanical apertures in the experimental setup [214]. These simulated deflection profiles of pyrrole and pyrrole(H_2O) matched the experimental data assuming an initial rotational temperature of the molecular beam entering the deflector of $T_{\text{rot}} = 0.8 \pm\ 0.2$ K. In the deflected part of the beam at $Y = -1.6$ mm the relative populations of the rotational states of pyrrole(H_2O) were determined from the simulations. Although this rotational-state distribution is non-thermal, it approximately corresponds to a thermal distribution of 0.4 K, see Supplementary Information. This indicates that an ensemble of very cold molecules is generated using the deflector [104, 227] and that ultracold ensembles, even of isolated well-defined molecular clusters, can be generated in the most deflected part of a dispersed molecular beam.

The purities of pyrrole and pyrrole(H_2O), as defined by the ratio of the specific signals to the sum of signals of all other species observed is shown in Figure 4.4 b, see Supplementary Information for details of the analysis. This demonstrates that a molecular beam of pyrrole(H_2O) with a purity of ∼100 % was produced at vertical positions $-1.8\text{ mm} < Y < -1.3\text{ mm}$. The column density profile of helium is not shown here, but is expected to be only slightly broader than the undeflected (0 kV) profile of the molecular species, owing to its lighter mass. Furthermore, helium is expected to be only marginally deflected by a few µm due to its small polarizability [183]. Hence, the extracted pure molecular beam of pyrrole(H_2O) should also be free from helium gas at $Y < -1$ mm.

4.4 Conclusion

We demonstrated the spatial separation of the pyrrole(H_2O) cluster in a molecular beam, i. e., from pyrrole, water, larger clusters, and the seed gas. A purity of ∼100 % of pyrrole(H_2O) was obtained in the most deflected part of the molecular beam. Simulated deflection profiles were in excellent agreement with the experiment. They yielded a rotational temperature of $T_{\text{rot}} = 0.8 \pm 0.2$ K in the initial molecular beam for both, pyrrole and pyrrole(H_2O), and of $T_{\text{rot}} \approx 0.4$ K in the deflected pure pyrrole(H_2O) beam.

These pure beams of pyrrole(H_2O) provide a crucial ingredient for photophysics studies aiming at time-resolved hydrogen bond formation/dissociation dynamics, e. g., in ultrafast laser pump and x-ray probe experiments. Further interesting aspects will be the control of the orientation in the laboratory frame by laser aligning or mixed-field orienting pyrrole(H_2O) clusters [104, 115, 116]. The separated pure species are also ideally suited for experiments to image the structure and dynamics of the pyrrole(H_2O) complex in the molecular frame, e. g., through molecular-frame photoelectron angular distributions (MFPADs), gas-phase x-ray diffraction, or laser-induced electron diffraction (LIED) experiments [65, 103, 228, 229].

4.5 Supplementary Information

The mass spectrum of the molecular beam after strong field ionization, recorded in the center of the undeflected (0 kV) molecular beam profile, is shown in Figure 4.3. In the spectrum, mass peaks that correspond to pyrrole$^+$, pyrrole(H_2O)$^+$, pyrrole$(H_2O)_2^+$, pyrrole$)_2^+$, (pyrrole)$_2$(H_2O)$^+$, (pyrrole)$_2$$(H_2O)_2^+$, pyrrole$(H_2O)_3^+$, and larger clusters were observed. Column-densities were obtained by integrating the mass spectrum within gates ±0.5 u/e around the nominal masses of pyrrole$^+$, pyrrole(H_2O)$^+$, pyrrole$)_2^+$, and pyrrole$(H_2O)_2^+$; the resulting vertical beam profiles are shown in Figure 4.4 a.

The plotted profiles are for undeflected pyrrole$^+$ (0 kV) and deflected (14 kV) molecular-beam species without any fragmentation correction. The profiles of all species were scaled to the undeflected profile of pyrrole$^+$ for an improved visibility, see the legend of Figure 4.4 a for the scaling factors used in the plot. The amount of deflection was in the following order: pyrrole(H_2O)$^+$ $>$ pyrrole$^+$ $>$ pyrrole(H_2O)$_2^+$ $>$ pyrrole)$_2^+$. Water is expected to deflect less than pyrrole)$_2$ because of its small effective dipole moment at the electric field strengths used in the experiment. The fragmentation of pyrrole(H_2O)$^+$ into the pyrrole$^+$ ion is evident from the matching shape of the deflection profile of pyrrole$^+$ with that of pyrrole(H_2O)$^+$ at vertical positions -1.8 mm $< Y < -1.4$ mm. This manifests itself in a constant ratio $R = S(\text{pyrrole}(H_2O)^+)/S(\text{pyrrole}^+)$ of the specific integrated signals $S(j)$ of the species j in that region as shown in Figure 4.4 c. We have corrected for the contribution of the fragmentation of pyrrole(H_2O)$^+$ into the pyrrole$^+$ channel using the mean value of the ratio R between vertical positions -1.8 mm $< Y < -1.4$ mm, $R = S(\text{pyrrole}(H_2O)^+)/S(\text{pyrrole}^+) = 0.38$.

The deflection profile of pyrrole(H_2O) was also corrected for the fragmentation from larger clusters. For this the width of the TOF-MS peak of pure pyrrole(H_2O)$^+$ in the most deflected part of the beam ($Y = -1.5$ mm) was compared with the width of the pyrrole(H_2O)$^+$ peak in the center ($Y = 0$ mm) of the molecular beam profile where we have contribution from higher clusters, Figure 4.4 e. The TOF-MS of pyrrole(H_2O)$^+$ with contribution from larger clusters (red curve) was broader than the one of the deflected pure pyrrole(H_2O)$^+$ beam (black curve). This is attributed to the kinetic-energy release upon cluster fragmentation; analyzing this allowed us to correct for these contributions. The vertical column density profiles in Figure 4.4 d obtained by setting gates to the wings of the TOF-MS peak (green line, $m/q = 85.02$–85.10 u/e and red line, $m/q = 84.88$–84.96 u/e) were scaled to the least deflected part of the pyrrole(H_2O)$^+$ signal ($m/q = 85 \pm 0.5$ u/e) at 0.2 mm $< Y < 1$ mm, with a scaling factor of 10. The fragmentation corrected pyrrole(H_2O)$^+$

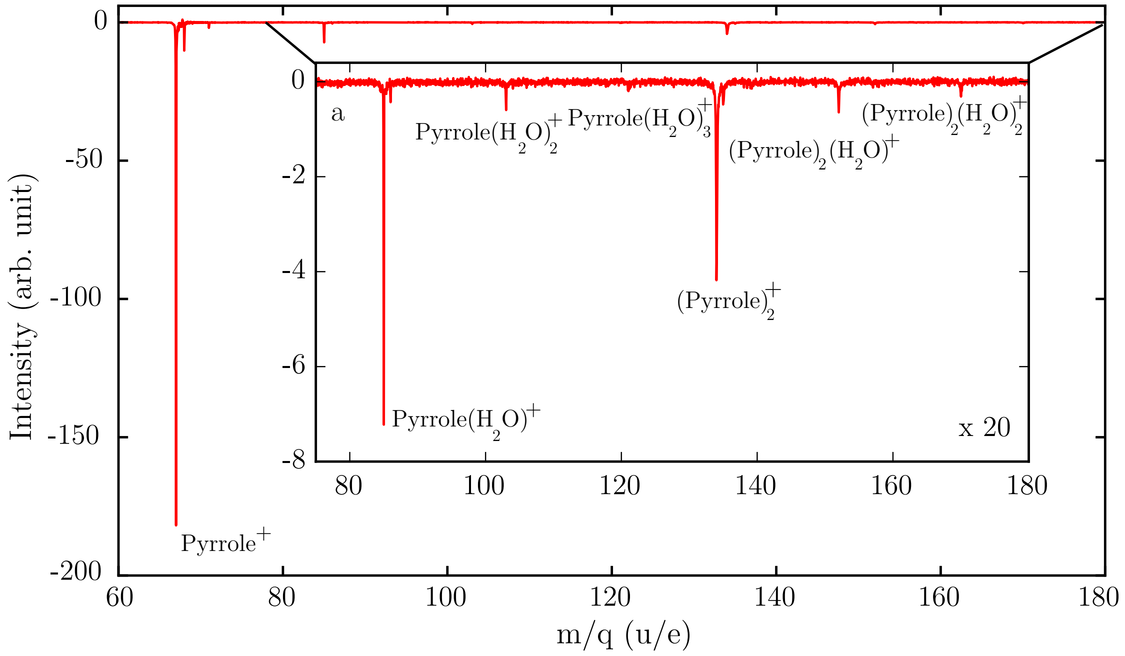

Figure 4.3. The mass spectra of pyrrole monomer, and larger clusters of pyrrole and water. a) Zoom in of the mass spectrum for clusters.

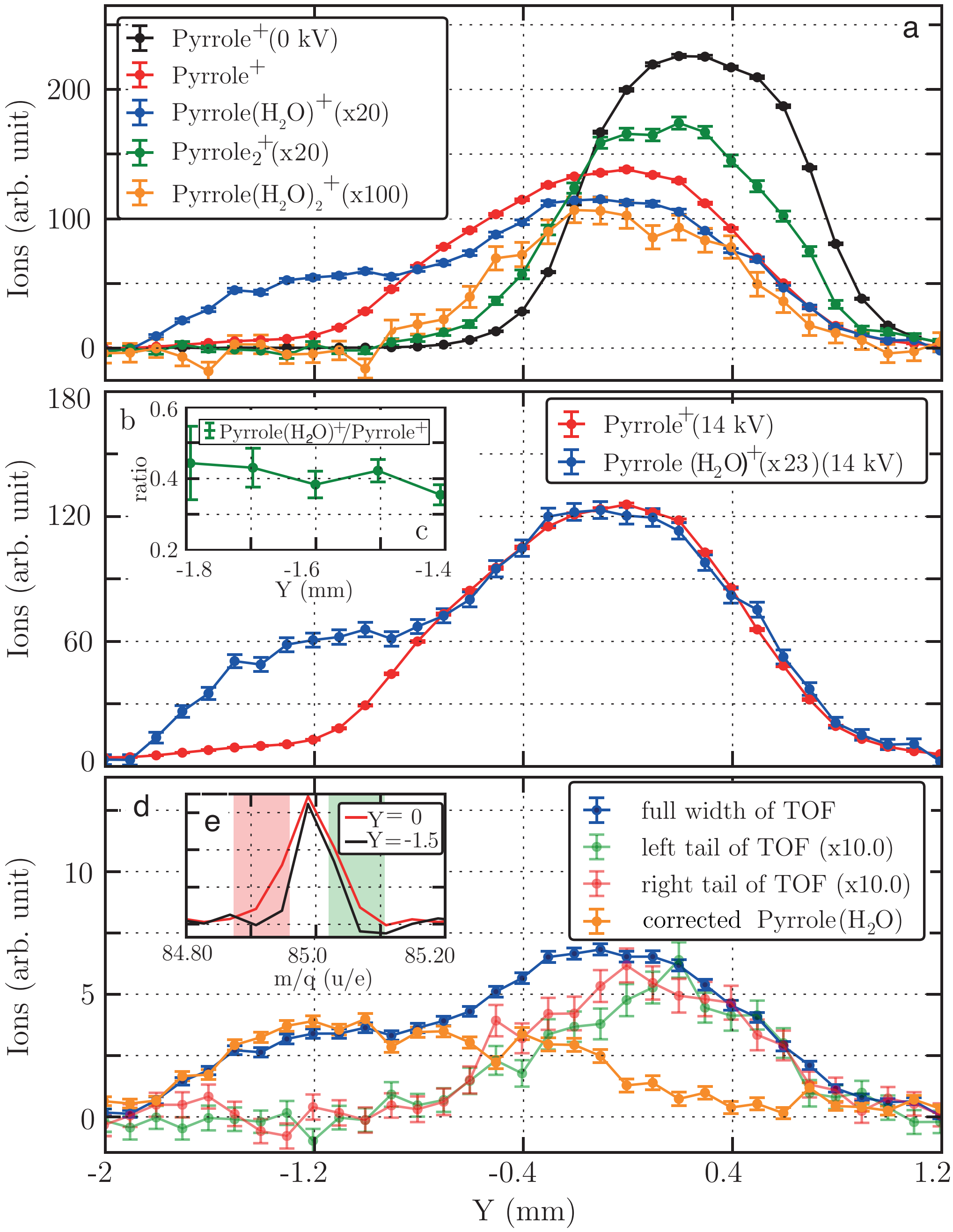

Figure 4.4. a) Vertical column density profiles recorded for various ion channels. b) Vertical column density profiles of deflected (14 kV) pyrrole$^+$ and pyrrole(H_2O)$^+$. c) Ratio of pyrrole(H_2O)$^+$/pyrrole$^+$ at positions -1.8 mm $< Y < -1.4$ mm. d) Molecular beam profile of pyrrole(H_2O) with gates covering the full-width of the TOF-MS peak (blue, $m/q = 85 \pm 0.5$ u/e) and curves corresponding to the vertical profile of pyrrole(H_2O) with gates set to the wings of TOF-MS peak (red and green), i. e., the red ($m/q = 84.88$–84.96 u/e) and green ($m/q = 85.02$–85.10 u/e) shaded regions shown in the inset, e). The orange curve corresponds to the fragmentation corrected column density profile of pyrrole(H_2O). e) TOF-MS of deflected (14 kV) pyrrole(H_2O)$^+$ at vertical position $Y = 0$ (red) and of pure pyrrole(H_2O) beam at $Y = -1.5$ mm (black, $m/q = 85 \pm 0.5$ u/e).

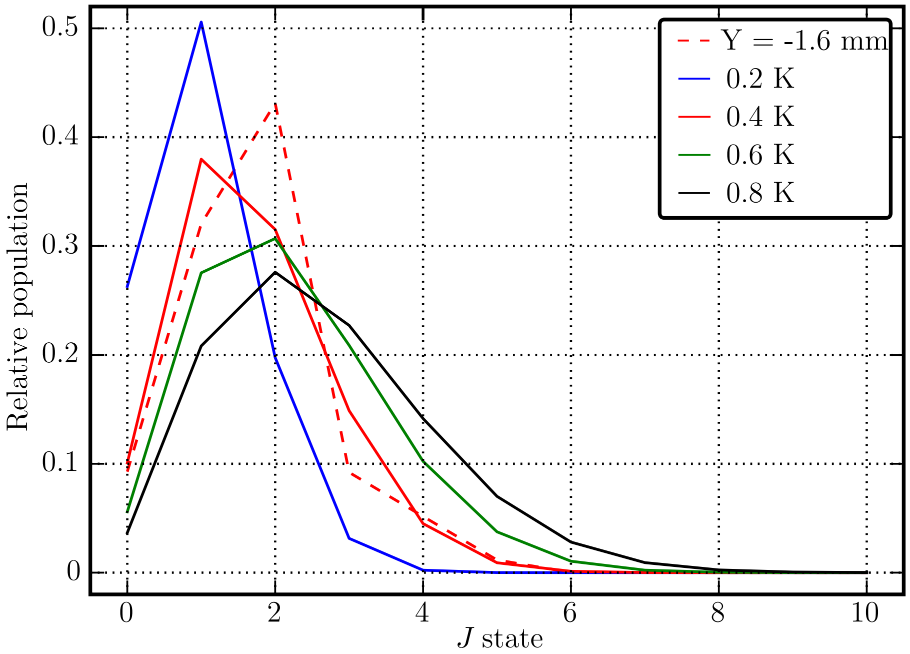

Figure 4.5. The relative population of the rotational states in the molecular beam at $Y = -1.6$ mm (dashed line) and the thermal distributions at various temperatures (solid lines).

profile (orange line) was obtained by subtracting these larger-cluster-fragment corrections (green and red lines) from the profile obtained by setting gates to the full width of the TOF-MS peak (blue line, $m/q = 85 \pm 0.5$ u/e). The step at vertical positions ranging from $Y = -0.3$ to -0.8 mm (blue line) and the shape of the profiles for larger clusters (red and green lines) matched the shape of the deflected pyrrole$(H_2O)_2^+$ in Figure 4.4 a. Hence, the uncorrected pyrrole$(H_2O)^+$ profile had significant contributions from fragments of larger, weakly deflected, pyrrole$(H_2O)_2^+$ cluster into the pyrrole$(H_2O)^+$ channel.

The purity P_i of a species i is defined by $P_i = S(i^+)/\sum_j S(j^+)$. For our evaluation of the purity, integrated signals from pyrrole$^+$, pyrrole$(H_2O)^+$, pyrrole$(H_2O)_2^+$, pyrrole$)_2^+$, (pyrrole$)_2(H_2O)^+$, and (pyrrole$)_2(H_2O)_2^+$ were taken into account; larger clusters were neglected.

The relative populations of rotational states of pyrrole(H_2O) in the molecular beam at $Y = -1.6$ mm were determined from the simulations, see Figure 4.5; this distribution is non-thermal due to the nature of the deflection process. The rotational state distribution for a range of temperatures are also shown in the plot. The relative populations in the deflected part of the beam match fairly well with a thermal distribution of $T_{\mathrm{rot}} = 0.4$ K. This confirms that ultracold molecular beams, even of isolated well-defined molecular clusters, can be generated in the most deflected part of a dispersed molecular beam.

5 Molecular sunscreen: water protects pyrrole from radiation damage *

5.1 Introduction

The damage of biological matter upon the interaction with UV radiation [8] or ionizing radiation [31], such as x-rays [31, 32], γ-rays [45], and α- [33], or other fast charged particles [32, 34, 39] is a major environmental impact on living organisms [8, 31]. For instance, inner-shell-, inner-valence-, or outer-valence-ionized states can relax in various pathways that form cationic species, which can result in molecular fragmentation [32, 146, 147]. In addition, recent studies show that one highly relevant mechanism of DNA strand breaks is *via* autoionization or excitation caused by low-energy secondary electrons [32, 34, 35, 39].

Regarding the radiation damage of molecules, ionization and excitation are similar: Vacancies are created in the occupied molecular orbitals in both cases, which can lead to corresponding bond breaking. In the case of ionization, the electron is directly transferred to the continuum, leaving the molecule, while excitation may result in the population of dissociative excited states [230, 231]. Typical sources for single ionization of biological matter in aqueous environments are deep UV ionization or the interaction with radicals, slow electrons, or ions [31, 32, 231, 232]. While deep UV radiation is efficiently blocked by the earth's atmosphere [233] it is omnipresent in outer space [234]; harder radiation penetrates the atmosphere. Larger molecular assemblies such as clusters, droplets, and even large molecules like proteins in their natural solvation environment are known to allow for additional relaxation pathways due to intermolecular interactions [29, 48, 146, 202, 235–240]. These pathways may lead to a protection of the molecule especially if the biomolecule is directly affected by the radiation [8]. On the other hand, secondary species originated from the ionization of surrounding solvent molecules can open up new pathways that lead to biomolecular destruction.

Hydrogen-bonded solute-solvent complexes allow for quantitative investigations of these effects [143, 149, 151, 241]. One of the important electronic relaxation channels of such dimers after x-ray ionization, electron-impact ionization, or α-particle irradiation was ascribed to intermolecular Coulombic decay (ICD) [143, 146–149, 241]. ICD results in the formation of mainly charge-separated di-cationic complexes which undergo fragmentation *via* Coulomb repulsion. A competing ultrafast relaxation channel of hydrogen-bonded complexes after inner-shell ionization, which may protect biomolecules, is intermolecular

---

[*] This chapter is based on the draft of the manuscript "*Molecular sunscreen: water protects pyrrole from radiation damage*" by Melby Johny, Constant A. Schouder, Ahmed Al-Refaie, Joss Wiese, Lanhai He, Henrik Stapelfeldt, Sebastian Trippel, and Jochen Küpper, *arXiv*:2010.00453. I contributed to the experiment, recorded the data, analyzed the data, discussed the results with some authors, and wrote the manuscript.

electron- or proton-transfer-mediated charge separation [48, 202, 241]. This was observed following x-ray ionization of the water dimer [151] and liquid water [150, 152].

A key ingredient for the indirect destruction pathways of biological matter is the radiolysis of water [37, 38, 232], which is probable because ∼3/4 of the volume of the cell comprises of aqueous environment [32, 232]. In this case, reactive cations, radicals, anions, or aqueous electrons are produced inside the water environment, which can trigger biomolecular fragmentation [31, 36–38, 43, 242]. In this context, it is still under discussion whether the hydration environment inhibits or enhances radiation-induced biological damage [40–46, 49, 232].

Pyrrole, a heterocyclic aromatic molecule, is a UV-absorbing chromophore, e. g., in hemes and chlorophylls [51]. Pyrrole is also a subunit of indole, 3-methylindole, and tryptophan, which are of great relevance as the principal UV-absorbers of proteins [52, 53]. The photophysical and photochemical properties of indole and pyrrole are sensitive to the hydration environment [25, 26, 54–56]: upon UV absorption these chromophores indirectly populate an excited $^1\pi\sigma^*$ state, which is repulsive along the N-H-stretching coordinate [52–54]. This triggers an ultrafast internal-conversion process to the ground state, essential for the photostability of proteins.

The pyrrole(H_2O) cluster has a well-defined structure with a hydrogen bond from the N-H site to the water [50]. This reflects the strongest interaction between pyrrole and surrounding H_2O in aqueous solution. H-elimination dynamics from the N-H site of pyrrole, mediated by the electronic excitation of the $^1\pi\sigma^*$ state [52, 218, 222, 223] or by vibrationally mediated photodissociation [243], was studied by time-resolved photoion and photoelectron spectroscopy. Theoretical calculations for electronically excited pyrrole(H_2O) clusters predicted electron transfer across the hydrogen bond without photodissociation of the pyrrole moiety [56, 219]. Direct ionization of pyrrole [244] and pyrrole(H_2O) [108] led to molecular fragmentation.

Here, we experimentally investigated the damage incurred in singly and doubly ionized pyrrole molecules and the effect of solvation by comparing the fragmentation pathways of bare pyrrole and microsolvated pyrrole(H_2O) heterodimers using pure samples of either species. This scheme enables the systematic investigation of the role of water solvation on the photophysics of pyrrole and hence for hydrated biomolecules in general.

A schematic representation of our ionization strategy is represented in Figure 5.1. We mimicked radiation damage through outer valence ionization. Pyrrole and pyrrole(H_2O) were site-specifically ionized, see Methods, through the removal of electrons from the HOMO or HOMO$-$1 orbitals, which are localized on the aromatic ring. This was achieved by strong-field ionization using 800 nm laser pulses with a peak intensity of $\sim 1 \times 10^{14}$ W/cm^2 and a pulse duration of 30 fs. Valence ionization of bare pyrrole resulted in extensive fragmentation. On the other hand, for singly ionized pyrrole(H_2O) we mainly observed breaking of the hydrogen bond and a water molecule leaving an intact pyrrole ring. In this case, breaking of the actual biomolecule is strongly suppressed.

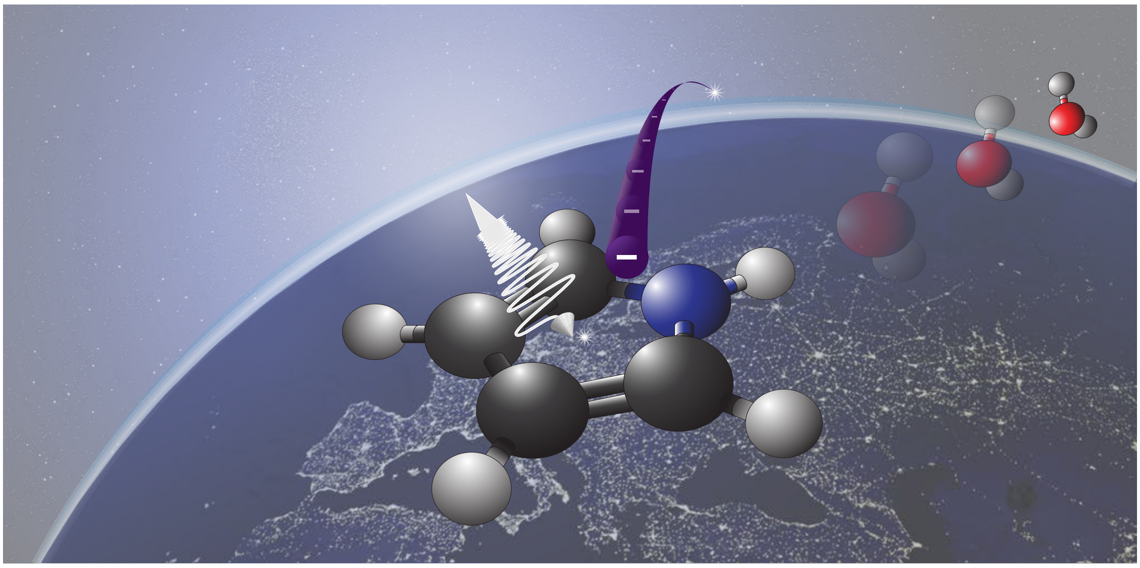

Figure 5.1. Schematic representation of the ionization scheme and radiation-protection mechanism in pyrrole(H_2O). Single ionization of the cluster is followed by its dissociation, with the leaving water molecule allowing the aromatic ring to stay intact without further fragmentation.

5.2 Results

Our comparison of the fragmentation dynamics of bare and microsolvated pyrrole built on the production of very pure molecular beams of pyrrole and pyrrole(H_2O), respectively; see Methods for details. The molecular beam had, in the case of pyrrole, a purity of ~95 %, with a contamination of ~5 % given by pyrrole dimer. The purity of the pyrrole(H_2O) beam was ~99 % with the major contamination by water dimer [110].

Figure 5.2 shows the time-of-flight mass spectrum (TOF-MS) and corresponding velocity-map images (VMIs) of all ions resulting from strong-field ionization of pyrrole. All data were recorded simultaneously using a Timepix3 camera [206, 207]. Rings in the VMIs occur for two-body Coulomb explosion, i. e., a charge-repulsion-driven fast breakup into two positively charged fragments. These fragmentation channels obey momentum conservation in the recoil frame. Low kinetic energy (KE) features correspond to charged intact parent ions or ions created from dissociative single ionization. The data shows no signatures of three-body breakup beyond hydrogen atom/proton loss.

The most prominent feature in the TOF-MS is the narrow peak at $m/q = 67$ u/e, assigned to pyrrole$^+$, on top of a broader pedestal. The peak corresponds to the sharp central dot in the corresponding VMI. The pedestal correlates with the rings in the VMI which are assigned to pyrrole$^+$ from Coulomb explosion of the pyrrole dimer. The TOF-MS peak at $m/q = 33.5$ u/e and the central dot in the corresponding VMI are assigned to the doubly ionized pyrrole. Its pedestal in the TOF-MS and the corresponding rings in the VMI are attributed to pyrrole^{2+} from Coulomb explosion of multiply-ionized pyrrole dimer. In both cases 95 % of the signal strengths are in the central peaks, i. e., originating from the

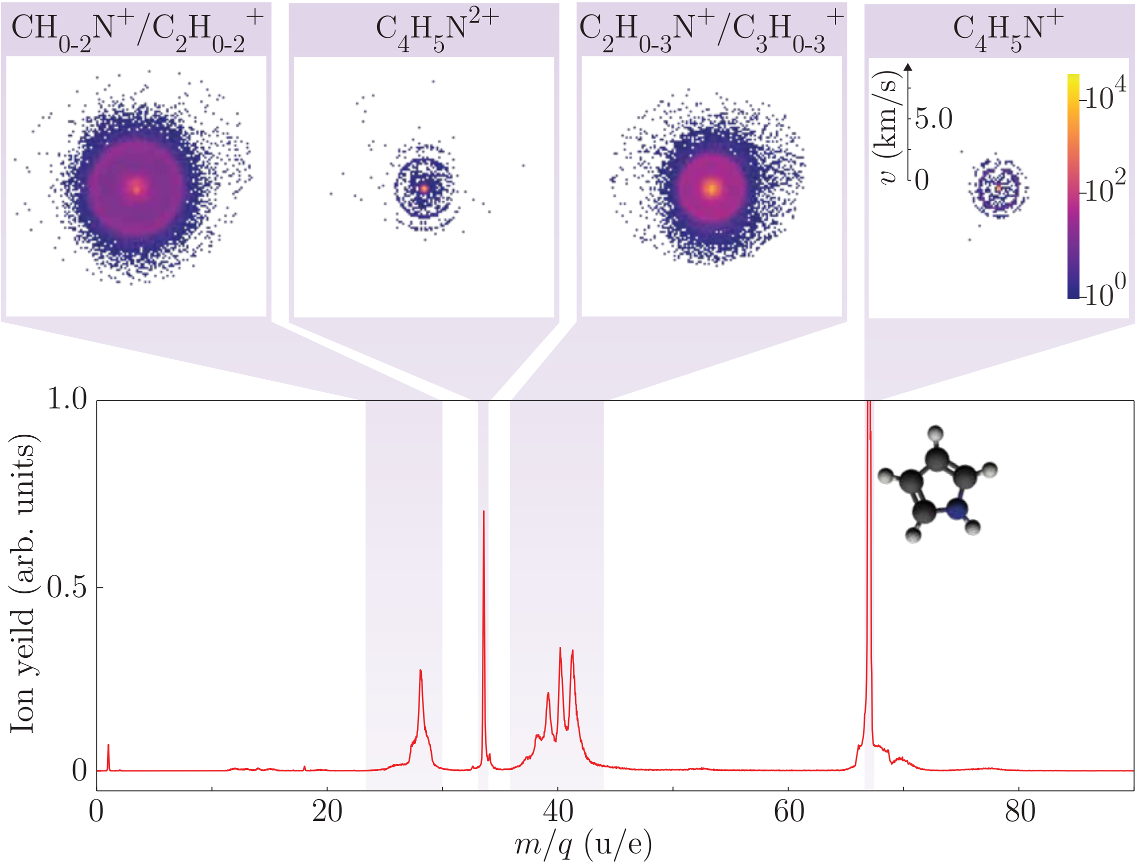

Figure 5.2. Time-of-flight mass spectrum and corresponding velocity-map images of the ions generated by strong-field ionization of pyrrole. The structure of pyrrole is given on the right of the lower panel. The colormap and velocity scale holds for all velocity map images.

monomer.

The signals in the mass-to-charge regions $m/q = 24\ldots30$ u/e and $m/q = 35\ldots44$ u/e correspond to fragments from the breakup of the pyrrole ring. Some possible ionic products are labeled in Figure 5.2, in line with the mass peak assignment after electron impact- and photoionization of pyrrole [244, 245]. A clear assignment of the various individual peaks observed in the two mass regions to specific fragments is not possible due to overlapping signals and ambiguities in the construction of specific mass to charge ratios out of possible feasible fragments. The situation is compounded by the fact that hydrogen loss off fragments was present. Proton loss after double ionization can be ruled out due to the lack of correlations between the detected protons and the fragments observed in the two mass regions. The small proton peak in the spectrum is therefore attributed to the initial charge states > 2. Intense central peaks in the VMIs correspond to fragments from dissociative ionization of singly charged pyrrole. The rings in these VMIs, contributing ∼30 % of the total ion count, correspond to fragments from Coulomb explosion of doubly charged pyrrole. The Coulomb explosion signals of the two mass regions are correlated, as confirmed by kinetic-energy selected coincidence maps and momentum conservation.

Figure 5.3 shows the TOF-MS and VMIs of all ions resulting from strong-field ionization

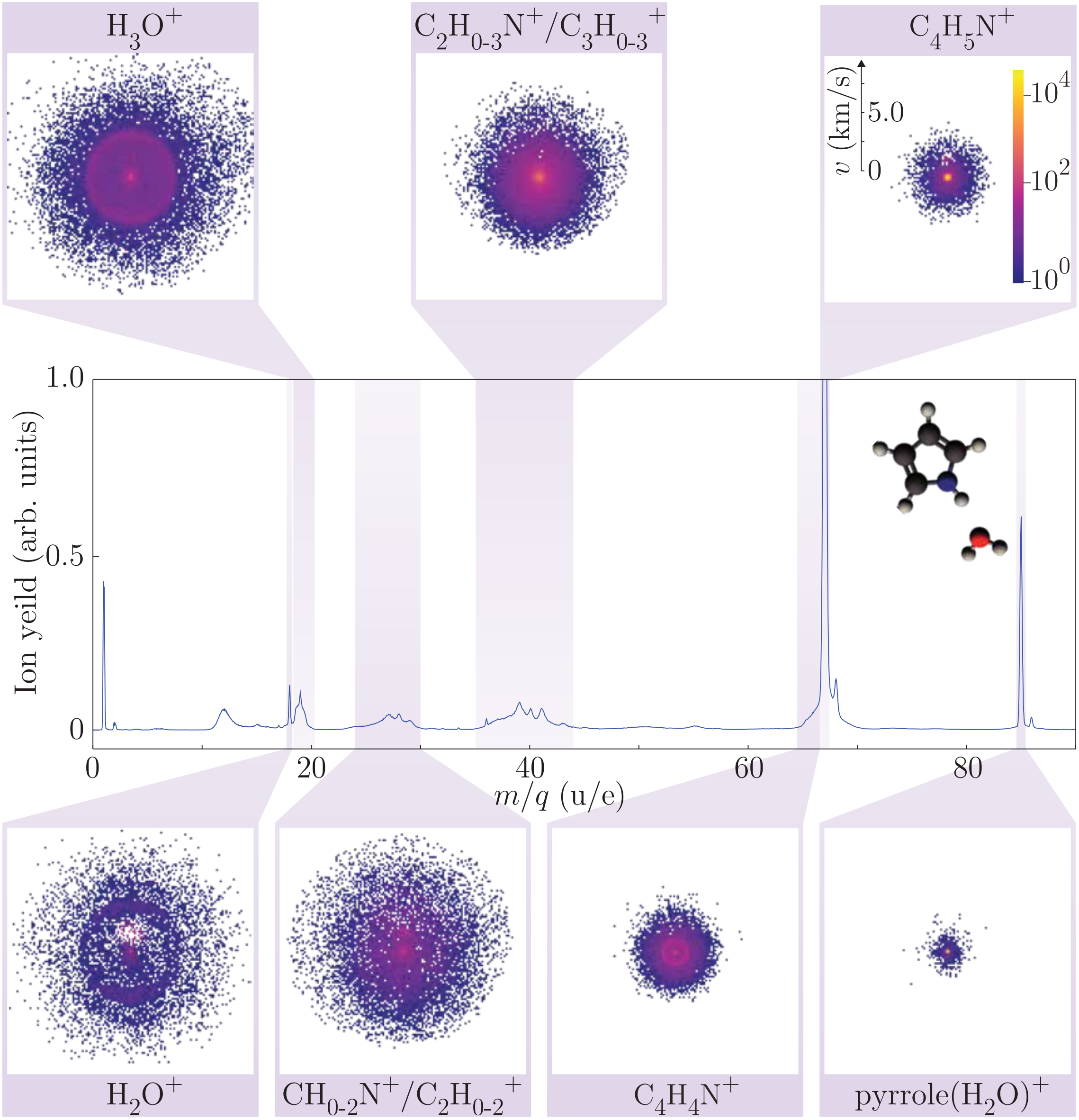

Figure 5.3. Time-of-flight mass spectrum of pyrrole(H_2O) with the velocity-map images of the ions, which were recorded simultaneously after strong-field ionization. Also shown are the structure of the dimer, sum formulas of all fragments, and the velocity ranges and colormap for all velocity-map images.

of purified pyrrole(H_2O). Again all data were recorded simultaneously using the time-stamping detector. All VMIs exhibit a central low-KE part due to single ionization as well as sharp or diffuse higher KE signals.

The peak at $m/q = 85$ u/e, with a central dot in the VMI, corresponds to the pyrrole(H_2O)$^+$ parent ion. The strongest peak in the TOF-MS is again at $m/q = 67$ u/e, the pyrrole-monomer cation, which resulted from the dissociation of the hydrogen bond in singly ionized pyrrole(H_2O). This is confirmed by its broader KE distribution in the VMI owing to recoil from the momentum conservation with the leaving neutral water molecule.

The peaks at $m/q = 66$ u/e and $m/q = 19$ u/e correspond to $C_4H_4N^+$ and H_3O^+, respectively. Both fragments exhibit sharp rings in their VMIs, with correlated ions that obey momentum conservation, demonstrating a two-body Coulomb explosion break-up channel of pyrrole(H_2O) including a proton transfer from pyrrole to water. A weaker H_2O^+ channel, ∼3/4 of which is correlated to pyrrole(H_2O) whereas the remaining signal can be attributed to the water dimer, shows the direct breakup of pyrrole$(H_2O)^{2+}$ across the hydrogen bond.

As for pyrrole, fragments within the regions $m/q = 24\ldots30$ u/e and $m/q = 35\ldots44$ u/e were detected due to the breakup of the aromatic ring. However, they show broad structureless distributions in the VMIs which are not correlated with each other. The high KE ions in these regions originate from pyrrole$(H_2O)^{2+}$ after three-body fragmentation processes. These channels always involve H_3O^+ as a second ionic partner, as well as a third neutral aromatic fragment. The small peak at $m/q = 36$ u/e is attributed to a singly ionized water dimer ($(H_2O)_2$).

5.3 Discussion

Overall, single and double valence ionization of pyrrole led to a significant breakup of the aromatic ring. Single ionization caused fragmentation of the pyrrole moiety through various dissociative pathways which resulted in low kinetic energy ions. Double ionization caused fragmentation of the aromatic ring driven by Coulomb explosion.

Surprisingly, the scenario is very different for pyrrole(H_2O). Despite of the localized ionization with the removal of electrons from pyrrole's same π orbitals, different relaxation pathways emerged through the hydrogen-bonded water molecule. For example, in the case of singly ionized pyrrole(H_2O), we observed the dissociation of the hydrogen bond, i. e., the loss of neutral water, which protected the pyrrole ring from fragmentation. Furthermore, after double ionization, additional Coulomb explosion channels appeared for pyrrole(H_2O), such as the H_3O^+ channel with its counter ion $C_4H_4N^+$. Both fragments showed sharp rings in the corresponding VMIs, thus leaving the pyrrole ring intact with only a proton lost. Additionally, two body Coulomb explosion channels of pyrrole(H_2O) in the regions $m/q = 24\ldots30$ u/e and $m/q = 35\ldots44$ u/e are absent and the uncorrelated signal is much weaker than the strong signals observed for the pyrrole monomer. In total, the fragmentation pathways were strongly influenced, i. e., pyrrole fragmentation was strongly reduced, by a single water molecule attached to pyrrole.

In order to unravel the influence of the microsolvation on the radiation induced damage and to quantify the degree of protection for ionized pyrrole in the presence of a single water molecule, we normalized the ion yields for the pyrrole and pyrrole(H_2O) species with respect to each other. We compared the laser intensity-dependent shape of the low-intensity single-ionization ion yield for both species as described in the Methods. Furthermore, the single, double, and higher-order ionization channels were separated to provide a direct comparison of the fragmentation yields for both species as a function of the initial charge

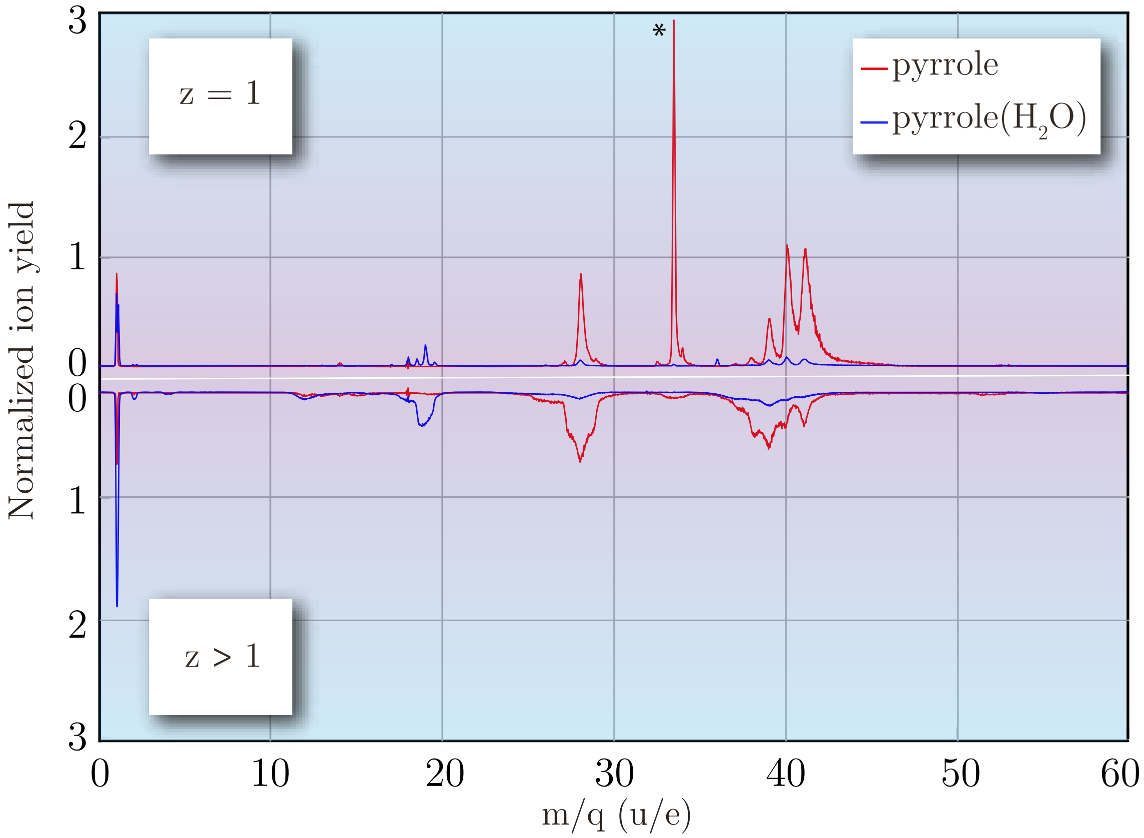

Figure 5.4. Comparison of the normalized TOF-MS of pyrrole (red) and pyrrole(H_2O) (blue). The number of charges created on the system after strong-field ionization is denoted by z. The upper panel corresponds to an initial charge state $z = +1$. The peak marked with the asterisk corresponds to intact $C_4H_5N^{2+}$ from double ionization of pyrrole. The lower section is for the charge states $z > +1$. Signals for $m/q = 2\ldots14$ u/e in the lower section originated from initial charge states with $z > +2$.

state. In addition, the fragmentation channels were classified into ring-fragmenting and ring-protecting channels.

The momentum maps for the specific mass-to-charge regions were taken into account in order to separate single, double, and higher-order ionization channels. Almost all VMIs shown in Figure 5.2 and Figure 5.3 had contributions from ions with low as well as with high kinetic energy. We attribute the low-KE ions to single ionization and the high-KE ions to double or higher-order ionization, respectively. Gating on the momenta with $p < 30$ u · km/s resulted in a normalized mass spectrum (NORMS) for single-ionization channels whereas gating on the momenta with $p > 30$ u · km/s resulted in a NORMS for the higher-ionization channels. The resulting normalized gated time-of-flight mass spectra for pyrrole and pyrrole(H_2O) are shown in Figure 5.4 for $m/q = 0\ldots60$ u/e, which contains all ring-breaking fragments. The upper panel corresponds to the single-ionization channels ($z = +1$), whereas the lower panel corresponds to double ($z = +2$) or higher ($z > +2$) ionization-channels.

Both species showed similar fragmentation products, especially in the mass-to-charge regions $m/q = 24 \ldots 30$ u/e and $m/q = 35 \ldots 44$ u/e, which are the channels arising from the breaking of the C–C and N–C covalent bonds of the pyrrole ring. However, they vastly differed in the specific ion yield and we observed a significant reduction of fragments arising from ring-opening in pyrrole(H_2O) as compared to pyrrole for both cases of single and multiple ionization. For both, pyrrole and pyrrole(H_2O), the contributions in the NORMS for $z \geq +2$ in the region $m/q = 15 \ldots 60$ u/e were dominated by double ionization. The contributions from triple ionization were statistically estimated to less than 5 % and are thus negligible, see Methods. Furthermore, the NORMS peaks in the region $m/q = 1 \ldots 14$ u/e originate from charge states with $z > +2$, confirmed by a covariance analysis. In the case of higher-order ionization, a direct comparison of the ion yield of pyrrole and pyrrole(H_2O) from the NORMS is not feasible due to the complex fragmentation processes and overlapping fragmentation channels.

To estimate the extent of fragmentation protection after single- and double ionization of pyrrole in a microsolvated environment the observed fragmentation channels were classified into ring-breakup and ring-protection channels. Based on this, the ring-fragmentation probability is defined as $P = \sum N_\text{b} / (\sum N_\text{b} + \sum N_\text{i})$ with the number of fragments where the ring is broken (intact) specified by N_b (N_i).

First, we considered ring-breakup and ring-protection channels following single ionization of pyrrole and pyrrole(H_2O). For pyrrole, the parent ion was considered as an intact channel. For single ionization of pyrrole(H_2O), in addition to the parent ion, the dominant ring-protection channel is the dissociation of the hydrogen bond, i. e., the loss of neutral water. Furthermore, the dissociative single ionization processes resulting in low KE ions of H_2O^+, H_3O^+, and $C_4H_4N^+$, prevent the aromatic ring from fragmentation. All other low KE ions in the mass-region $m/q = 15 \ldots 60$ u/e are considered as ionic products that originated from the fragmentation of the aromatic ring. The ring-fragmentation probabilities for pyrrole and pyrrole(H_2O) after single ionization were then determined by counting the ions in the momentum-map images with a cut on the low KE part in the specific mass-to-charge regions. The projection of ions from higher charge states ($z = +2$) into the center of the momentum-map images is estimated statistically, see Methods, and this contribution was subtracted. We estimated the ring-fragmentation probability individually for pyrrole and pyrrole(H_2O) to 48 % and 7 %, respectively, see also Figure 5.5. Overall, the ring-fragmentation probability of pyrrole following single ionization is reduced by a factor of ~7 in pyrrole(H_2O) compared to pyrrole.

We then classified the channels following double ionization of pyrrole and pyrrole(H_2O). For pyrrole, the only ring-protecting fragmentation channel was the formation of the doubly charged parent ion, $C_4H_5N^{2+}$, marked by the asterisks in the upper panel of Figure 5.4. All other channels broke up the aromatic ring. The dominant ring protection channel for the pyrrole$(H_2O)^{2+}$ was the intermolecular proton transfer from the N–H site of the pyrrole moiety to the water moiety, producing H_3O^+ and $C_4H_4N^+$. A second channel was the electron transfer process across the hydrogen bond, which leads to the formation

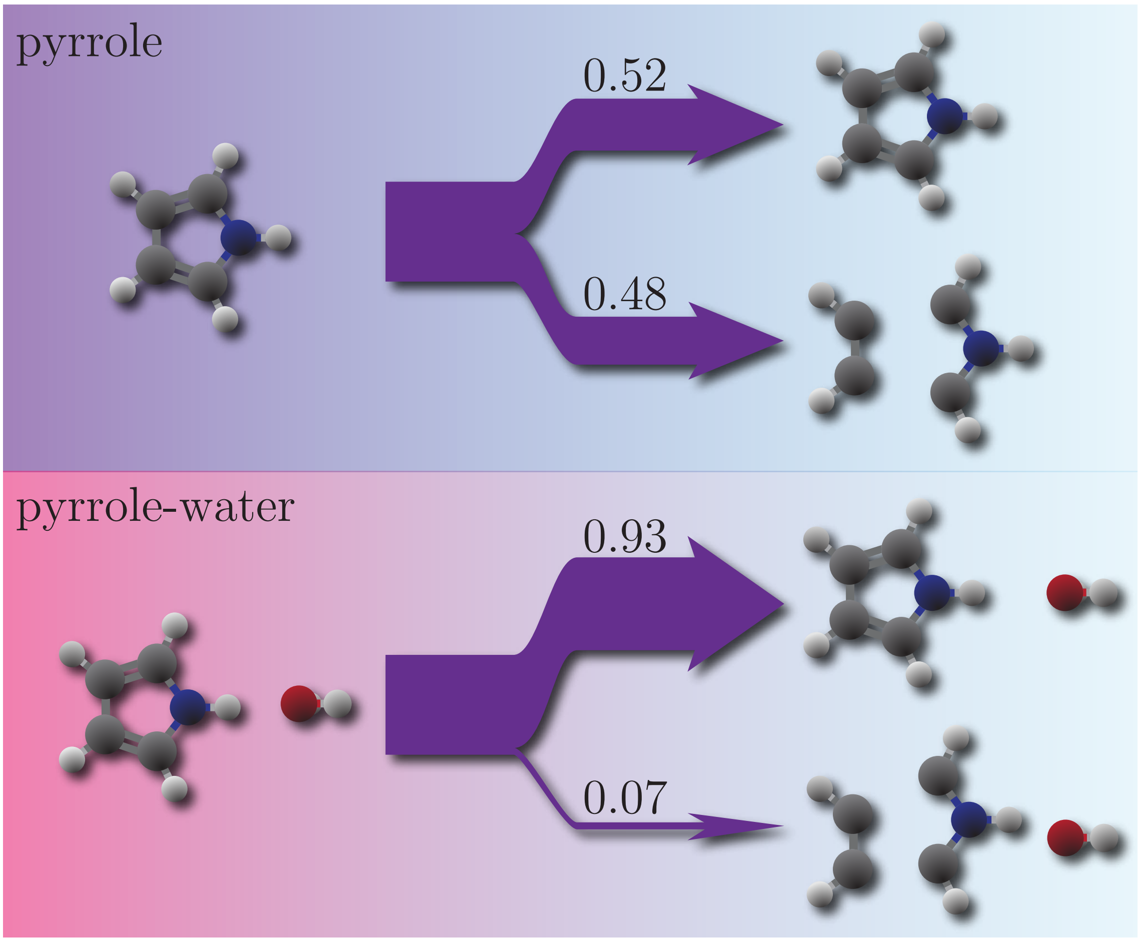

Figure 5.5. Schematic representation of the ring protection and breaking probabilities for pyrrole and pyrrole(H_2O) after single ionization, showing the very strongly reduced fragmentation probability of pyrrole in the cluster. For simplicity, only one of the observed fragments is shown for each channel. The width of the arrows (purple) and the numbers written above it represent the total ring-protection and breaking probabilities for pyrrole$^+$ and pyrrole(H_2O)$^+$.

of $C_4H_5N^+$ and H_2O^+. All other double ionization channels correspond to the breaking of the aromatic ring. The ring-fragmentation probability for pyrrole and pyrrole(H_2O) after double ionization were determined by counting ions in the high KE part of the momentum-map images while taking into account that two ions might have been produced after double ionization, leading to two hits in the corresponding momentum-maps for a single fragmentation event. The finite detection efficiency of 0.5 for each ion was taken into account. This led to a similar ring-fragmentation probability after double ionization for pyrrole(H_2O), $P = 0.80 \pm 0.04$, as for pyrrole, $P = 0.79 \pm 0.04$.

However, we observed a significant reduction in the total absolute ion yield of the microsolvated system for double ionization. This was indicated qualitatively through the comparison of the ion signals in the NORMS in Figure 5.4. To quantify this reduction we counted ions in the normalized momentum maps of the specific channels originating from double ionization of pyrrole and pyrrole(H_2O). The direct comparison revealed a reduction of the total ion yield of pyrrole(H_2O) by a factor of 2.6 ± 0.2. Thus, a single water molecule attached to the aromatic molecule pyrrole reduces its probability of being doubly ionized, with a subsequent high probability of ring breaking, 2.6-fold.

5.4 Conclusion

We demonstrated that a single water molecule strongly protected the pyrrole ring from fragmentation by ionization. For single ionization, microsolvation led to a strongly reduced fragmentation of the aromatic ring. Moreover, the solvation also significantly reduced the probability of double ionization and the corresponding probabilities for ring breaking. These quantitative studies were enabled by our ability to provide pure samples of the bare molecule and the microsolvated complex, as well as by using a novel time-stamping VMI detector.

Singly ionized pyrrole underwent radiation-induced damage through the breaking of, typically two, C–C or N–C bonds. Outstandingly, the dissociation mechanisms after single ionization of pyrrole(H_2O), through breaking of the intermolecular bond or by transferring an electron or proton across this hydrogen bond, strongly reduces the ring breaking probability by a remarkable factor of 7. After double ionization, similar ring-fragmentation probabilities were observed for pyrrole and pyrrole(H_2O). For the microsolvated system, intermolecular proton- and electron transfer processes occurring across the hydrogen bond increase the redistribution of charges, initially created in the pyrrole ring, to the water molecule. Nevertheless, we observed a reduction of 2.6 in the double-ionization probability for pyrrole(H_2O) compared to pyrrole, demonstrating a reduced double-ionization cross section and the corresponding protection of the microsolvated system.

Our experiments employed strong-field ionization for the ionization, typically removing electrons from the HOMO or HOMO-1 orbitals of pyrrole, which are also localized on the pyrrole moiety in the microsolvated systems. This mimics the ionization by neighboring molecules in aqueous systems, such as cells, as well as electronic excitation through UV radiation. Thus, our results provide a test case of how an aqueous microsolvation environment can strongly reduce the radiation damage of biological molecules induced by UV radiation as well as by secondary effects of ionizing radiation where single outer-valence ionization is the scenario. Furthermore, the doubly ionized systems in our experiment resemble to a large extent the fate of a molecule after Auger decay processes subsequent to core-shell ionization [146, 147].

Biomolecules and proteins in nature are actively solvated by the surrounding water molecules, which allow for efficient charge redistribution to the solvent environment through electron- and proton transfer pathways quantified here. In aqueous solution, the loss of the attached, neutral, ionized, or protonated, water could easily be repaired by the many solvent molecules around. Our analysis of the protection in pyrrole(H_2O) provides a quantitative analysis of radiation protection and serves as the basis for further investigations of the existing uncertainties [40–46, 49, 232] regarding the role of the solvent environment on the radiation damage of biomolecules.

5.5 Materials and Methods

5.5.1 Experimental Setup

Details of the experimental setup were described elsewhere [246]. A pulsed valve was operated at 100 Hz to supersonically expand a few millibars of pyrrole (Sigma Aldrich, >98 %) and traces of water in ~90 bar of helium into vacuum. The resulting molecular beam contained atomic helium, individual pyrrole and water molecules, and various aggregates thereof. The electric deflector was used to create pure samples of pyrrole(H_2O) [86, 108]. Pyrrole and pyrrole(H_2O) were strong-field ionized by 800 nm laser pulses with linear polarization, a duration of ~30 fs, focused to $\varnothing \approx 35$ µm (full width at half maximum intensity) with a peak intensity of $\sim 1 \times 10^{14}$ W/cm^2. The ions generated were extracted perpendicular to the molecular beam and laser propagation directions using a velocity-map-imaging spectrometer (VMIS). All ions were detected using a position- and time-sensitive detector consisting of a micro-channel plate (MCP) in combination with a fast phosphor screen (P46). A visible-light-sensitive Timepix3 detector [206, 247] in an event-driven mode recorded all signals, which were stored and centroided using our homebuilt pymepix software [207].

5.5.2 Normalization of the mass spectra

The normalization of the TOF-MS was necessary due to the different densities of the two species, pyrrole and pyrrole(H_2O), in the molecular beam. Due to the very similar first ionization energies (E_i) of pyrrole and pyrrole(H_2O) the ionization probabilities for both species are also very similar. The calculated (HF/MP2-aug-cc-pVTZ using GAMESS-US) first vertical E_i of pyrrole and pyrrole(H_2O) are 8.59 eV and 8.15 eV, respectively. To quantify the relative ionization probability experimentally [248, 249] the ion yield as a function of the laser peak intensity was measured for the single ionization channel for pyrrole, pyrrole(H_2O), and water, see Figure 5.6. Here, the ion yield from each pure species is normalized to its value for the highest laser intensity. In the low-intensity region, $1\text{–}8 \times 10^{13}$ W/cm^2, for pyrrole only the parent ion was observed. A saturation intensity for the parent ion signal of $\sim 6 \times 10^{13}$ W/cm^2 was obtained from the measured low-intensity ion-yield curve. For pyrrole(H_2O) we summed the signals for parent ion and pyrrole$^+$ [108], which yielded a saturation intensity for single ionization of $\sim 4.5 \times 10^{13}$ W/cm^2. Based on the similar saturation intensities and the very comparable intensity dependence of the ionization yields, Figure 5.6, we normalized the TOF-MS of pyrrole and pyrrole(H_2O) using a normalization factor of 1.94 ± 0.1.

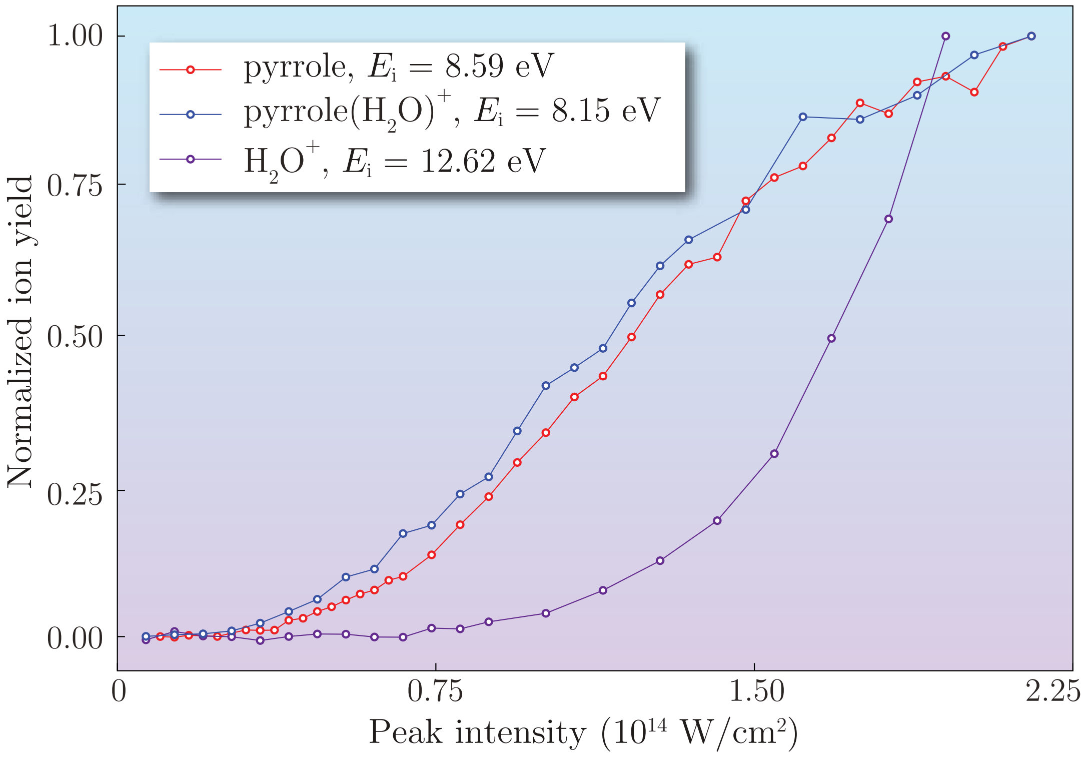

Figure 5.6. Single-ionization yields for pure samples of pyrrole (red), pyrrole(H_2O) (blue), and water (purple) measured at different laser peak intensities. All curves are normalized to their highest ion yield observed.

For the ionization of water, we obtained a very different intensity dependence and saturation intensity, which was determined as $\sim 1.4 \times 10^{14}$ W/cm^2. This is consistent with the larger E_i of 12.62 eV [250] and further demonstrates the similarities in the ionization cross sections of pyrrole and pyrrole(H_2O).

5.5.3 Highest occupied molecular orbitals of pyrrole(H_2O)

The molecular orbitals calculated (GAMESS-US, HF/MP2-aug-cc-pVTZ) for the geometry-optimized ground state structure of pyrrole(H_2O) are shown in Figure 5.7. The electron densities of HOMO to HOMO-3 are localized on the aromatic ring. The highest-energy bound molecular orbital with significant density on the water moiety is HOMO-4. This orbital has an energy that is 6.5 eV lower than the HOMO. Therefore, under the applied laser intensities ionization from this orbital can be neglected [194] and localized ionization of pyrrole(H_2O) at the pyrrole moiety can be safely assumed.

5.5.4 Triple-ionization contributions

To estimate the contributions of individual ions over a given mass-to-charge range from the measured 2D-projection of the 3D momenta, we made specific cuts in these experimental momentum maps in order to isolate contributions from single-, double-, and triple-ionization

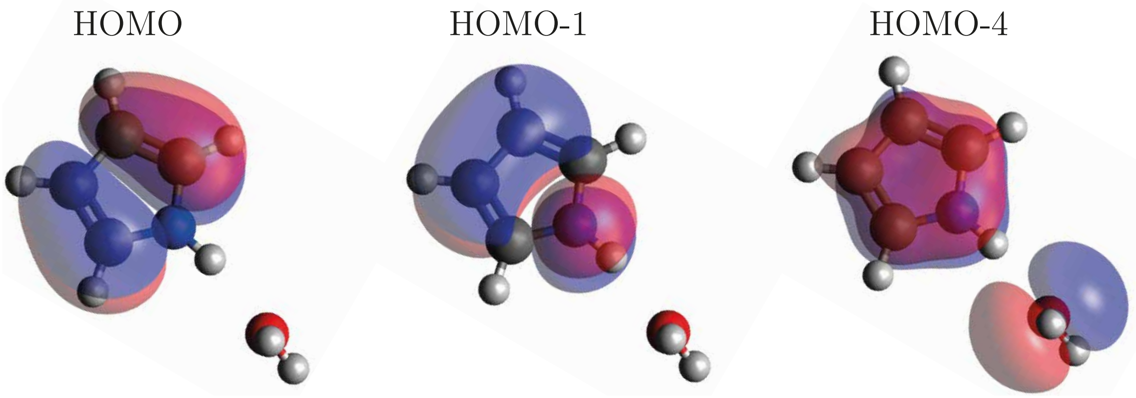

Figure 5.7. Molecular orbital picture of HOMO, HOMO-1, and HOMO-4 for the geometry optimized ground state structure of the pyrrole(H_2O).

radius p_r	ion counts in disk	ion counts in ring	area of disk/π	area of ring/π
60	167522	167522	3600	3600
140	225860	58338	19600	16000
200	229120	3260	40000	20400

Table 5.1: Total ion counts as well as the areas of disks and rings within specific radii chosen in the momenta map.

processes.

The measured momentum map for $m/q = 35 \ldots 45$ u/e is shown with Figure 5.8 as an example. Circles indicate corresponding cuts in the 2D-projection of the 3D-momentum sphere formed from each ionization process: The white circle with a radius of $p_r = 60$ u · km/s represents the edge of the momentum for dissociative single ionization, the green circle with $p_r = 140$ u · km/s corresponds to the maximum momentum of ions from Coulomb explosion following the double ionization, and the red circle with $p_r = \sqrt{2} * 140 \approx 200$ u · km/s is the maximum momentum of ions from triple ionization, assuming a two-body fragmentation into a singly-charged and a doubly-charged ion.

The total ion count corresponding to the disks defined by these specific radii and the signal in the two outer rings are provided in Table 5.1. Areas of the specific disks and rings are also given. Ion counts inside the outer ring, $140 < p_r < 200$, correspond to triple ionization without contribution from single and double ionization. However, the middle

charge state	ion counts	ion counts/area
+1 (single)	$167522 - 3.486 \cdot 3600 - 0.1598 \cdot 3600 = 154397$	$154397/3600 = 42.89$
+2 (double)	$58338 \cdot (19600/16000) - 0.1598 \cdot 19600 = 68332$	$68332/19600 = 3.486$
+3 (triple)	$3260 \cdot (40000/20400) = 6392$	$6392/40000 = 0.1598$

Table 5.2: Number of ion counts per area of each disk, and the estimated number of ions formed after the single, double, and triple ionization, respectively.

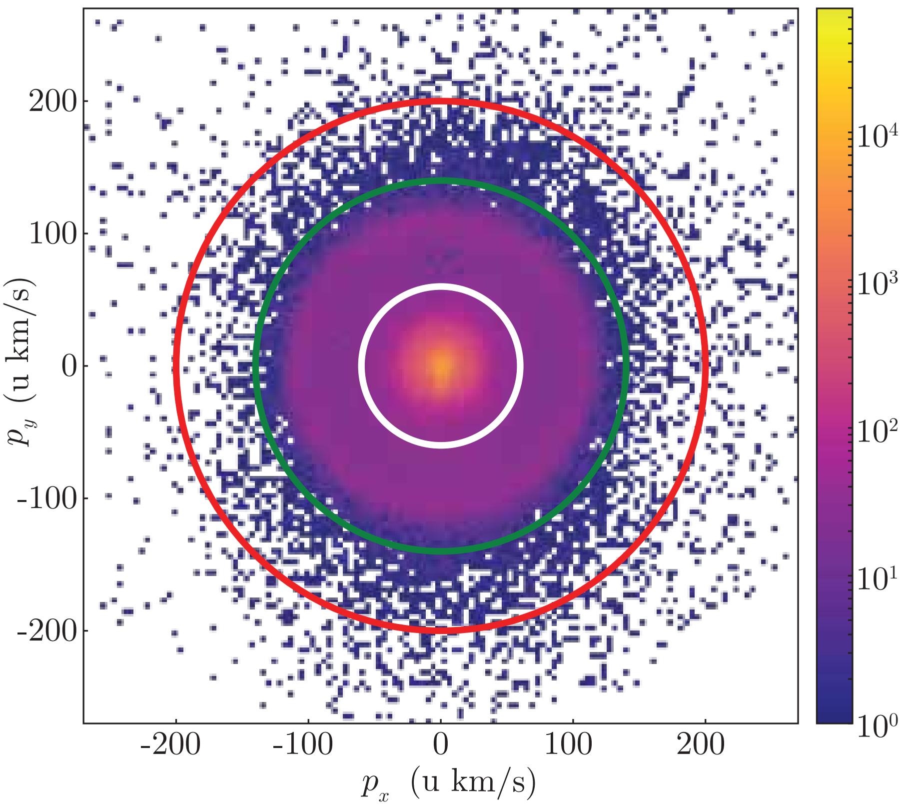

Figure 5.8. The momentum map for all ions detected within a mass-to-charge region $m/q = 35\ldots45$ u/e is shown. Marked circles with specific radii in the momenta map represent edges for single, double, and triple ionization, respectively.

ring, $60 < p_r < 140$, represents the double ionization channels and it has contributions from triple ionization; similarly, the innermost disk, $0 < p_r < 60$, representing single ionization has contributions from ions originating in double and triple ionization. The corrected total number of ions from single, double, and triple ionization are provided in Table 5.2 assuming a flat ion distribution in the inner part of the corresponding rings and disks. The relative contribution of the ion yield from the triple ionization process to the total ion yield in the given mass-to-charge region is < 5 %, i. e., negligible.

6 Enhanced strong-field ionization in pyrrole(H_2O) dimer [*]

6.1 Introduction

In the strong-field ionization regime, the field strength of the ionizing laser is comparable with the fields present inside a molecule or atom [188]. The mechanism for the ejection of the electron from the target depends on the intensity. At low intensities, it is mainly by multiphoton ionization, whereas within a range of intensities, tunnel ionization is dominating the process. The ionization occurs predominantly through the barrier suppression mechanism at really high intensities. Strong field ionization is the initial starting point for the high-harmonic generation [251, 252], which is crucial for attosecond sciences [253–257], as well as laser-induced electron diffraction experiments aimed to unravel the structure and dynamics of both electrons and nuclei [228, 258–261].

The ionization mechanism and corresponding rates for atoms in the tunneling regime are reasonably well known theoretically as well as experimentally [188, 262]. For molecules, the situation is, however, more complex due to the increased number of freedom induced by the various nuclei. In this context, it was demonstrated for diatomics that the ionization rate is strongly enhanced around critical internuclear distance, R_c, as compared to the equilibrium internuclear distance or in the dissociated limit. This phenomenon is known as charge resonance enhanced ionization (CREI), occurring around critical internuclear distance for electrons in the valence states [119, 120, 123, 263–270]. The mechanism for CREI depends on the specific system under investigation. One scenario for CREI in diatomic molecular ions is the existence of a pair of charged resonance states that are strongly coupled in the presence of laser field at stretched bond configurations [119, 120, 267]. Another reason is that the electron is partially trapped by the internal barrier of a double-well potential at a critical internuclear distance, R_c [123, 263]. Furthermore, an asymmetric charge localization in the potential well can also be responsible for this phenomenon [119, 120]. In all these scenarios, the localized electron experiences an enhanced field, which is the sum of the external laser field and the Coulomb field of the neighboring ion. This enables electrons to efficiently tunnel into continuum through the field-suppressed intra-molecular potential barrier [119, 120, 123, 267].

Enhanced ionization due to CREI (or variants of CREI) is responsible for the creation of highly-charged cationic states in triatomic molecules [271–274]. Recently, experimental and theoretical studies on strong-field ionization of small hydrocarbons revealed that the concerted stretch motions of multiple C-H bonds play a significant role in the enhanced

---

[*] This chapter is based on a draft of the manuscript "*Observation of an enhanced core-shell ionization in pyrrole(H_2O) dimer in the strong-field regime*" by Melby Johny, Constant A. Schouder, Ahmed Al-Refaie, Joss Wiese, Henrik Stapelfeldt, Sebastian Trippel, and Jochen Küpper. I contributed to the experiment, recorded the data, analyzed the data, discussed the results with some authors, and wrote the manuscript.

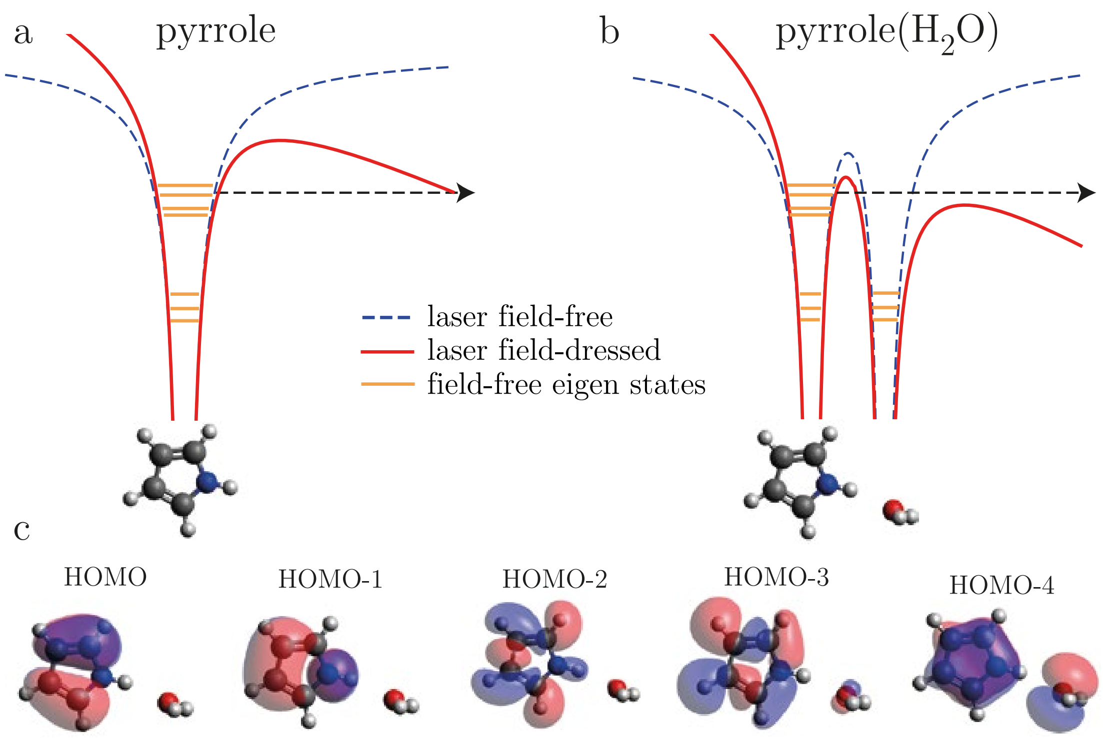

Figure 6.1. Schematic representation of Coulomb potential of a molecular ion of pyrrole (a) and pyrrole(H_2O) (b) in an intense laser field polarized along the internuclear axis (red curve). Field-free Coulomb potential (dashed blue curve) and eigenstates (orange lines) of both species are also represented. c) Molecular orbital picture of HOMO, HOM0-1, HOMO-2, HOMO-3, and HOMO-4.

ionization [122, 275–280].

In larger systems, i. e., larger van der Waals or hydrogen-bonded clusters, containing tens to hundreds of units, the interaction with an intense laser field leads to multiple electron ejection, and thereby, Coulomb explosion from highly-charged cationic species [117, 118, 124–127, 129, 130]. The proposed mechanisms for the creation of highly-charged atoms ejected from these clusters are explained either by the coherent electron motion model (CEMM) [117, 281] or the ionization ignition model (IIM) [117, 128, 129]. Interestingly, in these systems, complex ionization mechanisms resulting in inner-shell ionization are observed.

Here, we experimentally demonstrate enhanced inner-valence and inner-shell ionization observed in the heterodimer pyrrole(H_2O) after strong-field ionization. To unravel this novel observation for the dimer system, we performed the strong-field ionization on pure samples of our model systems, pyrrole monomer and pyrrole(H_2O). Pyrrole is a chromophore subunit of tryptophan, which is of great relevance as a principal UV-absorber of proteins [52, 53]. Our model system, pyrrole(H_2O), has a well-defined structure with the water attached to the N-H site of pyrrole [50] through a single hydrogen-bond. Figure 6.1 is a schematic representation of the Coulomb potential of a molecular ion of pyrrole (a) and pyrrole(H_2O) (b) with (red curve) and without (dashed blue curve) an intense laser field. The field-free eigenstates of pyrrole and pyrrole(H_2O) are also shown. The electron density is localized on the aromatic ring of pyrrole(H_2O) for HOMO until HOMO-3 (calculated using GAMESS-US, HF/MP2-aug-cc-pVTZ level of theory). The charge localization in the aromatic ring of pyrrole(H_2O) for the first four HOMOs facilitates an efficient pathway for electrons to tunnel out through the field suppressed intra-molecular potential barrier. Therefore, this can trigger an enhanced ionization rate for outer- and inner valence states of pyrrole(H_2O), which is not the case for pyrrole monomer. Hence, our studies propose pyrrole(H_2O) as a simple and well-defined model system to elucidate the mechanism of inner-shell ionization occurring in hydrogen-bonded molecular complexes in the strong-field regime.

6.2 Experimental details

The experimental setup used for the measurement was described elsewhere [246]. In brief, a pulsed molecular beam (repetition rate of 100 Hz) is generated using an Even-Lavie valve [73], *via* supersonic expansion of a few millibar of pyrrole (Sigma Aldrich, > 98 %) seeded in ∼90 bar of helium into a vacuum. Traces of water were added to the seed gas for the generation of pyrrole(H_2O). The electrostatic deflector [86] was used to spatially separate pyrrole as well as pyrrole(H_2O) from the rest of the molecular beam [108], which contained the seed gas atoms as well as other cluster species. Both pyrrole and pyrrole(H_2O) were strong field ionized using linearly polarized 800 nm laser pulses with a duration of ∼30 fs, focused to $\varnothing \approx 35$ µm (full width at half maximum in intensity) with a peak intensity of $\sim 1 \times 10^{14}$ W/cm^2. The ions generated were extracted perpendicular to both the molecular beam- and laser- propagation direction, using a velocity map imaging (VMI) spectrometer. All ions were detected using an assembly of a micro-channel plate (MCP) together with a fast phosphor screen (P46). A light-sensitive Timepix3 [206] camera, mounted outside vacuum facing the phosphor screen was used for the time- and position-sensitive detection of all ions. The Timepix3 camera was operated in an event-driven mode, and events were read out, stored, and centroided using a home-built python based library, Pymepix [207]. For the performed experiments, the estimated purity of pyrrole was ∼95 %, with a small contribution of ∼5 % of pyrrole dimer, while the purity of pyrrole(H_2O) was ∼99 %, with some remaining contributions from water dimer [110].

6.3 Results

The observation of enhanced ionization in microsolavted pyrrole(H_2O) in the strong-field regime is revealed by comparative fragmentation studies performed on pyrrole and pyrrole(H_2O). To investigate the complex fragmentation dynamics of these species after the strong-field ionization, we employed a covariance mapping technique [211–213]. The time-of-flight-mass-spectra (TOF-MS) information obtained with the Timepix3 camera was used to build up covariance maps of pyrrole and pyrrole(H_2O), as shown in Figure 6.2. Straight-line diagonal structures observed between ion pairs in the covariance map can be

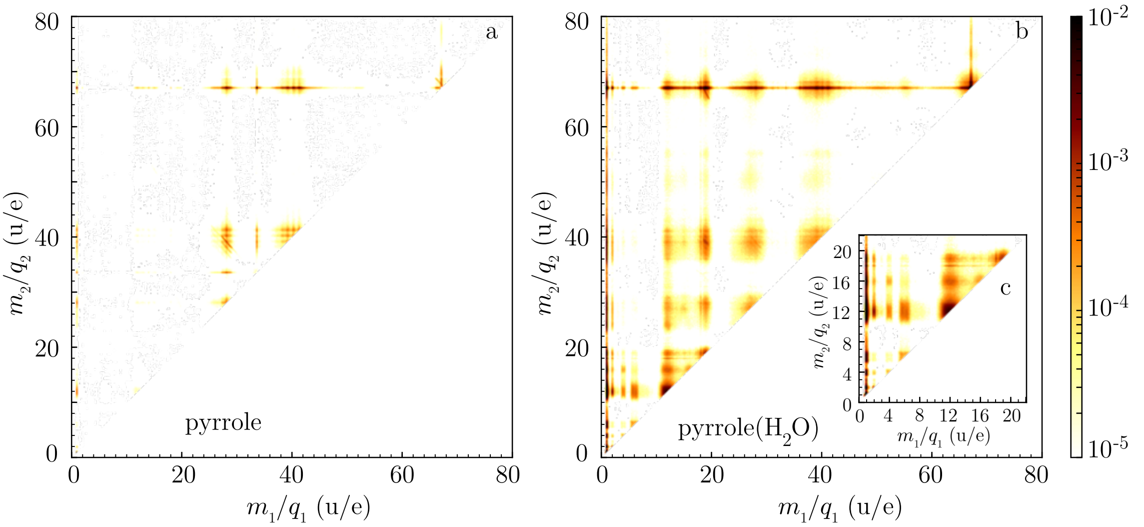

Figure 6.2. a) TOF-MS covariance map of pyrrole. b) Covariance map for pyrrole(H_2O). c) Zoom in to the mass-to-charge region $m/q = 0.5$–22 u/e of pyrrole(H_2O).

attributed to Coulomb explosion channels. These channels satisfy momentum conservation for perfect two-body break-up processes along with an axial recoil. For multi-body fragmentation processes as well as false coincidences, washed out correlation features are observed. Signal arising from single ionization-channels, which dominates the TOF-MS [282], are only present through false coincidences.

Figure 6.2 a shows the TOF-MS covariance map, which resulted from the fragmentation of pyrrole after strong-field ionization, unraveling the Coulomb explosion pathways of higher-order cationic states (z>1). The molecular mass of the pyrrole monomer is 67 u. The straight-line correlation between ion pairs, each with $m/q = 67$ u/e, is due to Coulomb explosion of the doubly ionized pyrrole dimers. Furthermore, Coulomb explosion of the $C_4H_5N^{2+}$ resulted in two singly-charged ionic fragments in our experiment, see the covariance island attributed to $m_1/q_1 = 24\ldots31$ u/e and $m_2/q_2 = 36\ldots43$ u/e. This island shows parallel correlation lines with a spacing of 1 u/e, which correspond to correlations for subsequent H loss channels. These are the only correlations observed in the case of pyrrole.

Figure 6.2 b shows the corresponding TOF-MS covariance map obtained from strong-field ionization of a pure beam of pyrrole(H_2O). Double ionization of pyrrole(H_2O) led to numerous fragmentation pathways with either two- or three-body breakup processes. Coulomb repulsion driven two-body breakup fragmentation channels of pyrrole$(H_2O)^{2+}$ are represented by straight-line correlations, see covariance island between $m_1/q_1 = 18$ u/e and $m_2/q_2 = 67$ u/e as well as between $m_1/q_1 = 19$ u/e and $m_2/q_2 = 66$ u/e. These channels are the electron- and proton- transfer pathways occurring across the hydrogen-bond in the pyrrole(H_2O) cluster [282]. Furthermore, fragmentation pathways for pyrrole$(H_2O)^{2+}$ were observed, where the cluster underwent a three-body breakup process generating two singly-charged ionic fragments and a neutral fragment. These channels result in washed-out correlation lines due to the neutral third fragment carrying a significant amount of the

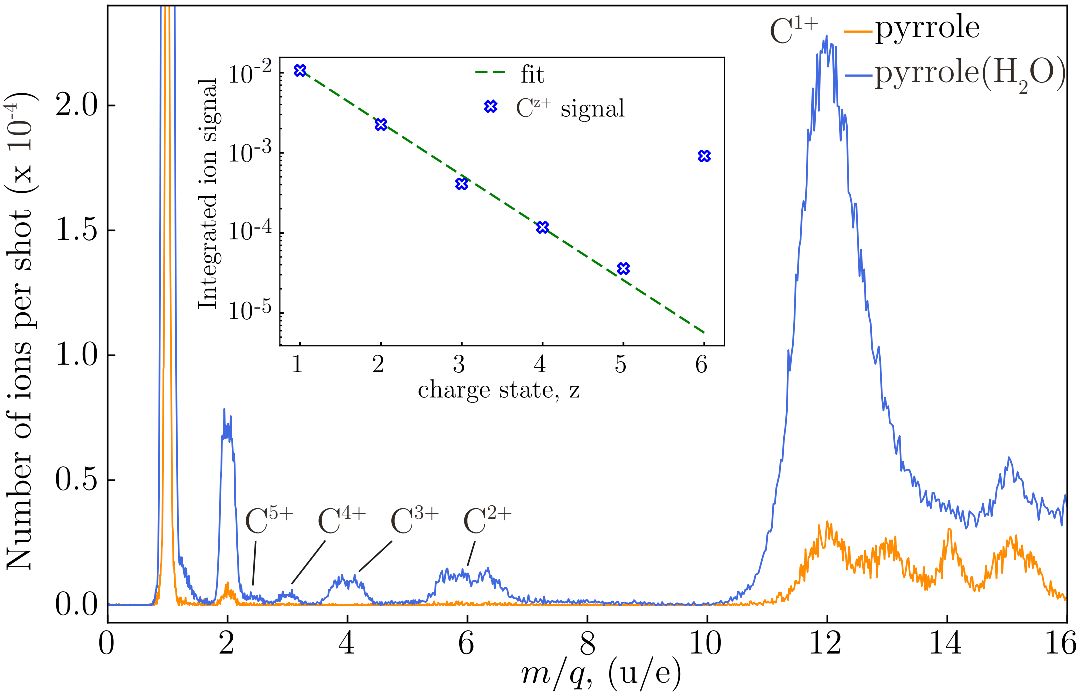

Figure 6.3. A comparison of the normalized TOF-MS of pyrrole and pyrrole(H_2O) for a mass-to-charge region $m/q = 0$–16 u/e. The m/q peaks in the TOF-MS is assigned for a specific charge state z of a carbon atom (C^{z+}). Inset: Ion yield for C^{z+} as a function of the charge state, z, together with an exponential fit.

total momentum. One example of such a process is the correlation of H_3O^+ with an ionic fragment of the aromatic ring. A second example for a three-body fragmentation channel of pyrrole$(H_2O)^{2+}$ is the formation of a neutral water molecule in combination with two singly-charged ionic fragments of the aromatic ring of pyrrole. The fragmentation dynamics for these channels are similar to the ring breaking channels in the case of $C_4H_5N^{2+}$, albeit the fact that the correlation lines are blurred out due to the leaving neutral water molecule.

An interesting feature observed in the fragmentation dynamics of pyrrole(H_2O) after strong-field ionization is the appearance of ionic fragments in the mass-to-charge region, $m/q = 0.5$–22 u/e, see Figure 6.2 c. Surprisingly, these ionic fragments were not observed or highly suppressed after strong-field ionization of the monomer. The region in the covariance map is dominated by C^+. Furthermore, washed-out correlations of C^+ with all ionic fragments of the aromatic ring; H^+, ${H_2}^+$, C^+, N^+, ${C_3H_3}^+$, CH_2N^+, $C_2H_3N^+$, and ${C_2H_2}^+$ were observed. Additionally, C^+ is also correlated with O^+, H_2O^+, and H_3O^+. Also, correlations of C^+ with highly-charged carbon ions C^{z+} ($z \leq 5$) were observed. The highly-charged carbon ions are also correlated with O^+, water$^+$, and H_3O^+.

A comparison of the normalized TOF-MS of pyrrole (orange graph) and pyrrole(H_2O) (blue graph) in the mass-to-charge region for highly-charged ions is shown in Figure 6.3; details concerning the normalization procedure can be found elsewhere [282]. The mass peak assignments and labels for the highly-charged ions are shown in the inset. A significant enhancement is observed for C^+ in the case of pyrrole(H_2O). Furthermore, a strong enhancement for the highly-charged C^{z+} ions with the value of positive charges up to $z = 5$ was measured. Also, an enhanced ion yield for H^+ and $m/q = 2$ u/e is observed, which can have contributions of either $H_2{}^+$ or C^{6+}. An unambiguous assignment of the individual contributions resulting in this mass peak is not possible due to the experimental resolution. In addition, it is interesting to note that only singly charged N^+ and O^+ are observed.

The integrated ion yield (in logarithmic scale) of highly-charged carbon ions, C^{z+}, obtained from the TOF-MS of pyrrole(H_2O) as a function of the charge z is shown in the inset of Figure 6.3. The mass peaks corresponding to C^{z+} with z = 2-4 are well-separated from each other, and the integral was determined by integrating over a single specific peak. For the peak corresponding to z=5, twice the integral over the non-overlapping right side of the mass peak from its center was taken into account. Similarly, for C^+, the left part of the peak was used to determine the integral. The integrated ion signal as a function of the charge state follows an exponential decrease up to z=5, as indicated by the green dashed line. The integrated ion yield for the TOF-MS peak of $m/q = 2$ u/e does not follow the fit function.

6.4 Discussion

We observed a strong enhancement in the yield for C^{z+} ($z = 1...5$), $m/q = 2$ u/e, and H^+ in pyrrole(H_2O) as compared to pyrrole, although the single- and double- ionization of the system protects it from fragmentation [282]. Surprisingly, a single water molecule attached to the pyrrole moiety results in an enhanced ion yield for highly-charged ionic fragments. Assigning a total initial charge state to the fragmentation channels arising from the strong-field ionization of pyrrole revealed that we create pyrrole^{z+} cationic states with charges $z < 3$. Similarly, for pyrrole(H_2O), the origin of covariance islands observed between regions $m_1/q_1 = 18 \ldots 67$ u/e and $m_2/q_2 = 18 \ldots 67$ u/e, are assigned to pyrrole(H_2O)$^{z+}$ states with charge $z < 3$.

Interestingly, in pyrrole(H_2O), we observed an enhanced ion yield for C^+. One of the possible pathways to generate C^+ is ascribed to Coulomb explosion after double- and triple- ionization of the pyrrole(H_2O). Furthermore, we measured core-shell ionized carbon species from Coulomb explosion of highly-charged pyrrole(H_2O), which was not the case for bare pyrrole. The appearance of C^{z+} ($z = 1...5$) in pyrrole(H_2O) is attributed to enhanced ionization in the strong-field regime, which resulted in Coulomb explosion from highly-charged pyrrole(H_2O)$^{z+}$ with a charge states up to $z = 6$ and higher. For example, counting the number of charges for a correlated fragmentation channel of C^{5+} against C^{5+} results in at least 10 charges initially created in pyrrole(H_2O). In that context, it would be highly desirable to determine the initial charge state for each specific fragmentation channel. However, this is not trivial due to the complexity of the system and the highly reduced efficiency for multi-body coincidence detection.

The efficient removal of outer-valence electrons in the heterodimer can be attributed to the fact that the first four HOMO orbitals of the cluster are localized on the pyrrole moiety. It enables enhanced tunneling rate from these states into continuum through the field-suppressed intra-molecular potential barrier in the presence of an external laser field and the Coulomb field of a neighboring ion, as shown in Figure 6.1. A combination non-adiabatic Landau-Zener type transistions and charge localization [119, 120, 267] can further suppress the internal barrier and facilitate the efficient removal of electrons from outer- and inner- valence states, which are bound by a few tens of eV in pyrrole(H_2O).

Outstandingly, for pyrrole(H_2O), we observed enhanced ionization, which results in the creation of core-shell ionized carbon atoms. To create the observed C^{5+}, it is required to remove an electron from C 1*s* orbital, which has an ionization energy of 392 eV [283]. This energy is 253 times the energy of a single 800 nm photon and therefore multiphoton ionization can be ruled out. Also, the electric field strength of $\sim 2.8 \times 10^8$ V/cm from the laser pulse is not large enough to distort the Coulomb potential of the pyrrole(H_2O) to remove core-shell electrons and transfer them into the continuum. Therefore, our observation hints towards the existence of a different ionization mechanism for the removal of electrons from the inner shell. To explain the observation of inner-shell vacancies in the strong-field regime, the possibility to ionize/excite inner-shell electrons by laser-induced electron re-collision remains elusive [131, 284, 285]. The attributed reasons are the low ponderomotive energy, i. e., 6 eV in our case, for the electrons at these laser fields as well as the reduced cross-section for such collisions [131]. Therefore, to explain the observed phenomenon, we adopt the inner-shell ionization mechanisms described in the case of very large hydrogen-bonded clusters or van der Waals clusters [117, 118, 130, 131]. In larger systems, the proposed mechanism is an electron-impact ionization caused by collisionally heated up hot electrons in clusters [117, 118, 128–130]. Again, the exact mechanism of inner-shell ionization is an open question and is still under investigation.

The integrated ion yield of the peak with $m/q = 2$ u/e does not follow the exponential decay observed for the charge states z=1-5. This observation can be explained by two-fold reasons. Firstly, the peak with $m/q = 2$ u/e can be ascribed to mixed contributions of H_2^+ or C^{6+}. Due to the presence of the water in the cluster, an enhancement for the H_2^+ might be possible, as observed for fragmentation processes in the case of alcohols after strong-field ionization [286]. Secondly, it is also possible that the signal is higher for this mass peak because it is not possible to further remove electrons from a carbon atom, which is completely stripped.

6.5 Conclusion and Outlook

In summary, we experimentally show that enhanced inner-shell ionization happens in the strong-field regime even for a small heterodimer, pyrrole(H_2O). The systematic investigation on a pure sample of pyrrole and pyrrole(H_2O) showed that highly charged cationic states are only observed for pyrrole(H_2O), but not in pyrrole monomer. Enhanced inner-valence ionization in pyrrole(H_2O) is triggered by charge localization in the pyrrole moiety of the cluster. The observation of enhanced ionization in pyrrole(H_2O) is surprising because, upon single and double ionization of the pyrrole(H_2O), the aromatic ring is significantly protected as compared to monomer [282]. Outstandingly, the observation of enhanced core-shell ionization in the strong-field regime for a small molecular system is for the first time. Our experimental results outlook the relevance of field-induced internal barrier suppression for molecular clusters in the strong-field regime and the necessities for the extensive theoretical framework that can explain core-shell ionization phenomena observed in molecular complexes. Furthermore, our studies outlook towards the implementation of a cluster beam as a source of highly-charged carbon ions, which have higher biological effectiveness in cancer therapy [287].

To elucidate the mechanism behind enhanced ionization of pyrrole(H_2O), one has to perform coincidence detection of the electrons and ions originating from highly charged cationic species. Another crucial requirement is the alignment and orientation of the molecular complex [115, 288]. This will have two-fold benefits. The first benefit is from the previously observed fact that the molecular alignment has a dramatic effect on the total ionization rate from enhanced ionization due to the geometric overlap of the molecular orbitals with the polarization axis of the ionizing laser [267, 275, 276, 280, 289, 290]. The second aspect is that this would help to identify the angular dependence of the ions or electrons ejected from the enhanced ionization process owing to the different geometric overlap of the molecular orbitals. In such a floppy cluster, the alignment would help to confine the direction of the ions from the Coulomb explosion process and as well as extract critical intermolecular distance Rc, at which enhanced outer-valence ionization occurs *via* simple approximations as used already for linear molecules [122, 266, 275]. Also, it is crucial to study the influence of polarization as well as the carrier-envelope phase of the ionizing laser field on the rate of enhanced ionization process. Strong-field ionization of the pyrrole(H_2O) cluster also has to be investigated for a range of laser intensities, to accommodate for the focal-volume averaging effects [249], as well as to determine the onset intensity for different cationic states to be created.

One of the challenges to unravel the inner-shell ionization mechanism in larger clusters is the complexity of these systems and the difficulties to perform experiments on controlled size-selected clusters. Also, the minimum number of cluster units required to have an enhanced core-shell ionization in the strong-field regime was unknown [117, 118, 128–130]. The systematic study performed on bare pyrrole and a hydrogen-bonded heterodimer, pyrrole(H_2O), revealed that enhanced core-shell ionization can happen even in a small dimer system. Our study demonstrates pyrrole(H_2O) as a simple model system, where extensive experiments and theoretical strategies can be implemented in the future, to shed light on underlying mechanisms for core-shell ionization in the strong-field regime.

7 Site-specific soft x-ray ionization of pyrrole and pyrrole-water

7.1 Introduction

Biological matter undergoes radiation-induced damage upon interaction with ionizing radiation like x-rays, γ rays, $\alpha-$, or fast-charged particles [31–33]. After the inner-shell ionization of the biomolecule, a vacancy is created in the core-shell, followed by subsequent radiative and non-radiative relaxation pathways. Numerous electronic relaxation dynamics are expected to occur after core-shell ionization of molecules, including charge-transfer and charge-migration processes, ultimately resulting in the fragmentation dynamics. In addition to the primary radiation damage caused by ionizing radiation, there exist the damage mechanisms created by secondary effects [32]. Recent studies show that one of the efficient mechanisms for radiation damage processes of biomolecules is *via* auto-ionization caused by low-energy secondary electrons [32, 34]. The interatomic coulombic decay (so-called ICD) process [146, 147] is one of the crucial electronic relaxation channels for molecules after inner-shell ionization, resulting in the formation of two-separate-charged sites and low-energy electrons. These slow electrons have the potential to cause radiation damage in biomolecules [32, 34]. Therefore, it is necessary to extensively investigate various relaxation dynamics observed in molecules, after core-shell ionization.

Here, the x-ray irradiation-induced fragmentation dynamics of a prototypical biomolecule, pyrrole is elucidated. The heterocyclic aromatic molecule pyrrole is a UV-absorbing chromophore found in hemes and chlorophylls [51, 52]. Pyrrole is also a subunit of indole, the chromophore of amino acid tryptophan. The electronic structure of pyrrole and indole has similarity to that of adenine, DNA base, as well as these chromophores are known to play an essential role in the photo-stability of biological matter [52, 53]. In order to unravel possible relaxation mechanisms after core-shell ionization of model chromophores, ionization induced by x-rays is utilized. Previously, the complex fragmentation pathways of indole after site-specific inner-shell ionization at the N-H site of the molecule was investigated by measuring Recoil-Frame Photo Angular Distributions (RFPAD) [162]. Such a study revealed fragmentation-pathway-dependent electron spectra, correlating the structural fragmentation dynamics to different electronic excitations. To get deeper insights performing such studies on pyrrole, indole's subunit will be of crucial importance.

As a next step, it is of great significance to elucidate the role of the solvent environment in the relaxation pathways of biomolecules after core-shell ionization. The influence of the hydration environment on the radiation-induced biological damage is not well understood so far, in terms of whether it results in further damage or protection to the biological matter [40–46, 49, 232]. For instance, we have observed reduction as well as an enhancement for the radiation damage in biomolecule in the vicinity of a single water molecule, after outer-valence ionization, as mentioned in previous chapters 5 and 6. Within this context of radiation-induced molecular damage, the observation of intermolecular coulombic decay (ICD) [147] has been demonstrated as a relaxation mechanism after inner-shell ionization of small molecular clusters, hydrogen-bonded water dimer [143], larger water clusters [148], or even in microsolvated tetrahydrofuran [149]. Additional ultrafast relaxation channels observed after core-shell ionization of hydrogen-bonded clusters are the electron- and proton-transfer mediated charge separation processes [150, 202]. These were observed in water dimer [151], liquid water [152], as well as in microsolvated indole-water [221] clusters.

The photophysical and photochemical properties of UV-absorbing chromophores, pyrrole and indole are fairly sensitive to the hydration environment [26], or even with a single water molecule attached to the molecule [25]. The microsolvated pyrrole(H_2O) cluster has a well-defined structure, with the water attached to the N-H site of pyrrole [219] through a hydrogen-bond. Site-specific x-ray ionization performed at N 1*s*, i. e., the local site of the cluster could potentially probe the inter-molecular relaxation mechanism occurring across the hydrogen bond. Hence, we consider pyrrole and pyrrole(H_2O) as a model system for the systematic investigation of solvation effects on the photophysics of core-shell ionized biomolecules.

A prior criterion to achieve, before studying the influence of solvents is to fully understand and characterize the photophysics of pyrrole monomer owing to x-ray irradiation. Therefore, we performed detailed investigations of the photophysics of pyrrole after site-specific core-shell ionization at the nitrogen atom. These studies promise to unravel the relaxation processes like interatomic coulombic decay (ICD) [147], as well as the radiation damage mechanisms of biological systems. Our experimental approaches to unravel the photophysics of pyrrole(H_2O), after site-specific ionization at the N-H site of the cluster, are also covered. With this, we aim to elucidate relaxation processes in these hydrogen-bonded systems like intermolecular coulombic decay (ICD) [147], electron-transfer mediated decay (ETMD) [202], proton-transfer mediated charge separation (PTMCS) [48], and radiation-induced damage/protection mechanisms in solvated biomolecules, in general.

7.2 Experimental Details

A schematic representation of the experimental setup used for the measurement is shown in Figure 7.1. In brief, an Even-Lavie valve [73] was used for the generation of a pulsed molecular beam *via* supersonic expansion of a few millibars of pyrrole (Sigma Aldrich, > 98 %), and traces of water seeded in ~90 bar of helium into a vacuum. The valve was operated with a repetition rate of 250 Hz and was heated to a temperature of 65 °C. The expanded molecular beam resulted in an ensemble of particles, including atomic seeding gas, monomers, and the molecular clusters. An inhomogeneous electric the field created inside an electrostatic deflector was used to disperse the molecular beam according to the species' effective-dipole-moment-to-mass ratio [86, 214, 226]. The test experiments demonstrating

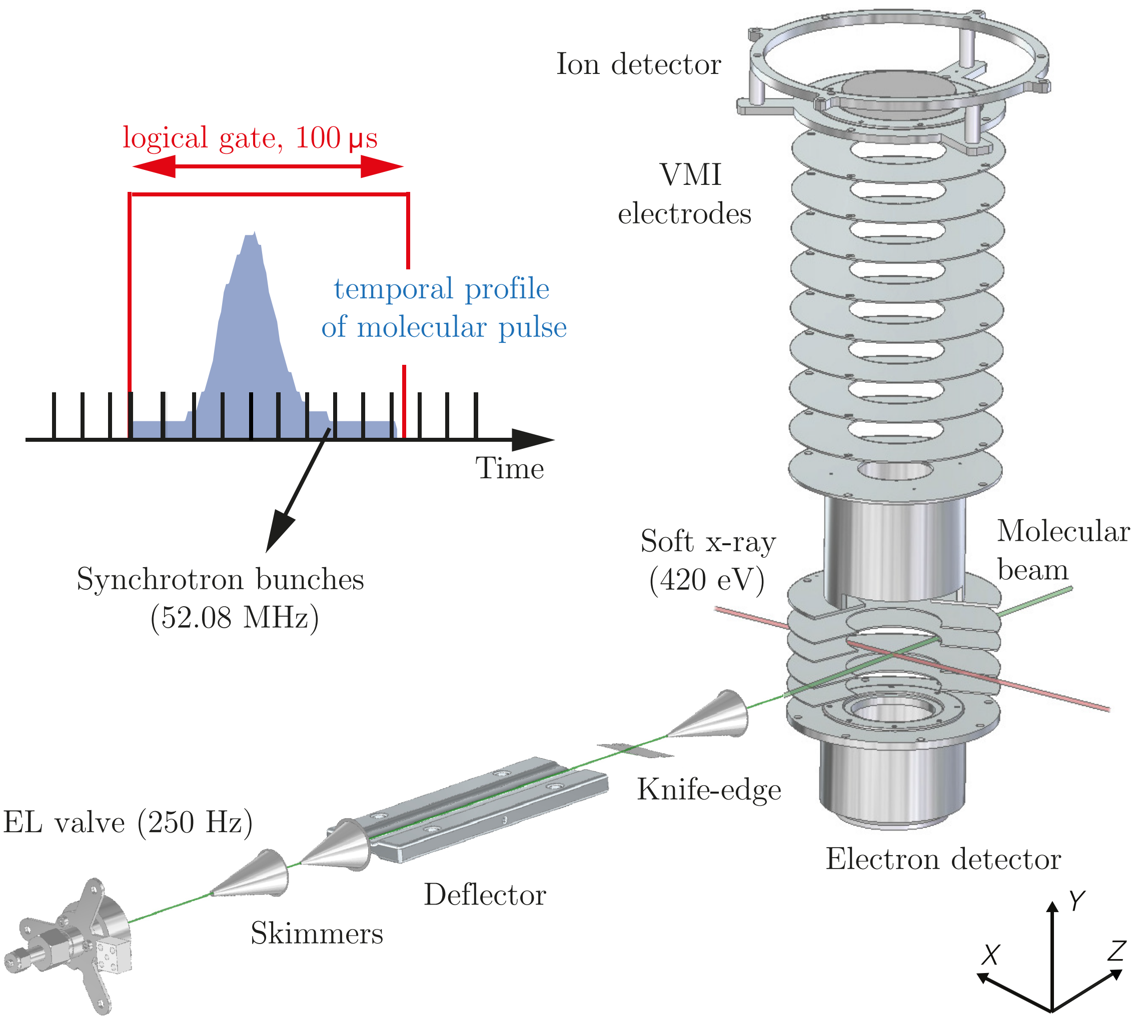

Figure 7.1. Schematic representation of the experimental setup: comprising of the pulsed EL valve, skimmers, deflector, knife-edge, and the double-sided velocity map imaging spectrometer (VMIS). The synchrotron beam, tuned to a photon energy of 420 eV, interacts with the molecular beam in the center of the VMIS. A schematics demonstrating the logical gate (red) used to synchronize the temporal profile of the molecular beam with x-rays in the interaction region is shown in the top-left corner. The black vertical bars represent multiple synchrotron pulses crossing the molecular beam.

the spatial separation of pyrrole(H_2O) was performed in our lab using an optical laser. The spatial separation of the singly-hydrogen bonded pyrrole(H_2O) cluster with ~100 % purity was already demonstrated [108]. Also, a high purity sample of pyrrole(H_2O) was achieved for experiments performed in chapters 5 and 6. Therefore, this level of purity is expected to achieve during the beamtime using our molecular beam setup [108, 224], provided the fact that the supersonic beam expansion and cooling conditions are stable.

Site-specific x-ray ionization of samples was performed using the synchrotron facility at Petra III, Variable Polarization Beamline P04 [291]. We aimed at using Photoelectron-Photoion-Photoion Coincidences (PEPIPICO) imaging technique for the detection of the ions and electrons created by x-ray ionization of pyrrole and pyrrole(H_2O). Our molecular beam setup was mounted to the CAMP−CFEL−ASG Multi Purpose−end station [292], which was then attached to the beam-line. The propagation direction of the x-rays was perpendicular to the propagation axis of the molecular beam. For the experiment, the synchrotron was operated at the time-resolved mode (also called timing-mode), which means we used 40 bunches with a bunch period of 192 ns. The synchrotron was tuned to a photon energy of 420 eV ($\lambda = 2.95$ nm) i. e., above N 1*s* edge and was linearly polarized ($>$ 98 %).

The electrons and ions generated after x-ray ionization were extracted perpendicular to the molecular beam propagation direction using a double-sided velocity map imaging (VMI) spectrometer [293]. The ions and electrons were detected using a time- and position-sensitive delay line detector (DLD, Roentek). A hex-anode (HEX80) and quad-anode DLD (DLD80) were implemented for the electron and ion side, respectively. The first detected electron signal on the electron side of the spectrometer was used to trigger the electronic readout of the ion detectors. All of the detected electrons and ions during a set acquisition window of 6 μs were treated as originated from one ionization event, which was then tagged with a time-stamp and sorted using the COBOLD software from Roentek.

The molecular beam has a pulse duration of $\sim$35 μs (FWHM, full width at half maximum), resulting in a duty cycle of $\sim$3.5 %. Our molecular beam was operated at 250 Hz, while the synchrotron was operated at a repetition rate of 52.08 MHz. To reduce the amount of background signal created by the high repetition rate of the synchrotron, we record data only in a specific time window. For this purpose, we used a logical gate of 100 μs duration, which was synchronized to the arrival time of the molecular beam in the interaction zone, as shown in Figure 7.1. More details of the detection scheme can be found in this publication [162].

7.3 Ionization cross-sections

The calculated total x-ray absorption cross-sections for each element species present in pyrrole and pyrrole(H_2O) are shown in Figure 7.2. The absorption cross-section for atomic hydrogen is negligible as compared to other elements (factor of $\sim$3000 lower), and hence it is not plotted. The energy for 1*s* ionization potential scales in the following order, C 1*s* $<$ N 1*s* $<$ O 1*s*. We have chosen photon energy of 420 eV for our studies, which is $\sim$10 eV above the ionization potential of N 1*s*. This is done to avoid direct ionization at the O 1*s*, i. e., ionization on the water site of the hydrogen-bonded pyrrole(H_2O) cluster. However, there exists a significant absorption cross-section for C 1*s* ionization at a photon energy of 420 eV. In the aromatic ring of pyrrole and pyrrole(H_2O), we have 4 carbon atoms, 1 nitrogen atoms, and 5 hydrogen atoms. For a photon energy of 420 eV, the atomic absorption cross-section for nitrogen is 0.6466×10^{-22} m^2, while for the carbon it is 0.4327×10^{-22} m^2. Hence, the probability to perform localized ionization at N 1*s* in pyrrole and pyrrole(H_2O) is only $\sim$20 %. This is obtained after making the following assumptions. The first one is that the x-ray absorption cross-section for each element in the molecule is similar to that

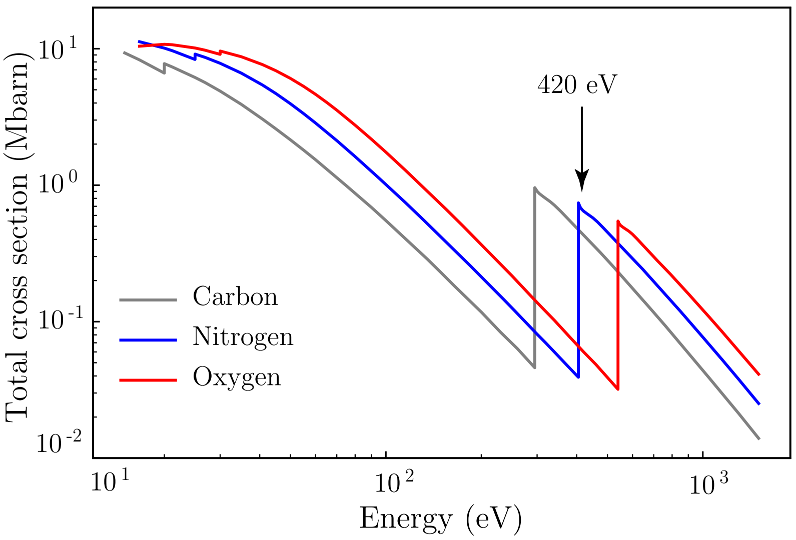

Figure 7.2. The calculated total absorption cross-section for individual atoms present in pyrrole(H_2O) is plotted for a range of photon energies. The marked vertical arrow represents the photon energy used for ionization of both pyrrole and pyrrole(H_2O). The data is taken from reference [198].

of individual atomic-like species. Secondly, the contributions from the absorption of the inner-valence and valence orbitals are not considered, as it is in the few percent levels.

7.4 Coincidence spectra of pyrrole monomer

The fragmentation mechanism of pyrrole after inner-shell ionization is studied using Photoion-Photoion Coincidence spectra. To create a fairly pure sample for pyrrole, we have not added traces of water to the seed gas. In addition to this, the contributions from the seed gas and homo-clusters of pyrrole (pyrrole$_n$, n>1) were reduced through deflecting the molecular beam by applying 14 kV voltage across the electrodes of the deflector, see Figure 4.4. The PIPICO spectrum built among the ions created from pyrrole following inner-shell ionization is shown in Figure 7.3. The structure of the pyrrole monomer is depicted in the inset of the figure. The PIPICO spectrum is depicted in the units of the mass-to-charge ratio, m/q (u/e). In general, the sharp straight lines observed in a coincidence island of the PIPICO map gives information about the fragmentation channels, where the molecules break-up into two ionic fragments with an axial recoil. The washed-out PIPICO islands give a hint towards the ionic fragments formed from a fragmentation process, where more than two fragments are created. For a perfect two-body break-up channel, the slope of the line observed within a PIPICO island is given by $-\sqrt{q_1 m_2 / q_2 m_1}$ [162, 210]. If the charge and the mass of both of the ionic fragments are identical, then the slope is -1.

The fragmentation channels originated from the Coulomb explosion of the cationic states of pyrrole are represented by the labeled PIPICO islands in Figure 7.3. The coincidence islands along $m_2/q_2 = 67$ u/e (black dashed rectangle) are either due to false coincidences

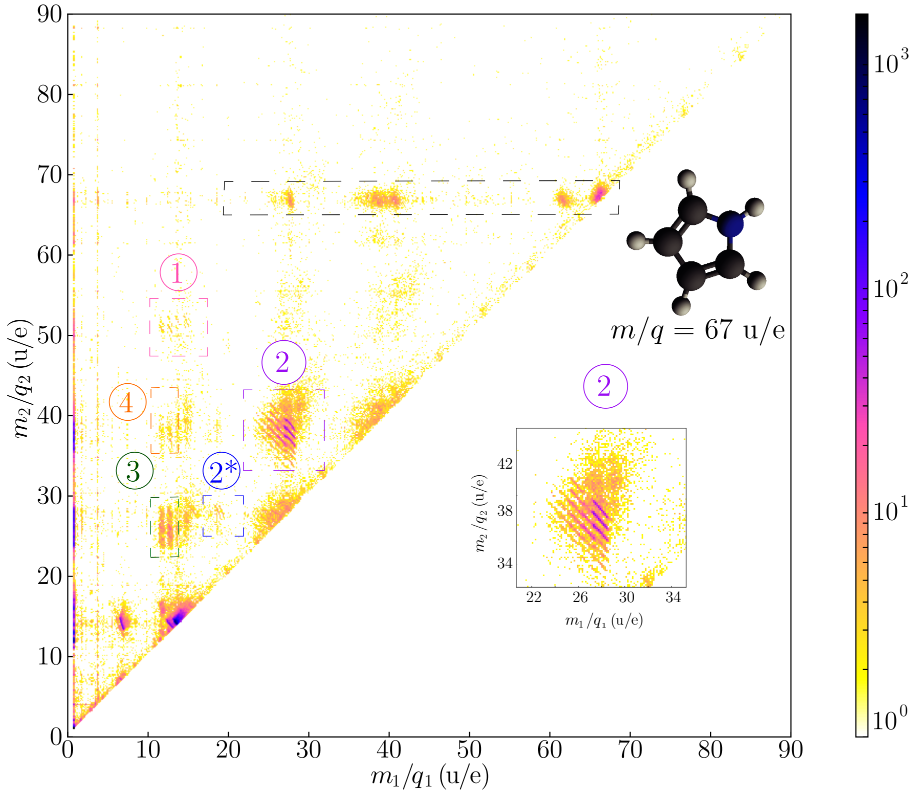

Figure 7.3. The Photoion-Photoion Coincidence spectrum after x-ray ionization of pyrrole at 420 eV. The structure of the molecule together with the molecular mass is shown in the inset. The regions outlined in boxes together with labels highlight relevant islands in the PIPCO map.

or the coincidences arising from the fragmentation of larger pyrrole clusters present in the deflected part of the molecular beam. The real coincidence islands from the fragmentation of cationic states of pyrrole are the following islands: 1, 2, 2*, 3, and 4. The coincidence island 1 (marked in pink) corresponds to the correlation between NH^+ ($m_1/q_1 = 15$ u/e) and $C_4H_4^+$ ($m_2/q_2 = 52$ u/e). The parallel lines in the PIPICO island separated by $m/q = 1$ u/e are due to the subsequent proton or H-losses. The PIPICO island 2 (marked in purple) belongs to two fragmentation channels. The first fragmentation channel is the Coulomb repulsion of $C_3H_3{}^+$ ($m_1/q_1 = 39$ u/e) and CH_2N^+ ($m_2/q_2 = 28$ u/e). The second channel is the formation of $C_2H_3N^+$ ($m_1/q_1 = 41$ u/e) and $C_2H_2{}^+$ ($m_2/q_2 = 26$ u/e). Both of these channels show additional PIPICO lines for the subsequent proton or H losses. The PIPICO island 2* (marked in blue) shows coincidence between $m_1/q_1 = 19.5$ u/e and $m_2/q_2 = 28$ u/e, and slope of the coincidence line is < -1. The washed-out PIPICO island 3 (marked in green) and island 4 (marked in orange) correspond to the coincidences of C^+, N^+ together with heavier fragments such as CH_2N^+, $C_2H_2{}^+$, $C_2H_3N^+$, and $C_3H_3{}^+$. The PIPICO islands 3 and 4 are possibly coincidences resulted from multi-body fragmentation processes involving other ionic or neutral fragments. The straight-line coincidence island between $m_1/q_1 = 14$ u/e and $m_2/q_2 = 14$ u/e is due to the Coulomb explosion of the dicationic state of N_2 present in the background. In addition to that, the coincidence line between $m_1/q_1 = 7$ u/e and $m_2/q_2 = 14$ u/e originated from the tri-cationic state of N_2.

Here, we assign few coincidence islands to the charge state of the parent ion from which they underwent Coulomb repulsion. The PIPICO islands 1 and 2 show very sharp PIPICO lines and are originated from an axial recoil fragmentation process involving two ionic fragments. Both of these ionic fragments within the coincidence island are singly charged, and the sum of the mass of these two fragments adds up to the mass of the parent molecule, pyrrole monomer. Hence, these fragmentation channels originated from the Coulomb explosion of $C_4H_5N^{2+}$. The correlated ion pairs created from $C_4H_5N^{2+}$ are shown below, and the numbers written in brackets represent the labeled fragmentation pathways of the PIPCO map, see Figure 7.3.

$$C_4H_5N^{2+} \longrightarrow C_4H_4{}^{+} + NH^{+}(1) \tag{7.1}$$

$$C_4H_5N^{2+} \longrightarrow C_3H_3{}^{+} + CH_2N^{+}(2) \tag{7.2}$$

$$C_4H_5N^{2+} \longrightarrow C_2H_3N^{+} + C_2H_2{}^{+}(2) \tag{7.3}$$

The PIPICO island 2* is formed from two-body break-up process of $C_4H_5N^{3+}$. The two ionic products resulted from the Coulomb explosion of $C_4H_5N^{3+}$ are $C_3H_3{}^{2+}$ ($m_1/q_1 = 19.5$ u/e) and CH_2N^{+} ($m_2/q_2 = 28$ u/e). Each of the above-mentioned fragmentation channels satisfies the conservation of the momentum in the recoil-frame for a perfect two-body break-up process. All of these fragmentation channels arise from breaking of the C−C, and N−C covalent bond in the pyrrole after the formation of $C_4H_5N^{2+}$ and $C_4H_5N^{3+}$ cationic states. The dicationic state has possibly resulted from the relaxation processes like Auger decay processes after core-shell ionization. The tri-cationic state formation can be explained by the shake-off processes accompanying the Auger decay [200].

The fragmentation channels for the created di- and tri-cationic states of pyrrole owing to core-shell ionization looks very similar to that was measured after strong-field ionization, as shown in chapters 5 and 6. In both cases, the observed PIPICO islands, as well as relative intensities between the Coulomb explosion pathways for the above-mentioned cationic states, are also similar. However, we have not seen any shreds of evidence for the formation of intact $C_4H_5N^{2+}$ and $C_4H_5N^{3+}$ states after x-ray ionization, unlike the scenario after outer-valence ionization as described in the chapter 5. This can be explained with the following argument: after x-ray ionization and subsequent relaxation processes, vacancies are created over a broad spectrum of dissociative inner- and outer-valence states. In comparison to the previous fragmentation pathways measured for the case of indole after site-specific x-ray ionization, we see a resemblance to the observation of mainly two-body break-up channels from di- and tri-cationic states [162].

To further investigate the site-specificity in the fragmentation pathway, fragment-channel dependent electron spectra, as well as details of charge-localization processes, one needs to look at the electrons that are formed from these cationic states. Based on the kinetic energy of the electrons, one could distinguish between different relaxation mechanisms, whether it is pure Auger decay or due to processes such as ICD and shake-off channels. Due to technical issues during the beamtime, the full potential of the delay line anode for the electron side was not exploited. Hence, the kinetic energy of electrons could not be extracted this time. However, measuring electrons and ions in coincidence is planned for future experiments, which could give detailed insights into site-specific fragmentation pathways.

7.5 Conclusion

In summary, we have investigated the fragmentation processes through coincidence imaging of the ions generated following inner-shell ionization of a fairly pure sample of pyrrole. We have observed the formation of $C_4H_5N^{2+}$ and $C_4H_5N^{3+}$, after the relaxation of the core-shell ionized molecule, pyrrole. The $C_4H_5N^{2+}$ and $C_4H_5N^{3+}$ states underwent heavy fragmentation of the aromatic ring through the breaking of C-C or N-C covalent bonds. We have also identified the individual fragmentation channels for these cationic states. Our studies revealed that the Coulomb explosion channels of $C_4H_5N^{2+}$ and $C_4H_5N^{3+}$ states formed after x-ray core-shell ionization is very similar in comparison with the observed fragmentation channels of di- and tri-cationic states of pyrrole created after strong-field ionization. A detailed fragmentation study on pyrrole provides a basis for the systematic investigation of radiation-induced damage in biological matter. Furthermore, performing a comparative site-specific x-ray ionization study on microsolvated pyrrole(H_2O) can pave the way to find the role of solvents on the photophysics of biomolecules after core-shell ionization.

7.6 Outlook: Toward the photofragmentation studies of pyrrole(H_2O)

To investigate the influence of a single water molecule on the fragmentation dynamics after site-specific x-ray ionization of pyrrole, we have attempted to perform the same fragmentation studies on pyrrole(H_2O). The following section discusses the preliminary experiments we have performed to investigate on the site-specific x-ray photophysics of pyrrole(H_2O). A combined insight from x-ray photophysics studies on bare pyrrole and pyrrole(H_2O) sets a baseline for the time-resolved photophysics studies on these model systems planned in the future. The systematic study of how the fragmentation dynamics of the core-shell ionized pyrrole evolves as a function of the increasing distance of the water molecule away from the pyrrole moiety can have implications on revealing the dynamic nature of the solvent environment. An overview of the envisaged time-resolved experiments

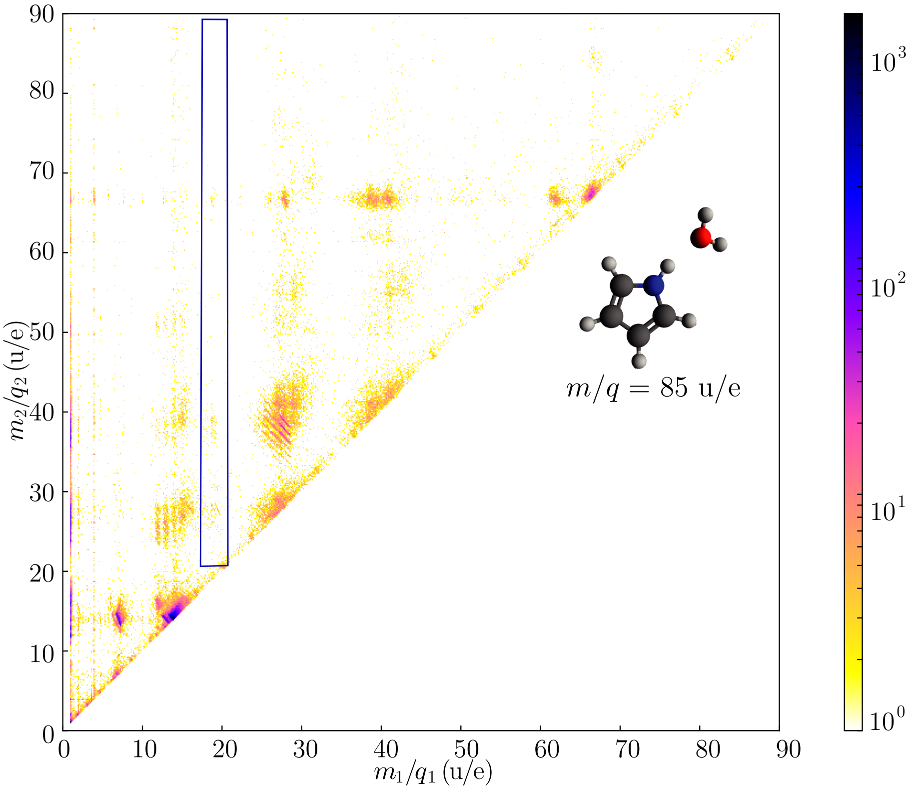

Figure 7.4. The Photoion-Photoion Coincidence spectrum measured at the deflected part of the molecular beam, where the pyrrole(H_2O) cluster is expected to be present. The structure of the pyrrole(H_2O) is also shown in the figure. The marked blue rectangle shows the coincidence regions, where significant differences between pyrrole and pyrrole(H_2O) are anticipated.

are also described in this section.

7.6.1 Photophysics after x-ray ionization of pyrrole(H_2O)

After the site-specific x-ray ionization measurements for bare pyrrole, as shown in section 7.4, we have performed the same experiment on pyrrole(H_2O) to unravel the role of solvent environment in the photophysics of ionized pyrrole. One of the key requirements for such a systematic photophysics investigation is the preparation of a pure sample of pyrrole(H_2O). Therefore, we have added the traces of water to the seed gas using a conventional bubbler. As demonstrated in the previous chapters 3 to 6, an electrostatic deflector is used to spatially disperse different species in the molecular beam expansion. The pyrrole(H_2O) cluster is expected to be present in the most deflected part of the molecular beam [108, 224]. Hence, we have adjusted the vertical position of the entire molecular beam, using motorized stages inside the vacuum, relative to the x-ray beam.

The measured PIPICO spectrum after x-ray ionization at 420 eV shown in Figure 7.4. The used photon energy ensures ionization occurs at the pyrrole ring of the cluster. We expect the fragmentation products from the pyrrole ring of the cluster to be similar to that of the pyrrole monomer. The observed PIPICO islands look very similar to the measured PIPICO

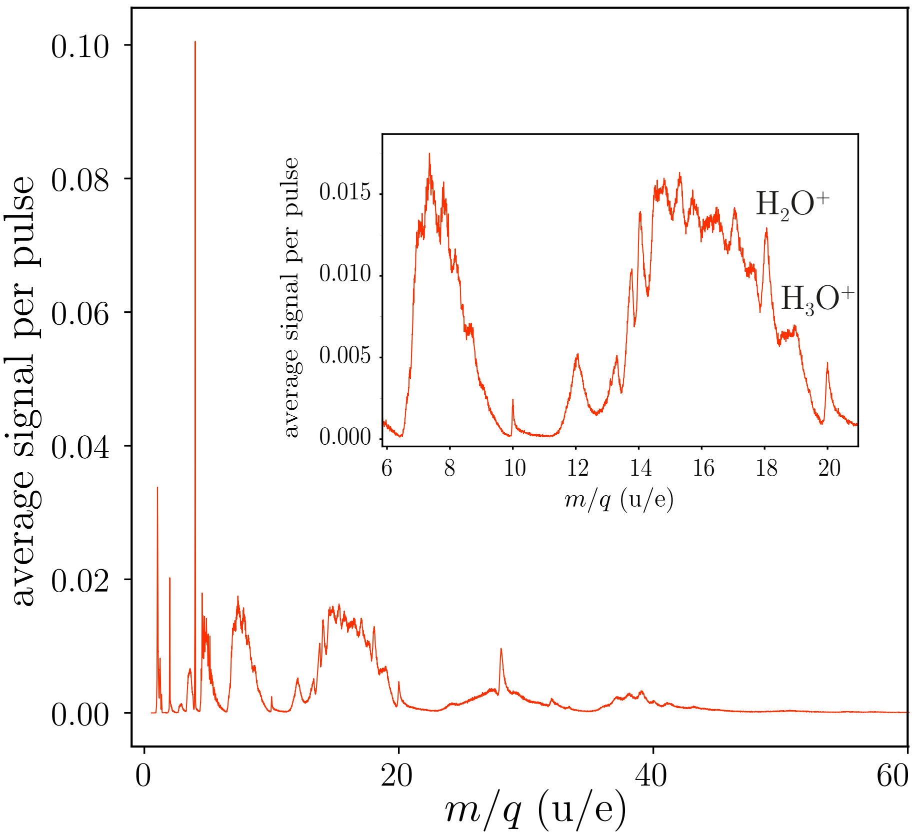

Figure 7.5. The time-of-flight-mass-spectrum measured after site-specific (above N 1s edge) x-ray ionization of a pure sample of pyrrole(H_2O). The inset shows a zoomed in to the mass-to-charge region $m/q = 0 \ldots 20$ u/e, highlighting the H_2O^+ and H_3O^+.

of monomer Figure 7.3, except the fact that the contributions from the larger clusters are reduced. This is expected for a measurement performed in the most deflected part of the beam because larger-clusters exhibit lower values for effective-dipole-moment-to-mass ratio [108] and are less deflected. In addition to this, the expected prominent features after x-ray ionization of pyrrole(H_2O) are the electron- and proton- transfer channels across the hydrogen-bond, i. e., H_2O^+, and H_3O^+, respectively as signatures for ionic products. This was the main difference observed in a similar previous experiment performed for indole [162] and indole(H_2O) [221]. However, in our PIPICO, we have not observed signatures for the formation of H_2O^+ ($m_1/q_1 = 18$ u/e) and H_3O^+ ($m_1/q_1 = 19$ u/e), see marked blue rectangle region shown in Figure 7.4.

Based on the absence of signatures of fragmentation products from pyrrole(H_2O), we suspect that we did not have pyrrole(H_2O) in the interaction zone. Such a scenario can happen if the supersonic beam is not cold enough for cluster formation and cluster selection. Typically, in the lab, i. e., like the experiments performed in previous chapters 3 to 6, we could look at the parent ion signal to see whether pyrrole(H_2O) is present in our molecular beam. This approach is not possible with x-ray ionization because after core-shell ionization of pyrrole(H_2O) parent ions are not expected to be measured as the cluster undergoes fragmentation owing to subsequent relaxation processes. The absence of an optical laser in the beamline also inhibited us from checking the constituents of the molecular beam during the measurement time. Unfortunately, due to time constraints during the beamtime, our quick attempts to find the signatures of pyrrole(H_2O) were not successful.

Recent follow-up beamtime performed at EuXFEL confirms our suspicion that we did not have pyrrole(H_2O): we there clearly observed the electron- and proton-transfer channels across the hydrogen-bond in pyrrole(H_2O) for ionization above N 1s edge. The time-of-flight-mass-spectra measured after x-ray ionization of pyrrole(H_2O) is shown in Figure 7.5 [294]. In addition to the ionic fragments originated from the fragmentation of the pyrrole ring, we observed m/q peaks at $m/q = 18$ u/e and $m/q = 19$ u/e, which corresponds to H_2O^+ and H_3O^+, respectively. These channels were not observed in the Figure 7.4, and hence we rule out the probability for the absence of these channels in pyrrole(H_2O) as a reason for not observing these channels in our experiments performed at PETRA. The charge and mass transfer across the hydrogen-bond in pyrrole(H_2O) can be caused by any of the following relaxation pathways after core-shell ionization, such as intermolecular coulombic decay (ICD) [147], electron transfer mediated decay (ETMD) [202], or proton transfer mediated charge separation (PTMCS) [48]. For a detailed investigation of the fragmentation dynamics of pyrrole(H_2O), we have applied for further beamtime at EuXFEL, and the planned schedule is beyond the timescales of this thesis work.

7.6.2 Toward time-resolved photophysics of pyrrole(H_2O)

Site-specific x-ray photophysics investigations in pyrrole(H_2O) hint towards the charge- and mass- transfer processes occurring across the hydrogen-bond after core-shell ionization. The electron- and proton- transfer across the hydrogen-bond was observed, in chapter 5, after valence-shell ionization of pyrrole(H_2O). These channels showed the potential as radiation-protection pathways, to reduce the breaking of the C-C or N-C covalent bonds of the aromatic ring, after double valence ionization. As the observed Coulomb explosion pathways for $C_4H_5N^{2+}$ and $C_4H_5N^{3+}$ were similar for inner-shell and outer-valence ionization, one can expect a similar trend for pyrrole(H_2O) as well.

In the microsolvated pyrrole(H_2O) cluster, the observed electron- and proton-transfer channels can act as relaxation channels for pyrrole$(H_2O)^{2+}$ and pyrrole$(H_2O)^{3+}$ states created following inner-shell ionization. Another interesting aspect of the electron- and proton- transfer mechanisms are their potential to play as a radiation protection mechanism for core-shell ionized biomolecules in the solvent environment. Based on these observations, pyrrole(H_2O) is a good model system to study the phenomenon like intermolecular coulombic decay (ICD) [147], electron-transfer mediated decay (ETMD) [202], or proton-transfer mediated charge separation (PTMCS) [48], occurring after core-shell ionization. The full characterization of the fragmentation pathways of core-shell ionized bare pyrrole and microsolvated pyrrole(H_2O) cluster also brings the possibility of using x-rays as a probe for tracking hydrogen-bond breaking dynamics in pyrrole(H_2O).

Furthermore, we planned electron-ion coincidence measurements aiming at time-resolved photophysics studies on pyrrole(H_2O), e. g., in ultrafast UV/IR pump and x-ray probe experiments. One of the interesting experiments is to probe the neutral dissociation dynamics of the pyrrole(H_2O), initiated by a single UV-photon excitation or mode-selective IR excitation. In general, such studies can shed insight into fragmentation dynamics of solvated biomolecules, nature of the hydrogen bonds, and elucidating the radiation damage effects of solvated biological model systems.

8 Conclusions and Outlook

The incentive of the work performed in this thesis is real-time imaging of the relaxation pathways of microsolvated biomolecules in the gas phase after photoexcitation or ionization. Understanding the dynamic nature of the hydrogen-bonding, and their influence on the photophysics of biological systems is of universal importance in chemistry and biochemistry. Recording the dynamical structural changes in solvated biomolecules with high spatial and temporal resolution can unravel the mechanisms of their photophysics or photochemistry. In the last decades, fast and unprecedented progress is being made to record the quantum molecular movie of molecules in action with the evolution of ultrafast light sources and imaging methodologies to get structural information. The work performed in the framework of this thesis paves the way to the aforementioned dynamical studies on solvated molecules through a systematic photophysics investigation of an isolated and microsolvated biomolecule. Such comparative studies to investigate the influence of a single water molecule on the photophysics of a biomolecule can answer the existing uncertainties related to the role of the solvent environment, for example, whether it has protective or enhancing effects on radiation-induced biomolecular damage. Moreover, this study aims at bridging the gap between the isolated and solvated molecules in general, as well as at understanding the significance of hydrogen bonding in biology.

Two important milestones have been achieved in this thesis. The first one was the preparation of a cold and pure molecular beam of microsolvated clusters, which was difficult to achieve in a cluster beam. The second one was the comparative photophysics investigation of the isolated and microsolvated molecule after outer-valence and core-shell ionization. The photophysics of model-systems, pyrrole, and pyrrole(H_2O), was studied by velocity map imaging of the 3D-momenta of all ions, which originated from the fragmentation process. In chapter 3, the methodology to improve the spatial separation of size-selected clusters is focused. In chapter 4, it is demonstrated that a cold and pure molecular beam of pyrrole(H_2O) clusters is prepared. In chapter 5 and chapter 6, the photophysics investigation owing to strong-field ionization is included, while the scenario of site-specific core-shell ionization is focused in chapter 7.

In the following section, a summary of the outcome of this thesis is given, together with conclusions and an outlook on prospective projects to extend the work presented in this thesis in the future.

8.1 Achieving a pure beam of microsolvated cluster

A knife-edge skimming technique for shaping a molecular beam to improve the spatial separation of the different species in a molecular beam by the electrostatic deflector is described in the chapter 3. A vertically adjustable sharp razor blade was implemented near to the exit of the deflector, to clip off the deflected part of the beam. The combined experimental setup increases the column density of the selected molecular-beam part in the interaction zone, which corresponds to higher signal rates. Also, it enhances the contrast for the spatial separation of different molecular species from each other as well as from atomic seed gas. The demonstration of the advantage of using the combination of the knife-edge with the electrostatic deflector was shown through the separation of indole and indole-water clusters. An observation of better separation of $C_8H_7N–H_2O$ from indole and higher clusters was achieved, in comparison to our previous experiments on this system without the knife edge [76, 86]. The demonstrated setup is beneficial for molecular beam experiments that demand a strong separation of molecular species or a strong separation from the seed gas.

In chapter 4, the generation of a pure molecular beam of pyrrole and pyrrole(H_2O) clusters was achieved, the crucial ingredient of the photo-physics investigations employed on this thesis. The generation of a pure, sub-Kelvin rotationally cold beam of size-selected clusters was demanding and was difficult to achieve before. Here, the cluster selection was accomplished using the electrostatic deflector, which dispersed different species in a molecular beam based on their effective-dipole-moment-to-mass ratios. We demonstrated the spatial separation of pyrrole and pyrrole(H_2O) clusters from the other atomic and molecular species in a supersonically-expanded beam of pyrrole and traces of water seeded in high-pressure helium gas. The pyrrole(H_2O) cluster was well separated from other species in a molecular beam, i. e., from pyrrole, water, larger clusters, and the seed gas. The obtained pyrrole(H_2O) cluster beam had a purity of ~100 %. The experimental results were quantitatively supported by Monte-Carlo trajectory simulations. The extracted rotational temperature of pyrrole and pyrrole(H_2O) from the original supersonic expansion is $T_{\text{rot}} = 0.8 \pm 0.2$ K, whereas the temperature of the deflected, pure-pyrrole(H_2O) part of the molecular beam is approximated to $T_{\text{rot}} \approx 0.4$ K. To our best knowledge, it was the first time that a pure and sub-Kelvin rotationally cold molecular beam of microsolvated clusters was created.

The presented experimental approach in the chapter 3 helped to enhance the column density of the size-selected cluster beam and removal of the contributions from the seeding gas. This strategy is especially useful for experiments with lower count rates or restricted measurement times, e. g., beamtimes at large facilities such as free-electron lasers (FELs), synchrotrons, or high-power-laser facilities. The obtained pure beams of pyrrole(H_2O) in chapter 4, provide a crucial ingredient for photophysics studies aiming at time-resolved hydrogen bond formation/dissociation dynamics, e. g., in ultrafast laser pump and x-ray probe experiments. Further interesting aspects of the created sub-Kelvin rotationally cluster beam will be the control of the orientation in the laboratory frame by laser aligning or mixed-field orienting pyrrole(H_2O) clusters [104, 115, 116]. The separated pure species are also ideally suited for experiments to image the structure and dynamics of the pyrrole(H_2O) complex in the molecular frame, e. g., through molecular-frame photoelectron angular distributions (MFPADs), recoil-frame photoelectron angular distributions (RFPADs), gas-phase x-ray diffraction, or laser-induced electron diffraction (LIED) experiments [65, 103, 228, 229].

8.2 Photophysics investigations on model microsolvated systems

The photophysics studies performed on the model systems, pyrrole and pyrrole(H_2O) after strong-field and site-specific x-ray ionization, to mimic the radiation induced-damage effects on the biological matter are focused on chapters 5 to 7. A combination of time- and position-sensitive detectors, Timepix3 and delay-line detectors, together with a velocity-map imaging spectrometer was utilized for the fragmentation studies by simultaneous imaging of 3D-momenta of all ions.

In chapter 5, an experimental observation of a single hydrogen-bonded water molecule acting as a radiation protection agent for ionized pyrrole, a prototypical aromatic biomolecule, is demonstrated. Pyrrole and its microsolvated pyrrole(H_2O) cluster are ionized by intense 800 nm laser pulses mimicking radiation damage through outer-valence ionization. Both species were strong-field ionized through the removal of electrons from the HOMO or HOMO$-$1 orbitals, which are localized on the aromatic ring. We experimentally investigated the damage incurred in singly and doubly ionized pyrrole molecules and the effect of solvation by comparing the fragmentation pathways of bare pyrrole and microsolvated pyrrole(H_2O) heterodimers using pure samples of either species. For bare pyrrole (C_4H_5N), the initially produced pyrrole$^+$ and pyrrole^{2+} ions fragmented through the breaking of the C–C or N–C covalent bonds. However, for the microsolvated pyrrole, the initially generated pyrrole(H_2O)$^+$ shows strong protection of the pyrrole ring through dissociation of the neutral water molecule from the cluster or by transferring an electron or proton across the hydrogen bond. Furthermore, for pyrrole(H_2O) a smaller probability for double ionization was observed. Overall, a hydrogen-bonded single water molecule strongly reduces the fragmentation probability, and thus the persistent radiation damage of ionized pyrrole. In aqueous solution, the loss of the attached, neutral, ionized, or protonated, water could easily be repaired by the many solvent molecules around.

In chapter 6, it is demonstrated experimentally the observation of enhanced ionization for pyrrole(H_2O) in the strong-field regime at a laser intensity of $\sim 1 \times 10^{14}$ W/cm^2. The systematic investigation on a pure sample of pyrrole and pyrrole(H_2O) paved a way to elucidate that the highly-charged carbon species are only observed for pyrrole(H_2O), but not in pyrrole monomer. The observation of inner-shell ionized carbon atoms from pyrrole(H_2O) after strong-field ionization is surprising at this lower peak laser intensity, and it is the first time an enhanced core-shell ionization in such a small dimer system. We attributed the reason for this to a charge-resonance enhanced ionization mechanism together with internal ionization barrier suppression during the ionization processes and possibilities of electron-impact ionization for the removal of inner-shell electrons. However, the mechanism for core-shell ionization in the strong-field regime is still an open question. Our experimental results call for the relevance of considering the laser-driven electron re-collisions and electron correlation effects in molecular clusters in the strong-field regime, and the necessities for the extensive theoretical framework that can explain enhanced inner-shell ionization phenomena observed in molecular complexes. Moreover, our experimental studies propose pyrrole(H_2O) as a simple model system, where the mechanisms of inner-shell ionization in the strong-field regime can be investigated in the future, both experimentally and theoretically.

Next, the x-ray photophysics studies on pyrrole and pyrrole(H_2O) are discussed on chapter 7. x-ray radiation of energy of 420 eV was used for site-specific ionization of both species at its nitrogen atom, to mimic the role of the solvent environment on radiation damage after localized core-shell ionization of biomolecule. An electron-ion coincidence imaging technique, using a combination of double-sided velocity map imaging spectrometer and the delay-line detector was employed. The fragmentation studies aimed to investigate ultrafast relaxation processes like intermolecular Coulombic decay (ICD), electron-transfer mediated decay (ETMD), or proton-transfer mediated charge separation (PTM-CS) in hydrogen-bonded systems. The photo-fragmentation of the pyrrole showed that the monomer is primarily fragmented from the di-cationic state. For pyrrole(H_2O), we observed the charge- and mass-transfer across the hydrogen-bond. Additional insight into the nature of cationic states and fragmentation studies of pyrrole(H_2O) were limited due to technical issues during the beam-time, and such investigations are planned for future.

In summary, the systemic photophysics studies through ionization at the pyrrole moiety of the pure monomer and microsolvated cluster lead to the following conclusions. The aromatic ring is significantly protected for the microsolvated cluster as compared to monomer upon single and double outer-valence ionization. Therefore, water played the role of a radiation protection agent for an outer-valence ionized biomolecule, pyrrole. The enhanced ionization in pyrrole(H_2O) had a catalytic effect on radiation damage although it is a weak channel. Surprisingly, this phenomenon resulted in the creation of core-shell ionized carbon species in the strong-field regime at a laser peak intensity of $\sim 1 \times 10^{14}$ W/cm^2. The highly-charged carbon ions have implications on cancer treatment through the development of a cost-efficient and clean source for ion therapy, utilizing the cluster beam as compared to conventional methods using stripper materials [287]. In addition to strong-field studies, the direct core-shell ionization studies using soft x-rays manifest at probing the ultrafast rearrangement and relaxation processes occurring in biomolecules facilitated by their hydration environment.

8.3 Outlook: Toward the recording of molecular movies of microsolvated clusters

In nature, the solvent environment surrounding the biological system is always dynamic, through an active network of hydrogen-bonds. Hence, understanding the nature of hydrogen-bond networks, bond-formation, and bond-breaking dynamics are of universal importance in chemistry and biochemistry. So far, we discussed investigations performed to study the significance of hydrogen-bonded water in the photophysics of biomolecule, pyrrole. Real-time observation of the photodissociation dynamics is required to investigate the role of the dynamic solvent environment on the photophysics of biomolecules. Moreover, these studies will provide deeper insights into the relaxation pathways in biological systems initiated through the hydrogen-bond interactions, after photo-excitation, or ionization.

To achieve the above-mentioned dynamic studies, in line with the photo-fragmentation studies that formed this thesis, I have made significant contributions to time-resolved ion imaging investigations after photoexcitation or ionization of model systems, indole(H_2O), and pyrrole(H_2O). In general, these experiments intended to study how the photo-fragmentation and charge redistribution upon x-ray absorption is influenced due to the presence of a single water molecule as a function of its distance to the biomolecule. To change the distance between the two moieties, we initiated a photodissociation of the neutral indole(H_2O) cluster. The solute-solvent interaction in an electronically excited indole(H_2O) cluster was explored by studying the (dis)solvation dynamics through UV-pump (266 nm) - site-specific x-ray probe (N 1s, 420 eV) photoion-photoion coincidence (PIPICO) imaging, using a free-electron laser source at LCLS. We observed electron- and proton-transfer pathways in microsolvated indole(H_2O) clusters, which is dependent on the distance of the water molecule from the indole molecule. Additionally, we performed experiments to study the dissociation dynamics of the neutral water from the pyrrole(H_2O) cluster, after the single ionization. The dissociation dynamics were investigated by photoion-photoion coincidence (PIPICO) imaging, through IR-pump (1030 nm) and x-ray probe (420 eV), utilizing the EUXFEL light source. Observing these ion fragmentation dynamics paves the way to disentangle the role of a dynamic solvent environment on the photophysics of biomolecules.

As a next step towards recording a molecular movie, i. e., to unravel underlying mechanisms for the observed photophysics of solvated biomolecules after photoionization or excitation, a time-resolved electron-ion coincidence measurement has to be performed. For this, we have planned time-resolved photoelectron photoion-photoion coincidence (PEPIPICO) imaging experiments on pyrrole(H_2O), through UV/IR-pump and x-ray probe (420 eV), utilizing the EUXFEL light source. Also, we anticipate elucidating details of electron- and proton-transfer pathways observed in pyrrole(H_2O) after core-shell ionization. To realize such coincidence experiments, one could use well-known techniques such as the reaction microscopes, Cold Target Recoil Ion Momentum Spectroscopy (COLTRIMS) [295]. However, for experiments, we planned to use a double-sided velocity map imaging spectrometer together with a time- and position-sensitive detector, such as Timepix3[206, 207].

Another aim is to track the ground-state dynamics of the microsolvated pyrrole(H_2O) *via* investigating the hydrogen-bond dissociation after bond-selective excitation of the cluster. Most of the biological reactions in nature occur in their ground state, and hence, this attempt will guide us to probe and steer the bond-breaking or bond-formation processes in the ground state.

A complementary approach for recording the electron and nuclear dynamics is the time-resolved diffractive imaging in the molecular frame, either using x-rays or electron beams. The emerging self diffraction techniques, such as LIED [228, 258–261], is also a promising methodology to track the structural changes with high spatial and temporal resolution. To get the structural information it is required to control the orientation of the cluster in the laboratory frame by laser alignment or mixed-field orientation [104, 115, 116]. Utilizing these advanced imaging techniques together with pure and controlled cluster samples, we envisage shedding light on fundamental processes occurring in nature, such as hydrogen-bond breaking, through real-time imaging, i. e., by recording their molecular movies, in the near future.

A Appendix to Chapter 5

A.1 Analysis to distinguish Coulomb explosion and Dissociative ionization channels

A Photo-ion Photo-ion Coincidence (PIPICO) analysis was performed to identify ion pairs that are correlated among all ions originated after strong-field ionization of both pyrrole and pyrrole(H_2O). The coincidence map was therefore built between two ions for all possible combinations of ions present in the TOF-MS spectrum. Strong-field ionization of both pyrrole and pyrrole(H_2O) leads to complex fragmentation processes, and hence, identification of the real correlated ion pairs is not easy from a normal coincidence map. To distinguish between ionic fragments within the same mass-to-charge region, which were formed either after the Coulomb explosion or dissociative ionization process, an additional gate was implemented on the velocity space for these ions while building the coincidence map. An example of this sorting procedure for all ions is shown for the case of the pyrrole monomer Figure A.1.

The PIPICO spectra obtained for the pyrrole monomer, after gating separately on low- and high- kinetic energy regions of the velocity map image for all ions are shown in Figure A.1. A uniform cut was made on velocity map images with radii of 0.6 km/s. The VMI image of all high kinetic energy ions and the obtained coincidence map is shown

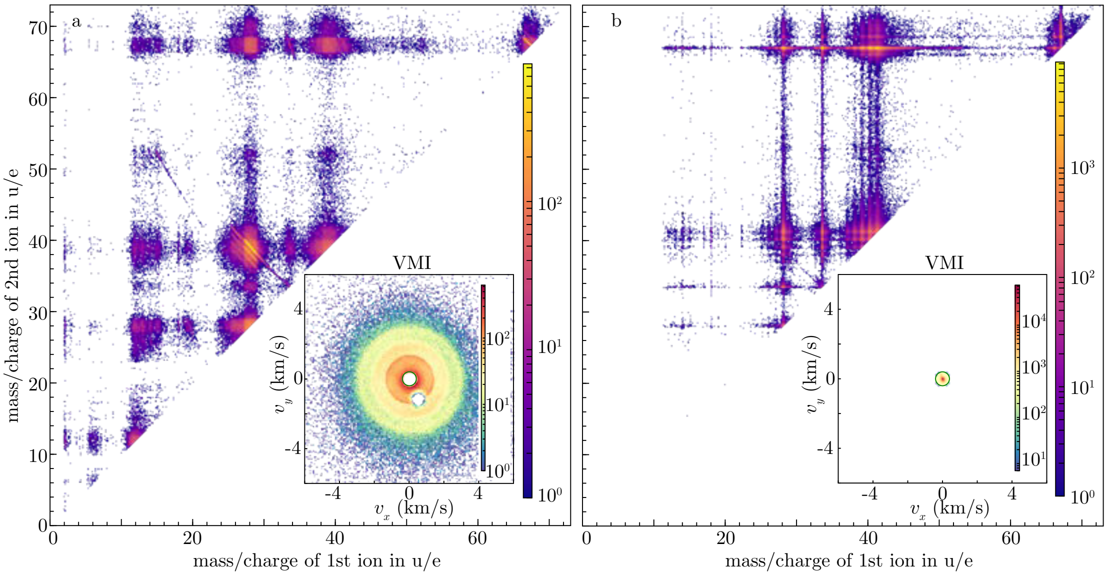

Figure A.1. a) The Photo-ion Photo-ion Coincidence (PIPICO) map for all high kinetic energy ions created after strong-field ionization of pyrrole. Inset shows the velocity map image of all ions after sorting out low kinetic region (circle in the centre) and background ions (circle in the lower right quadrant). b) The PIPICO map for all low kinetic energy ions created after strong-field dissociative ionization of pyrrole. The velocity map image of all low kinetic energy ions is also shown.

in Figure A.1 a. The ions created due to ionization of the chamber background (mainly water) were also gated out, which results in the empty circular blob on the lower right quadrant of the velocity map image. Ions with high kinetic energy are correlated. These channels mainly resulted from Coulomb explosion after double- and triple ionization of the pyrrole. A straight line coincidence island (slope = -1) corresponds to two-body axial fragmentation processes owing to Coulomb repulsion. Again coincidence lines with slope $<$ -1, are originated from two-body fragmentation processes, where the mass-to-charge ratio of one correlated ion is significantly lower than the other. A washed-out coincidence island between ion pair is a signature that they originated from the multi-body fragmentation process of the parent molecule. All the main observed ring-break up channels of pyrrole after double ionization are well observed in the PIPICO spectrum.

The PIPICO created after gating on the low kinetic region of the velocity map image of all ions is shown in Figure A.1 b. These low energy ions are uncorrelated, and hence they appear as false coincidences in the coincidence map. These channels are caused by the dissociation process, which results in one ion, and remaining are neutral products.

A.2 Estimation of contamination from the water dimer to the water ion channel of pyrrole(H_2O)

The water dimer is also present in the deflected part of our molecular beam, where measurements for pyrrole(H_2O) was performed. This leads to contamination in the water ion channel of pyrrole(H_2O), due to water ions originated from the water dimer. A photo-ion photo-ion correlation (PIPICor) analysis, with constraints by following momenta conservation can help to distinguish between water ion formed after Coulomb explosion of either water dimer or pyrrole(H_2O).

In order to identify correlating pairs of ions in pyrrole(H_2O) beam, momentum conservation has been employed by (i) building all shot-wise combinations of ions, (ii) deducing all possible fragment masses, $m_{ij} = (m/z)_i \cdot z_j$ from the mass/charge values and implying fragment charges of $z_j = +1, +2$, and (iii) computing the composite two-dimensional momenta, $m_{ij} \cdot \mathbf{v}_i + m_{kl} \cdot \mathbf{v}_k$, for each pair of fragments. The composite momentum is a very sensitive observable for this identification, where the true correlations add-up to values close to zero. These true correlations are clearly separated from the uncorrelated ones, whose composite momenta do not add-up to values close to zero, and therefore specific gates can be employed to get PIPICor maps Figure A.2 of true correlations corresponding to an axial recoil fragmentation. The two-body break-up channels after double ionization of pyrrole(H_2O) and water dimer are given in Table A.1. The contribution from the water dimer with respect to all intact double ionization channels of pyrrole(H_2O) is 7%.

The estimation for contamination in the low kinetic energy part of the velocity map image is not easy, due to the complexity to distinguish the water ion formed after dissociative single ionization of pyrrole(H_2O) and the water-dimer. Hence, the same contamination (7%)

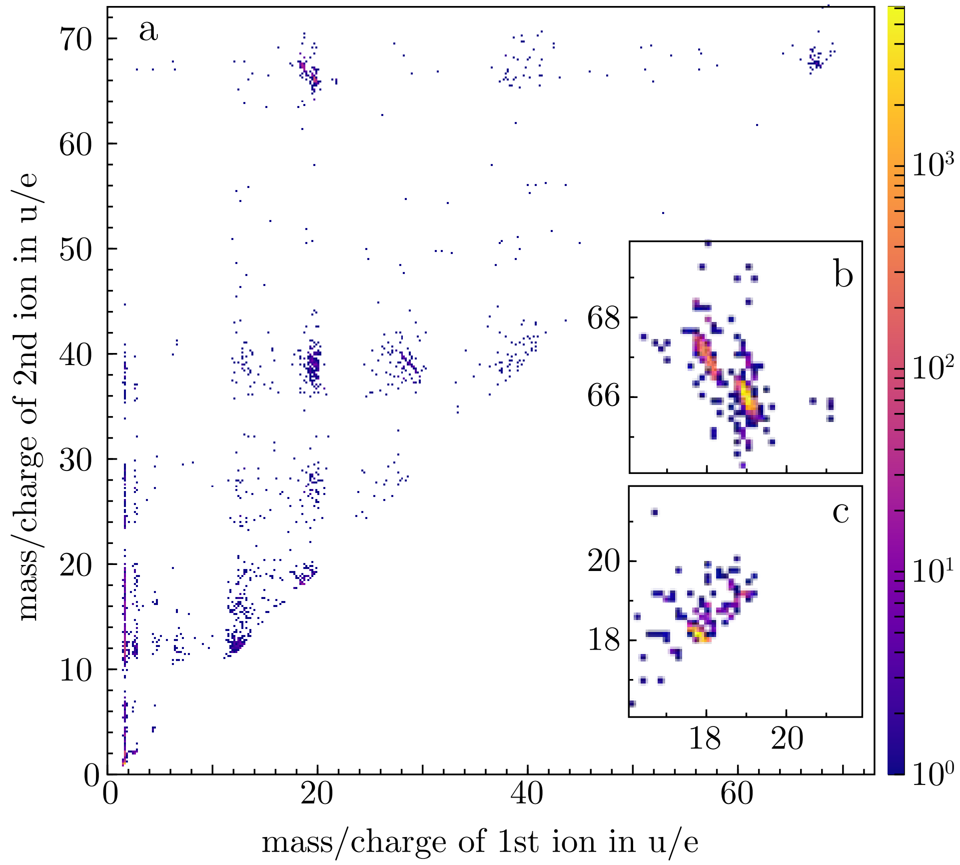

Figure A.2. a) The photo-ion photo-ion correlation (PIPICor) map showing all correlated pair of ions after strong-field ionization of pyrrole(H_2O). Insets show zoomed in to the observed two-body fragmentation channels of pyrrole(H_2O) (b) and the water dimer (c).

cluster type	correlated island	counts
pyrrole(H_2O)	67 & 18	304
pyrrole(H_2O)	66 & 19	995
water dimer	18 & 18	102

Table A.1. The table shows counts for correlated ions pairs originated from double ionization of pyrrole(H_2O) and water dimer.

is assumed for single ionization channels as well. The contamination from the water dimer is also incorporated for the estimation of the over-all ring protection ratios (i. e., comparison of pyrrole and pyrrole(H_2O)) after single- and double- ionization. It does not change the protection ratio significantly i. e., only by less than 0.5%, and therefore a contribution from the water dimer can be even neglected.

A.3 Specific cuts on the momenta map for specific ionization channels of pyrrole and pyrrole(H_2O)

The ring-fragmentation probabilities for pyrrole and pyrrole(H_2O) after single- and double-ionization was estimated by counting the ions in the background-subtracted momentum-map images.

For single ionization, the probabilities were then determined by counting the ions in the momentum-map images with a gate on the low kinetic energy part in the specific mass-to-charge regions. The gates made for different single ionization channels are marked by white circles in the specific mass-to-charge regions, as shown in Figure A.3 for pyrrole and in Figure A.4 for pyrrole(H_2O). In this case, we also estimated the projection of the Coulomb explosion rings to the center of the momenta map statistically.

In the case of double ionization, the probabilities were extracted by counting the ions in the momentum-map images with a gate on the high kinetic energy part in the specific mass-to-charge regions. The gates made for different Coulomb explosion channels owing to double ionization are represented by green circles in the specific mass-to-charge regions, as shown in Figure A.3 for pyrrole and in Figure A.4 for pyrrole(H_2O). In this case, it is important to mention that the intact $C_4H_5N^{2+}$ appears in the low kinetic energy region of the momenta map due to the low kinetic energy for intact ions. Here, we added the estimated ions counts due to the projection of the Coulomb explosion rings to the center of the momenta map.

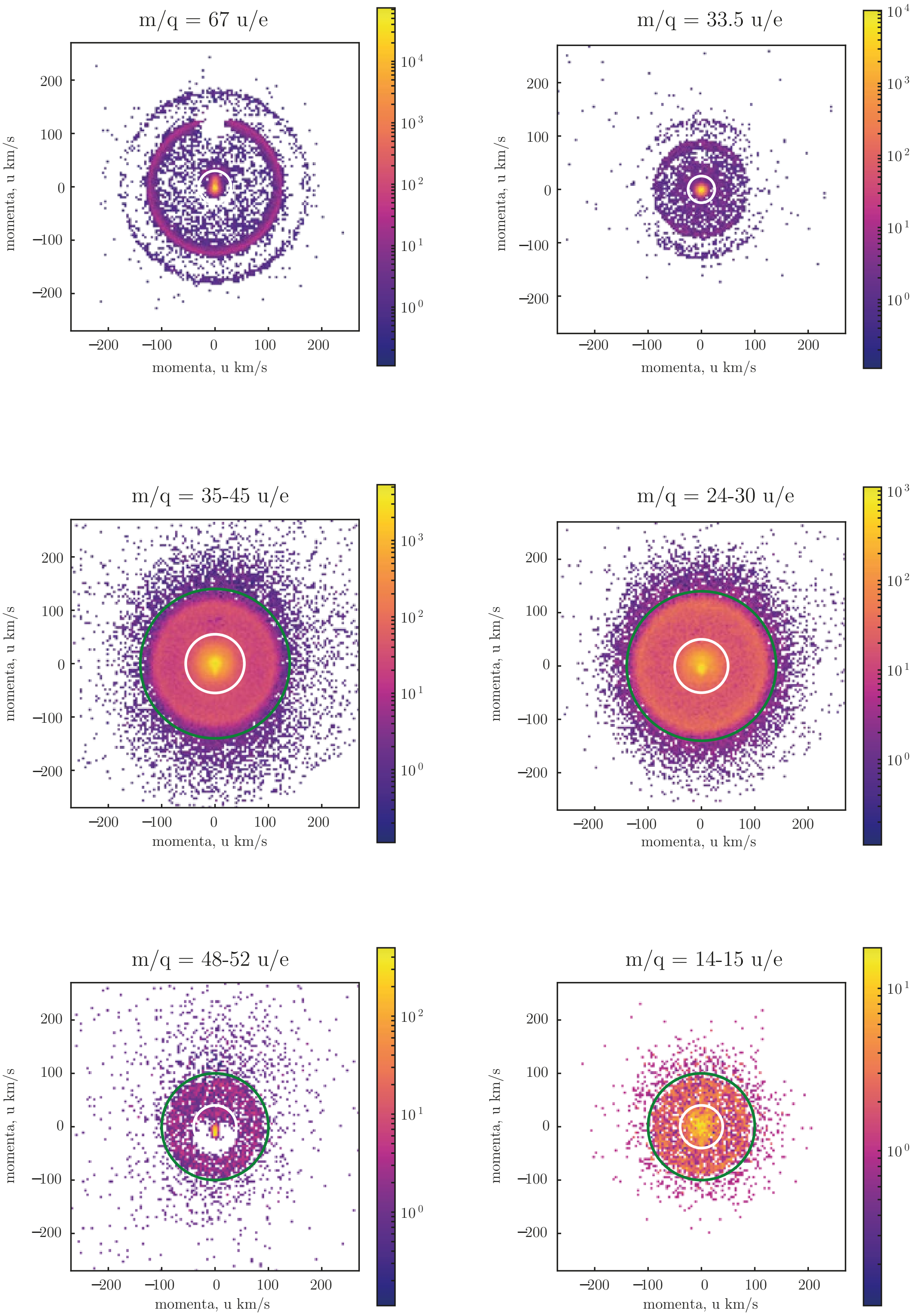

Figure A.3. The momentum map for all ions detected after strong-field ionization of pyrrole. Marked white and green circles with specific radii in the momenta map represent edges for single- and double- ionization channels, respectively.

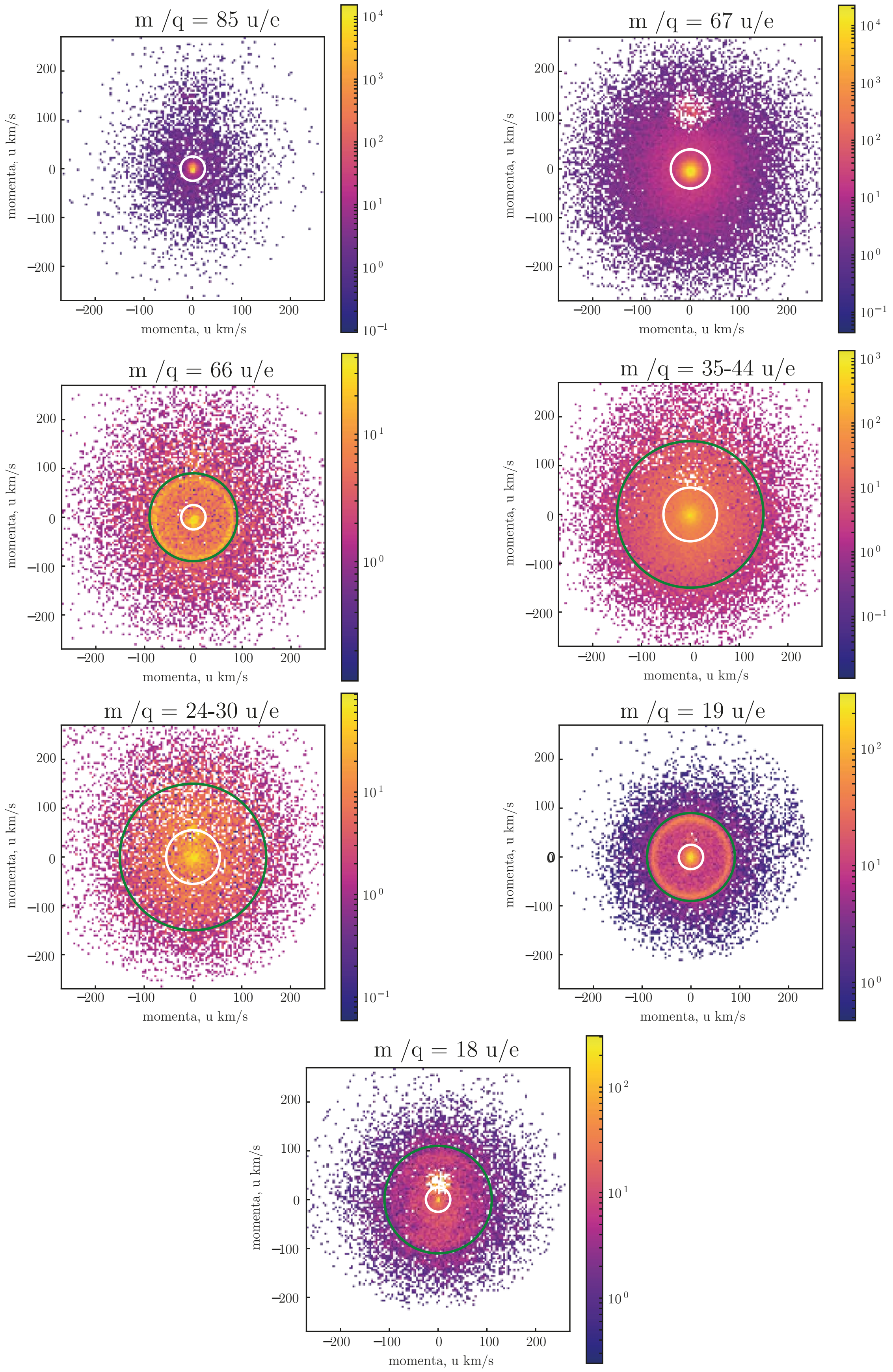

Figure A.4. The momentum map for all ions detected after strong-field ionization of pyrrole(H_2O). Marked white and green circles with specific radii in the momenta map represent edges for single- and double- ionization channels, respectively.

Bibliography

[1] Albert Szent-Györgyi. Biology and pathology of water. *Perspectives in Biology and Medicine*, 14(2):239–249, 1971. doi: 10.1353/pbm.1971.0014. URL `https://doi.org/10.1353/pbm.1971.0014`.

[2] Lynn J Rothschild and Rocco L Mancinelli. Life in extreme environments. *Nature*, 409(6823):1092–1101, February 2001. doi: 10.1038/35059215. URL `http://www.nature.com/doifinder/10.1038/35059215`.

[3] Philip Ball. Water is an active matrix of life for cell and molecular biology. *PNAS*, 114(51):13327–13335, 2017. doi: 10.1073/pnas.1703781114. URL `https://doi.org/10.1073/pnas.1703781114`.

[4] Frances Westall and A Brack. The importance of water for life. *Space Science Reviews*, 214(2):50, 2018. doi: 10.1007/s11214-018-0476-7.

[5] R. Lynden-Bell, S. Morris, J. Barrow, J. Finney, and C. Harper, editors. *Water and Life*. CRC Press, Boca Raton, 2010. ISBN 9780429191039. URL `https://doi.org/10.1201/EBK1439803561`.

[6] Philip Ball. Seeking the solution. *Nature*, 436:1084–1085, 2005. doi: 10.1038/4361084a. URL `https://doi.org/10.1038/4361084a`.

[7] Marie-Claire Bellissent-Funel, Ali Hassanali, Martina Havenith, Richard Henchman, Peter Pohl, Fabio Sterpone, David van der Spoel, Yao Xu, and Angel E Garcia. Water determines the structure and dynamics of proteins. *Chem. Rev.*, 116(13):7673–7697, 2016. ISSN 0009-2665. doi: 10.1021/acs.chemrev.5b00664.

[8] Carlos E Crespo-Hernández, Boiko Cohen, Patrick M Hare, and Bern Kohler. Ultrafast excited-state dynamics in nucleic acids. *Chem. Rev.*, 104:1977–2020, 2004. doi: 10.1021/cr0206770. URL `https://doi.org/10.1021/cr0206770`.

[9] Damien Laage, Thomas Elsaesser, and James T Hynes. Water dynamics in the hydration shells of biomolecules. *Chem. Rev.*, 117(16):10694–10725, 2017. ISSN 0009-2665. doi: 10.1021/acs.chemrev.6b00765. URL `https://pubs.acs.org/doi/10.1021/acs.chemrev.6b00765`.

[10] Biman Bagchi. Water dynamics in the hydration layer around proteins and micelles. *Chem. Rev.*, 105(9):3197–3219, 2005. ISSN 0009-2665. doi: 10.1021/cr020661+. URL `https://pubs.acs.org/doi/10.1021/cr020661%2B`.

[11] Olivier Collet. How does the first water shell fold proteins so fast? *J. Chem. Phys.*, 134(8):085107, 2011. doi: 10.1063/1.3554731. URL `https://doi.org/10.1063/1.3554731`.

[12] David W. Pratt. High resolution spectroscopy in the gas phase: Even large molecules have well-defined shapes. *Annual Review of Physical Chemistry*, 49(1): 481–530, 1998. URL `http://physchem.annualreviews.org/cgi/content/abstract/49/1/481`.

[13] Steven T Shipman and Brooks H Pate. *New Techniques in Microwave Spectroscopy*, chapter 36, pages 801–827. John Wiley & Sons, Ltd, Chichester, UK, September 2011.

[14] Kurt Wüthrich. NMR studies of structure and function of biological macromolecules (Nobel lecture). *Angew. Chem. Int. Ed.*, 42(29):3340–3363, 2003. ISSN 1521-3773. doi: 10.1002/anie.200300595. URL `http://dx.doi.org/10.1002/anie.200300595`.

[15] Cristóbal Pérez, Matt T. Muckle, Daniel P. Zaleski, Nathan A. Seifert, Berhane Temelso, George C Shields, Zbigniew Kisiel, and Brooks H Pate. Structures of cage, prism, and book isomers of water hexamer from broadband rotational spectroscopy. *Science*, 336(6083):897–901, May 2012. ISSN 1095-9203. doi: 10.1126/science.1220574. URL `http://www.ncbi.nlm.nih.gov/pubmed/22605772`.

[16] H. N. Chapman, A. Barty, M. J. Bogan, S. Boutet, S. Frank, S. P. Hau-Riege, S. Marchesini, B. W. Woods, S. Bajt, W. H. Benner, London W. A., E. Plönjes, M. Kuhlmann, R. Treusch, S. Düsterer, T. Tschentscher, J. R. Schneider, E. Spiller, T. Möller, C. Bostedt, M. Hoener, D. A. Shapiro, K. O. Hodgson, D. van der Spoel, F. Burmeister, M. Bergh, C. Caleman, G. Huldt, M. M. Seibert, F. R. N. C. Maia, R. W. Lee, A. Szöke, N. Timneanu, and J. Hajdu. Femtosecond diffractive imaging with a soft-x-ray free-electron laser. *Nat. Phys.*, 2:839–843, 2006. doi: 10.1038/nphys461. URL `http://dx.doi.org/10.1038/nphys461`.

[17] H. N. Chapman. Facility and method for molecular structure determination, April 2014. URL `http://worldwide.espacenet.com/publicationDetails/biblio?FT=D&date=20130424&DB=EPODOC&locale=en_EP&CC=EP&NR=2584347A1&KC=A1&ND=4`. EP Patent 2584347; US Patent 20130101086.

[18] Anton Barty, Jochen Küpper, and Henry N. Chapman. Molecular imaging using x-ray free-electron lasers. *Annu. Rev. Phys. Chem.*, 64(1):415–435, April 2013. doi: 10.1146/annurev-physchem-032511-143708. URL `http://dx.doi.org/10.1146/annurev-physchem-032511-143708`.

[19] R. J. Dwayne Miller, Ralph Ernstorfer, Maher Harb, Meng Gao, Christoph T Hebeisen, Hubert Jean-Ruel, Cheng Lu, Gustavo Moriena, and German Sciaini. 'Making the molecular movie': First frames. *Acta Crystallogr A*, 66:137–156, Jan 2010. doi: 10.1107/S0108767309053926. URL `http://www3.interscience.wiley.com/journal/123291799/abstract`.

[20] R J Dwayne Miller. Femtosecond crystallography with ultrabright electrons and x-rays: capturing chemistry in action. *Science*, 343(6175):1108–1116, March 2014. doi: 10.1126/science.1248488.

[21] B. Testa and L. B. Kier. The concept of molecular-structure in structure activity relationship studies and drug design. *Med. Res. Rev.*, 11:35–48, 1991.

[22] A C Anderson. The process of structure-based drug design. *Chemistry & Biology*, 10(9): 787–797, sep 2003. doi: 10.1016/j.chembiol.2003.09.002. URL `http://linkinghub.elsevier.com/retrieve/pii/S1074552103001947`.

[23] Marcio F. Colombo, Donald C. Rau, and V. Adrian Parsegian. Protein solvation in allosteric regulation: A water effect on hemoglobin. *Science*, 256(5057):655–659, 1992. doi: 10.1126/science.1585178. URL `http://science.sciencemag.org/content/256/5057/655`.

[24] Catherine A. Royer. Probing protein folding and conformational transitions with fluorescence. *Chem. Rev.*, 106(5):1769–1784, 2006. doi: 10.1021/cr0404390.

[25] Timothy M. Korter, David W. Pratt, and Jochen Küpper. Indole-H_2O in the gas phase. Structures, barriers to internal motion, and $S_1 \leftarrow S_0$ transition moment orientation. Solvent reorganization in the electronically excited state. *J. Phys. Chem. A*, 102(37): 7211–7216, 1998. doi: 10.1021/jp982456x. URL `http://dx.doi.org/10.1021/jp982456x`.

[26] Samir Kumar Pal, Jorge Peon, and Ahmed H. Zewail. Biological water at the protein surface: Dynamical solvation probed directly with femtosecond resolution. *PNAS*, 99(4):1763–1768, 2002. doi: 10.1073/pnas.042697899. URL `https://www.pnas.org/content/99/4/1763`.

[27] Haruki Niwa, Satoshi Inouye, Takashi Hirano, Tatsuki Matsuno, Satoshi Kojima, Masayuki Kubota, Mamoru Ohashi, and Frederick I. Tsuji. Chemical nature of the light emitter of the Aequorea green fluorescent protein. *PNAS*, 93(24):13617–13622, 1996. doi: 10.1073/pnas.93.24.13617. URL `https://www.pnas.org/content/93/24/13617`.

[28] Matthew W. Forbes and Rebecca A. Jockusch. Deactivation pathways of an isolated green fluorescent protein model chromophore studied by electronic action spectroscopy. *J. Am. Chem. Soc.*, 131(47):17038–17039, 2009. doi: 10.1021/ja9066404. URL `https://doi.org/10.1021/ja9066404`.

[29] Chongand Fang, Renee R. Frontiera, Rosalie Tran, and Richard A. Mathies. Mapping GFP structure evolution during proton transfer with femtosecond raman spectroscopy. *Nature*, 462:200–204, 2009. doi: 10.1038/nature08527. URL `https://doi.org/10.1038/nature08527`.

[30] Manoj K Shukla and Jerzy Leszczynski. *Radiation Induced Molecular Phenomena In Nucleic Acids: A Brief Introduction*, pages 1–14. Springer Netherlands, Dordrecht, 2008. ISBN 978-1-4020-8184-2. doi: 10.1007/978-1-4020-8184-2_1. URL `https://doi.org/10.1007/978-1-4020-8184-2_1`.

[31] Shirley Lehnert. *Biomolecular Action of Ionizing Radiation*. Taylor & Francis, London, 2007. doi: 10.1201/9781420011920. URL `https://www.taylorfrancis.com/books/9780429145117`.

[32] Elahe Alizadeh, Thomas M. Orlando, and Léon Sanche. Biomolecular damage induced by ionizing radiation: The direct and indirect effects of low-energy electrons on DNA. *Annu. Rev. Phys. Chem.*, 66:379–398, 2015. doi: 10.1146/annurev-physchem-040513-103605. URL `https://www.annualreviews.org/doi/pdf/10.1146/annurev-physchem-040513-103605`.

[33] Hong-Keun Kim, Jasmin Titze, Markus Schöffler, Florian Trinter, Markus Waitz, Jörg Voigtsberger, Hendrik Sann, Moritz Meckel, Christian Stuck, Ute Lenz, Matthias Odenweller, Nadine Neumann, Sven Schössler, Klaus Ullmann-Pfleger, Birte Ulrich, Rui Costa Fraga, Nikos Petridis, Daniel Metz, Annika Jung, Robert Grisenti, Achim Czasch, Ottmar Jagutzki, Lothar Schmidt, Till Jahnke, Horst Schmidt-Böcking, and Reinhard Dörner. Enhanced production of low energy electrons by alpha particle impact. *PNAS*, 108:11821–11824, 2011. doi: 10.1073/pnas.1104382108. URL `https://www.pnas.org/content/108/29/11821`.

[34] Badia Boudaïffa, Pierre Cloutier, Darel Hunting, Michael A. Hues, and Leon Sanche. Resonant formation of DNA strand breaks by low-energy (3 to 20 ev) electrons. *Science*, 287(5458):1658–1660, 2000. doi: 10.1126/science.287.5458.1658. URL `https://science.sciencemag.org/content/287/5458/1658`.

[35] F Martin, P. D. Burrow, Z Cai, D Cloutier, Pand Hunting, and L Sanche. DNA strand breaks induced by 0–4 ev electrons: The role of shape resonances. *Phys. Rev. Lett.*, 93:068101, Aug 2004. doi: 10.1103/PhysRevLett.93.068101. URL `https://link.aps.org/doi/10.1103/PhysRevLett.93.068101`.

[36] Barry D. Michael and Peter O'Neill. A sting in the tail of electron tracks. *Science*, 187(5458):1603–1604, 2000. doi: 10.1126/science.287.5458.1603. URL `https://science.sciencemag.org/content/287/5458/1603`.

[37] Z.-H. Loh, G. Doumy, C. Arnold, L. Kjellsson, S. H. Southworth, A. Al Haddad, Y. Kumagai, M.-F. Tu, P. J. Ho, A. M. March, R. D. Schaller, M. S. Bin Mohd Yusof, T. Debnath, M. Simon, R. Welsch, L. Inhester, K. Khalili, K. Nanda, A. I. Krylov, S. Moeller, G. Coslovich, J. Koralek, M. P. Minitti, W. F. Schlotter, J.-E. Rubensson, R. Santra, and L. Young. Observation of the fastest chemical processes in the

radiolysis of water. *Science*, 367:179–182, 2020. doi: 10.1126/science.aaz4740. URL `https://science.sciencemag.org/content/367/6474/179`.

[38] Vít Svoboda, Rupert Michiels, Aaron C. LaForge, Jakub Med, Frank Stienkemeier, Petr Slavíček, and Hans Jakob Wörner. Real-time observation of water radiolysis and hydrated electron formation induced by extreme-ultraviolet pulses. *Science Advances*, 6:eaaz0385, 2020. doi: 10.1126/sciadv.aaz0385. URL `https://advances.sciencemag.org/content/6/3/eaaz0385`.

[39] Tilmann D Märk and Paul Scheier. Unexpected electrons. *Nat. Phys.*, 6(2):82–83, 2010. doi: 10.1038/nphys1526. URL `https://doi.org/10.1038/nphys1526`.

[40] Jun Ma, Furong Wang, Sergey A. Denisov, Amitava Adhikary, and Mehran Mostafavi. Reactivity of prehydrated electrons toward nucleobases and nucleotides in aqueous solution. *Science Advances*, 3(12):1–7, 2017. doi: 10.1126/sciadv.1701669. URL `https://advances.sciencemag.org/content/3/12/e1701669`.

[41] Jun Ma, Anil Kumar, Yusa Muroya, Shinichi Yamashita, Tsuneaki Sakurai, Sergey A. Denisov, Michael D. Sevilla, Amitava Adhikary, Shu Seki, and Mehran Mostafavi. Observation of dissociative quasi-free electron attachment to nucleoside via excited anion radical in solution. *Nat. Commun.*, 6:1, 2019. doi: 10.1038/s41467-018-08005-z. URL `https://doi.org/10.1038/s41467-018-08005-z`.

[42] Jiande Gu, Jerzy Leszczynski, and Henry F. Schaefer. Interactions of electrons with bare and hydrated biomolecules: From nucleic acid bases to DNA segments. *Chem. Rev.*, 112:5603–5640, 2012. doi: 10.1021/cr3000219. URL `https://doi.org/10.1021/cr3000219`.

[43] Xiaoguang Bao, Jing Wang, Jiande Gu, and Jerzy Leszczynski. DNA strand breaks induced by near-zero-electronvolt electron attachment to pyrimidine nucleotides. *PNAS*, 103(15):5658–5663, 2006. doi: 10.1073/pnas.0510406103. URL `https://www.pnas.org/content/103/15/5658`.

[44] M. Smyth, J. Kohanoff, and I. I. Fabrikant. Electron-induced hydrogen loss in uracil in a water cluster environment. *J. Chem. Phys.*, 140:184313, 2014. doi: 10.1063/1.4874841. URL `https://doi.org/10.1063/1.4874841`.

[45] T. Ito, S. C. Baker, C. D. Stickley, J. G. Peak, and M. J. Peak. Dependence of the yield of strand breaks induced by γ-rays in DNA on the physical conditions of exposure: Water content and temperature. *Int. J. Radiat. Biol.*, 63:289–296, 1993. doi: 10.1080/09553009314550391. URL `https://doi.org/10.1080/09553009314550391`.

[46] J Kočišek, A Pysanenko, M Fárník, and J Fedor. Microhydration prevents fragmentation of uracil and thymine by low-energy electrons. *J. Phys. Chem. Lett.*, 27:

3401–3405, 2016. doi: 10.1021/acs.jpclett.6b01601. URL `https://doi.org/10.1021/acs.jpclett.6b01601`.

[47] Milan Ončák, Hans Lischka, and Petr Slavíček. Photostability and solvation: photodynamics of microsolvated zwitterionic glycine. *Phys. Chem. Chem. Phys.*, 12(19): 4906–14, 2010. ISSN 1463-9076. doi: 10.1039/b925246k. URL `https://pubs.rsc.org/en/content/articlelanding/2010/cp/b925246k#!divAbstract`.

[48] Petr Slavíček, Nikolai V Kryzhevoi, Emad F Aziz, and Bernd Winter. Relaxation processes in aqueous systems upon x-ray ionization: Entanglement of electronic and nuclear dynamics. *The Journal of Physical Chemistry Letters*, 7(2):234–243, jan 2016. doi: 10.1021/acs.jpclett.5b02665. URL `http://pubs.acs.org/doi/10.1021/acs.jpclett.5b02665`.

[49] Enliang Wang, Xueguang Ren, WoonYong Baek, Hans Rabus, Thomas Pfeifer, and Alexander Dorn. Water acting as a catalyst for electron-driven molecular break-up of tetrahydrofuran. *Nat. Commun.*, 11:2194, 2020. doi: 10.1038/s41467-020-15958-7. URL `https://doi.org/10.1038/s41467-020-15958-7`.

[50] Michael J. Tubergen, Anne M. Andrews, and Robert L. Kuczkowski. Microwave spectrum and structure of a hydrogen-bonded pyrrole-water complex. *J. Phys. Chem.*, 97(29):7451–7457, 1993. doi: 10.1021/j100131a011. URL `https://doi.org/10.1021/j100131a011`.

[51] Andrew T. Ulijasz, Gabriel Cornilescu, Claudia C. Cornilescu, Junrui Zhang, Mario Rivera, John L. Markley, and Richard D. Vierstra. Structural basis for the photoconversion of a phytochrome to the activated Pfr form. *Nature*, 463:250–254, 2010. doi: 10.1038/nature08671. URL `https://www.nature.com/articles/nature08671`.

[52] M.N.R. Ashfold, B. Cronin, A. L. Devine, R.N. Dixon, and M. G. D. Nix. The role of $\pi\sigma^*$ excited states in the photodissociation of heteroaromatic molecules. *Science*, 312:1637–1640, 2006. doi: 10.1126/science.1125436. URL `http://science.sciencemag.org/content/312/5780/1637/tab-pdf`.

[53] A. L. Sobolewski, W. Domcke, C. Dedonder-Lardeux, and C. Jouvet. Excited-state hydrogen detachment and hydrogen transfer driven by repulsive $^1\pi\sigma^*$ states: A new paradigm for nonradiative decay in aromatic biomolecules. *Phys. Chem. Chem. Phys.*, 4:1093–1100, 2002. doi: 10.1039/B110941N. URL `http://dx.doi.org/10.1039/B110941N`.

[54] A. L. Sobolewski and W. Domcke. Conical intersections induced by repulsive $^1\pi\sigma^*$ states in planar organic molecules: malonaldehyde, pyrrole and chlorobenzene as photochemical model systems. *Chem. Phys.*, 259(2):181–191, 2000. doi: 10.1016/

S0301-0104(00)00203-2. URL `http://www.sciencedirect.com/science/article/pii/S0301010400002032`.

[55] H Lippert, V Stert, L Hesse, C P Schulz, I V Hertel, and W Radloff. Ultrafast photoinduced processes in indole-water clusters. *Chem. Phys. Lett.*, 376(1-2):40–48, jul 2003. doi: 10.1016/S0009-2614(03)00921-7. URL `http://linkinghub.elsevier.com/retrieve/pii/S0009261403009217`.

[56] Andrzej L Sobolewski and Wolfgang Domcke. Photoejection of electrons from pyrrole into an aqueous environment: ab initio results on pyrrole-water clusters. *Chem. Phys. Lett.*, 321(5-6):479–484, May 2000. doi: 10.1016/S0009-2614(00)00404-8. URL `http://linkinghub.elsevier.com/retrieve/pii/S0009261400004048`.

[57] A. H. Zewail. Femtochemistry: Atomic-Scale Dynamics of the Chemical Bond. *J. Phys. Chem. A*, 104(24):5660–5694, June 2000. doi: 10.1021/jp001460h. URL `https://dx.doi.org/10.1021/jp001460h`.

[58] J C Williamson, J M Cao, H Ihee, H Frey, and Ahmed H Zewail. Clocking transient chemical changes by ultrafast electron diffraction. *Nature*, 386(6621):159–162, 1997. doi: 10.1038/386159a0.

[59] Richard Neutze, Remco Wouts, David van der Spoel, Edgar Weckert, and Janos Hajdu. Potential for biomolecular imaging with femtosecond x-ray pulses. *Nature*, 406(6797):752–757, August 2000. doi: 10.1038/35021099. URL `http://dx.doi.org/10.1038/35021099`.

[60] M. Meckel, D. Comtois, D. Zeidler, A. Staudte, D. Pavičić, H. C. Bandulet, H. Pépin, J. C. Kieffer, R. Dörner, D. M. Villeneuve, and P. B. Corkum. Laser-induced electron tunneling and diffraction. *Science*, 320(5882):1478–1482, 2008. ISSN 0036-8075. doi: 10.1126/science.1157980. URL `http://science.sciencemag.org/content/320/5882/1478`.

[61] A H Zewail. Femtochemistry. Past, present, and future. *Pure & Appl. Chem.*, 72(12): 2219–2231, dec 2000. doi: 10.1351/pac200072122219.

[62] Ahmed H Zewail. Laser femtochemistry. *Science*, 242(4886):1645–1653, December 1988. doi: 10.1126%2Fscience.242.4886.1645. URL `https://doi.org/10.1126%2Fscience.242.4886.1645`.

[63] R. Srinivasan, V. A. Lobastov, C.-Y. Ruan, and A. H. Zewail. Ultrafast electron diffraction (ued). a new development for the 4d determination of transient molecular structures. *Helv. Chim. Acta.*, 86(40):1763, 2003. doi: 10.1002/chin.200340299.

[64] Ahmed H. Zewail. 4D ultrafast electron diffraction, crystallography, and microscopy. *Annu. Rev. Phys. Chem.*, 57:65–103, 2006.

[65] Jochen Küpper, Stephan Stern, Lotte Holmegaard, Frank Filsinger, Arnaud Rouzée, Artem Rudenko, Per Johnsson, Andrew V. Martin, Marcus Adolph, Andrew Aquila, Saša Bajt, Anton Barty, Christoph Bostedt, John Bozek, Carl Caleman, Ryan Coffee, Nicola Coppola, Tjark Delmas, Sascha Epp, Benjamin Erk, Lutz Foucar, Tais Gorkhover, Lars Gumprecht, Andreas Hartmann, Robert Hartmann, Günter Hauser, Peter Holl, Andre Hömke, Nils Kimmel, Faton Krasniqi, Kai-Uwe Kühnel, Jochen Maurer, Marc Messerschmidt, Robert Moshammer, Christian Reich, Benedikt Rudek, Robin Santra, Ilme Schlichting, Carlo Schmidt, Sebastian Schorb, Joachim Schulz, Heike Soltau, John C. H. Spence, Dmitri Starodub, Lothar Strüder, Jan Thøgersen, Marc J. J. Vrakking, Georg Weidenspointner, Thomas A. White, Cornelia Wunderer, Gerard Meijer, Joachim Ullrich, Henrik Stapelfeldt, Daniel Rolles, and Henry N. Chapman. X-ray diffraction from isolated and strongly aligned gas-phase molecules with a free-electron laser. *Phys. Rev. Lett.*, 112:083002, 2014. doi: 10.1103/PhysRevLett.112.083002. URL `https://dx.doi.org/10.1103/PhysRevLett.112.083002`.

[66] O. Stern. A new method for the measurement of the bohr magneton. *Phys. Rev.*, 51: 0852–0854, 1937.

[67] G. Scoles, editor. *Atomic and molecular beam methods*, volume 1 & 2. Oxford University Press, New York, NY, USA, 1988 & 1992.

[68] Norman F. Ramsey. *Molecular Beams.* The International Series of Monographs on Physics. Oxford University Press, London, GB, 1956. reprinted in *Oxford Classic Texts in the Physical Sciences* (2005).

[69] John B Fenn. Research in retrospect: Some biograffiti of a journeyman chemist. *Annu. Rev. Phys. Chem.*, 47:1–41, 1996. doi: 10.1146/annurev.physchem.47.1.1.

[70] Hans Pauly. *Atom, Molecule, and Cluster Beams*, volume 1 & 2 of *Springer Series on Atomic, Optical, and Plasma Physics.* Springer Verlag, 2000.

[71] U. Even. Pulsed supersonic beams from high pressure source: Simulation results and experimental measurements. *Adv. Chem.*, 2014:636042, 2014. doi: 10.1155/2014/636042.

[72] Uzi Even. The Even-Lavie valve as a source for high intensity supersonic beam. *Eur. Phys. J. Techn. Instrumen.*, 2(1):17, December 2015. doi: 10.1140/epjti/s40485-015-0027-5.

[73] U. Even, J. Jortner, D. Noy, N. Lavie, and N. Cossart-Magos. Cooling of large molecules below 1 K and He clusters formation. *J. Chem. Phys.*, 112:8068–8071, 2000. doi: 10.1063/1.481405. URL `http://dx.doi.org/10.1063/1.481405`.

[74] Matthias Hillenkamp, Sharon Keinan, and Uzi Even. Condensation limited cooling in supersonic expansions. *J. Chem. Phys.*, 118(19):8699–8705, 2003. doi: 10.1063/1.1568331. URL `http://link.aip.org/link/?JCP/118/8699/1`.

[75] Donald H Levy. The spectroscopy of very cold gases. *Science*, 214(4518):263–269, 1981.

[76] Sebastian Trippel, Yuan-Pin Chang, Stephan Stern, Terry Mullins, Lotte Holmegaard, and Jochen Küpper. Spatial separation of state- and size-selected neutral clusters. *Phys. Rev. A*, 86:033202, September 2012. doi: 10.1103/PhysRevA.86.033202. URL `http://pra.aps.org/abstract/PRA/v86/i3/e033202`.

[77] I V Hertel and W Radloff. Ultrafast dynamics in isolated molecules and molecular clusters. *Rep. Prog. Phys.*, 69(6):1897–2003, 2006. doi: 10.1088/0034-4885/69/6/r06. URL `https://iopscience.iop.org/article/10.1088/0034-4885/69/6/R06/meta`.

[78] Richard E. Smalley, Lennard Wharton, and Donald H. Levy. Molecular optical spectroscopy with supersonic beams and jets. *Acc. Chem. Res.*, 10(4):139–145, 1977. doi: 10.1021/ar50112a006. URL `https://doi.org/10.1021/ar50112a006`.

[79] Wolfgang Christen, Klaus Rademann, and Uzi Even. Supersonic beams at high particle densities: Model description beyond the ideal gas approximation. *J. Phys. Chem. A*, 114(42):11189–11201, 2010. doi: 10.1021/jp102855m.

[80] Joop J. Gilijamse, Steven Hoekstra, Sebastiaan Y. T. van de Meerakker, Gerrit C. Groenenboom, and Gerard Meijer. Near-threshold inelastic collisions using molecular beams with a tunable velocity. *Science*, 313:1617–1620, September 2006. doi: 10.1126/science.1131867.

[81] Eric R. Hudson, H. J. Lewandowski, Brian C. Sawyer, and Jun Ye. Cold molecule spectroscopy for constraining the evolution of the fine structure constant. *Phys. Rev. Lett.*, 96(14):143004, 2006. URL `http://link.aps.org/abstract/PRL/v96/e143004`.

[82] J. J. Hudson, D. M. Kara, I. J. Smallman, B. E. Sauer, M. R. Tarbutt, and E. A. Hinds. Improved measurement of the shape of the electron. *Nature*, 473(7348):493–496, may 2011. doi: 10.1038/nature10104. URL `https://doi.org/10.1038%2Fnature10104`.

[83] Lincoln D Carr, David DeMille, Roman V Krems, and Jun Ye. Cold and ultracold molecules: science, technology and applications. *New J. Phys.*, 11(5):055049, may 2009. doi: 10.1088/1367-2630/11/5/055049. URL `https://doi.org/10.1088%2F1367-2630%2F11%2F5%2F055049`.

[84] Sebastiaan Y. T. van de Meerakker, Hendrick L. Bethlem, and Gerard Meijer. Taming molecular beams. *Nat. Phys.*, 4(8):595, Aug 2008. doi: 10.1038/nphys1031. URL `http://dx.doi.org/10.1038/nphys1031`.

[85] O. G. Danylchenko, S. I. Kovalenko, and V. N. Samovarov. Experimental verification of the hagena relation for large clusters formed in a conical nozzle. *Tech. Phys. Lett.*, 34:1037–1040, 2008. doi: 10.1134/S1063785008120146. URL `https://doi.org/10.1134/S1063785008120146`.

[86] Yuan-Pin Chang, Daniel A. Horke, Sebastian Trippel, and Jochen Küpper. Spatially-controlled complex molecules and their applications. *Int. Rev. Phys. Chem.*, 34: 557–590, 2015. doi: 10.1080/0144235X.2015.1077838. URL `https://dx.doi.org/10.1080/0144235X.2015.1077838`.

[87] N. Vanhaecke, U. Meier, M. Andrist, B. H. Meier, and F. Merkt. Multistage Zeeman deceleration of hydrogen atoms. *Phys. Rev. A*, 75(3):031402(R), MAR 2007. doi: 10.1103/PhysRevA.75.031402.

[88] Edvardas Narevicius and Mark G Raizen. Toward cold chemistry with magnetically decelerated supersonic beams. *Chem. Rev.*, 112(9):4879–89, September 2012. doi: 10.1021/cr2004597. URL `http://www.ncbi.nlm.nih.gov/pubmed/22827566`.

[89] Jochen Küpper, Frank Filsinger, and Gerard Meijer. Manipulating the motion of large molecules. *Faraday Disc.*, 142:155–173, 2009. doi: 10.1039/b820045a.

[90] W. Gerlach and O. Stern. Der experimentelle Nachweis der Richtungsquantelung im Magnetfeld. *Z. Phys.*, 9:349–352, 1922. doi: 10.1007/BF01326983. URL `http://dx.doi.org/10.1007/BF01326983`.

[91] Henrik Stapelfeldt and Tamar Seideman. Colloquium: Aligning molecules with strong laser pulses. *Rev. Mod. Phys.*, 75(2):543–557, 2003. doi: 10.1103/RevModPhys.75.543. URL `http://link.aps.org/abstract/RMP/v75/p543`.

[92] J. P. Gordon, H. J. Zeiger, and C. H. Townes. The Maser—new type of microwave amplifier, frequency standard, and spectrometer. *Phys. Rev.*, 99:1264–1274, 1955. doi: 10.1103/PhysRev.99.1264.

[93] Sebastiaan Y T van de Meerakker, Hendrick L Bethlem, Nicolas Vanhaecke, and Gerard Meijer. Manipulation and control of molecular beams. *Chem. Rev.*, 112(9): 4828–4878, March 2012. doi: 10.1021/cr200349r. URL `http://pubs.acs.org/doi/abs/10.1021/cr200349r`.

[94] Melanie Schnell and Gerard Meijer. Cold molecules: Preparation, applications, and challenges. *Angew. Chem. Int. Ed.*, 48(33):6010–6031, Jan 2009. doi: 10.1002/anie.200805503. URL `http://dx.doi.org/10.1002/anie.200805503`.

[95] H. L. Bethlem, G. Berden, F. M. H. Crompvoets, R. T. Jongma, A. J. A. van Roij, and G. Meijer. Electrostatic trapping of ammonia molecules. *Nature*, 406:491–494, 2000. doi: 10.1038/35020030. URL `http://dx.doi.org/10.1038/35020030`.

[96] H. Odashima, S. Merz, K. Enomoto, M. Schnell, and G. Meijer. Microwave lens for polar molecules. *Phys. Rev. Lett.*, 104:253001, 2010. doi: 10.1103/PhysRevLett.104.253001.

[97] H. Stapelfeldt, H. Sakai, E. Constant, and P. B. Corkum. Deflection of neutral molecules using the nonresonant dipole force. *Phys. Rev. Lett.*, 79:2787–2790, 1997. URL `http://dx.doi.org/10.1103/PhysRevLett.79.2787`.

[98] Bum Suk Zhao, Hoi Sung Chung, Keunchang Cho, Sung Hyup Lee, Sungu Hwang, Jongwan Yu, Y. H Ahn, J. Y Sohn, D. S Kim, Wee Kyung Kang, and Doo Soo Chung. Molecular lens of the nonresonant dipole force. *Phys. Rev. Lett.*, 85(13):2705–2708, Sep 2000. doi: 10.1103/PhysRevLett.85.2705.

[99] R. Fulton, A. I. Bishop, and P. F. Barker. Optical Stark decelerator for molecules. *Phys. Rev. Lett.*, 93:243004, 2004. doi: 10.1103/PhysRevLett.93.243004.

[100] H. J. Loesch and A. Remscheid. Brute force in molecular reaction dynamics: A novel technique for measuring steric effects. *J. Chem. Phys.*, 93:4779, 1990. doi: 10.1063/1.458668.

[101] B. Friedrich and D. R. Herschbach. Spatial orientation of molecules in strong electric fields and evidence for pendular states. *Nature*, 353:412–414, 1991. doi: 10.1038/353412a0.

[102] Bretislav Friedrich and Dudley Herschbach. Alignment and trapping of molecules in intense laser fields. *Phys. Rev. Lett.*, 74(23):4623–4626, June 1995. doi: 10.1103/PhysRevLett.74.4623.

[103] Lotte Holmegaard, Jonas L. Hansen, Line Kalhøj, Sofie Louise Kragh, Henrik Stapelfeldt, Frank Filsinger, Jochen Küpper, Gerard Meijer, Darko Dimitrovski, Mahmoud Abu-samha, Christian P. J. Martiny, and Lars Bojer Madsen. Photoelectron angular distributions from strong-field ionization of oriented molecules. *Nat. Phys.*, 6:428, 2010. doi: 10.1038/NPHYS1666. URL `https://www.nature.com/articles/nphys1666`.

[104] Lotte Holmegaard, Jens H. Nielsen, Iftach Nevo, Henrik Stapelfeldt, Frank Filsinger, Jochen Küpper, and Gerard Meijer. Laser-induced alignment and orientation of quantum-state-selected large molecules. *Phys. Rev. Lett.*, 102:023001, 2009. doi: 10.1103/PhysRevLett.102.023001. URL `http://dx.doi.org/10.1103/PhysRevLett.102.023001`.

[105] Jens S. Kienitz, Sebastian Trippel, Terry Mullins, Karol Długołęcki, Rosario González-Férez, and Jochen Küpper. Adiabatic mixed-field orientation of ground-state-selected carbonyl sulfide molecules. *Chem. Phys. Chem.*, 17(22):3740–3746, 2016. doi: cphc.201600710R2. URL `http://dx.doi.org/10.1002/cphc.201600710`.

[106] Daniel A. Horke, Yuan-Pin Chang, Karol Długołęcki, and Jochen Küpper. *Angew. Chem.*, 126:12159–12162, 2014. doi: 10.1002/ange.201405986.

[107] Nicole Teschmit, Daniel A. Horke, and Jochen Küpper. Spatially separating the conformers of a dipeptide. *Angew. Chem. Int. Ed.*, 57(42):13775–13779, October 2018. doi: 10.1002/anie.201807646. URL `https://onlinelibrary.wiley.com/doi/abs/10.1002/anie.201807646`.

[108] Melby Johny, Jolijn Onvlee, Thomas Kierspel, Helen Bieker, Sebastian Trippel, and Jochen Küpper. Spatial separation of pyrrole and pyrrole-water clusters. *Chem. Phys. Lett.*, 721:149–152, 2019. ISSN 0009-2614. doi: 10.1016/j.cplett.2019.01.052. URL `https://doi.org/10.1016/j.cplett.2019.01.052`.

[109] Thomas Kierspel, Daniel A. Horke, Yuan-Pin Chang, and Jochen Küpper. Spatially separated polar samples of the *cis* and *trans* conformers of 3-fluorophenol. *Chem. Phys. Lett.*, 591:130–132, 2014. ISSN 0009-2614. doi: 10.1016/j.cplett.2013.11.010. URL `http://www.sciencedirect.com/science/article/pii/S0009261413014000`.

[110] Helen Bieker, Jolijn Onvlee, Melby Johny, Lanhai He, Thomas Kierspel, Sebastian Trippel, Daniel A Horke, and Jochen Küpper. Pure molecular beam of water dimer. *J. Phys. Chem. A*, 123:7486–7490, August 2019. doi: 10.1021/acs.jpca.9b06460. URL `https://doi.org/10.1021/acs.jpca.9b06460`.

[111] W. Ronald Gentry and Clayton F. Giese. High-precision skimmers for supersonic molecular beams. *Rev. Sci. Instrum.*, 46(1):104–104, 1975. doi: 10.1063/1.1134043. URL `https://doi.org/10.1063/1.1134043`.

[112] Wolfgang Demtröder. *Laser Spectroscopy 1: Basic Principles.* Springer Verlag, Berlin, 2008. ISBN 978-3-540-73418-5. doi: 10.1007/978-3-540-73418-5.

[113] Ranga Subramanian and Mark Sulkes. Production of a slit skimmer for use in cold supersonic molecular beams. *Rev. Sci. Instrum.*, 79(1):016101, January 2008. doi: 10.1063/1.2814026. URL `http://aip.scitation.org/doi/10.1063/1.2814026`.

[114] Klaus Hornberger, Stefan Gerlich, Philipp Haslinger, Stefan Nimmrichter, and Markus Arndt. Colloquium: Quantum interference of clusters and molecules. *Rev. Mod. Phys.*, 84(1):157–173, February 2012. doi: 10.1103/RevModPhys.84.157. URL `http://link.aps.org/doi/10.1103/RevModPhys.84.157`.

[115] Sebastian Trippel, Joss Wiese, Terry Mullins, and Jochen Küpper. Communication: Strong laser alignment of solvent-solute aggregates in the gas-phase. *J. Chem. Phys.*, 148(10):101103, March 2018. doi: 10.1063/1.5023645. URL `http://aip.scitation.org/doi/10.1063/1.5023645`.

[116] Linda V. Thesing, Andrey Yachmenev, Rosario González-Férez, and Jochen Küpper. Laser-induced alignment of weakly bound molecular aggregates. *Phys. Rev. A*, 98:053412, November 2018. doi: 10.1103/PhysRevA.98.053412. URL `https://journals.aps.org/pra/abstract/10.1103/PhysRevA.98.053412`.

[117] Th. Fennel, K.-H. Meiwes-Broer, J. Tiggesbäumker, P.-G. Reinhard, P. M. Dinh, and E. Suraud. Laser-driven nonlinear cluster dynamics. *Rev. Mod. Phys.*, 91(2): 1793–1842, 2010. doi: 10.1103/revmodphys.82.1793. URL `https://doi.org/10.1103/revmodphys.82.1793`.

[118] Scott G. Sayres, Matt W. Ross, and A. W. Castleman. Influence of clustering and molecular orbital shapes on the ionization enhancement in ammonia. *Phys. Chem. Chem. Phys.*, 13(26):12231, 2011. doi: 10.1039/c1cp20612e. URL `https://doi.org/10.1039/c1cp20612e`.

[119] T. Seideman, M. Y. Ivanov, and P. B. Corkum. Role of electron localization in intense-field molecular ionization. *Phys. Rev. Lett.*, 75:2819–2822, 1995. doi: 10.1103/PhysRevLett.75.2819. URL `https://link.aps.org/doi/10.1103/PhysRevLett.75.2819`.

[120] T. Zuo and A. D. Bandrauk. Charge-resonance-enhanced ionization of diatomic molecular ions by intense lasers. *Phys. Rev. A*, 52:R2511–R2514, 1995. doi: 10.1103/PhysRevA.52.R2511. URL `https://link.aps.org/doi/10.1103/PhysRevA.52.R2511`.

[121] K Codling, L J Frasinski, and P A Hatherly. On the field ionisation of diatomic molecules by intense laser fields. *J. Phys. B*, 22(12):L321–L327, 1989. doi: 10.1088/0953-4075/22/12/004. URL `https://doi.org/10.1088%2F0953-4075%2F22%2F12%2F004`.

[122] Stefan Roither, Xinhua Xie, Daniil Kartashov, Li Zhang, Markus Schöffler, Huailiang Xu, Atsushi Iwasaki, Tomoya Okino, Kaoru Yamanouchi, Andrius Baltuska, and Markus Kitzler. High energy proton ejection from hydrocarbon molecules driven by highly efficient field ionization. *Phys. Rev. Lett.*, 106(16):163001, 2011. URL `https://link.aps.org/doi/10.1103/PhysRevLett.106.163001`.

[123] E. Constant, H. Stapelfeldt, and P. B. Corkum. Observation of enhanced ionization of molecular ions in intense laser fields. *Phys. Rev. Lett.*, 76:4140–4143, 1996. doi: 10.1103/PhysRevLett.76.4140. URL `https://link.aps.org/doi/10.1103/PhysRevLett.76.4140`.

[124] J. Purnell, E.M. Snyder, S. Wei, and A.W. Castleman. Ultrafast laser-induced coulomb explosion of clusters with high charge states. *Chem. Phys. Lett.*, 229(4): 333 – 339, 1994. doi: https://doi.org/10.1016/0009-2614(94)01145-1. URL `http://www.sciencedirect.com/science/article/pii/0009261494011451`.

[125] E.M. Snyder, S. Wei, J. Purnell, S.A. Buzza, and A.W. Castleman. Femtosecond laser-induced coulomb explosion of ammonia clusters. *Chem. Phys. Lett.*, 248(1):1–7, 1996. doi: 10.1016/0009-2614(95)01278-8. URL `http://www.sciencedirect.com/science/article/pii/0009261495012788`.

[126] E. M. Snyder, S. A. Buzza, and A. W. Castleman, Jr. Intense field-matter interactions: Multiple ionization of clusters. *Phys. Rev. Lett.*, 77:3347–3350, 1996. doi: 10.1103/PhysRevLett.77.3347. URL `https://link.aps.org/doi/10.1103/PhysRevLett.77.3347`.

[127] D. A. Card, E. S. Wisniewski, D. E. Folmer, and A. W. Castleman. Dynamics of coulomb explosion and kinetic energy release in clusters of heterocyclic compounds. *J. Chem. Phys.*, 116:3554–3567, 2002. doi: 10.1063/1.1446849. URL `https://doi.org/10.1063/1.1446849`.

[128] C. Rose-Petruck, K. J. Schafer, K. R. Wilson, and C. P. J. Barty. Ultrafast electron dynamics and inner-shell ionization in laser driven clusters. *Phys. Rev. A*, 55:1182–1190, 1997. doi: 10.1103/PhysRevA.55.1182. URL `https://link.aps.org/doi/10.1103/PhysRevA.55.1182`.

[129] Matt W. Ross, Cuneyt Berkdemir, and A. W. Castleman. Strong-field ionization and coulomb explosion of chlorine weakly bound to small water clusters. *J. Phys. Chem. A*, 116:8530–8538, 2012. doi: 10.1021/jp3036617. URL `https://doi.org/10.1021/jp3036617`.

[130] S. Zamith, T. Martchenko, Y. Ni, S. A. Aseyev, H. G Muller, and M. J. J. Vrakking. Control of the production of highly charged ions in femtosecond-laser cluster fragmentation. *Phys. Rev. A*, 70:011201, 2004. doi: 10.1103/physreva.70.011201. URL `https://doi.org/10.1103/physreva.70.011201`.

[131] Yunpei Deng, Zhinan Zeng, Pavel Komm, Yinhui Zheng, Wolfram Helml, Xinhua Xie, , Zoltan Filus, Mathieu Dumergue, Roland Flender, Máté Kurucz, Ludovit Haizer, Balint Kiss, Subhendu Kahaly, Ruxin Li, and Gilad Marcus. Laser-induced inner-shell excitations through direct electron re-collision versus indirect collision. *Opt. Exp.*, 28:23251, 2020. doi: 10.1364/oe.395927. URL `https://doi.org/10.1364/oe.395927`.

[132] Z. Vager, R. Naaman, and E. P. Kanter. Coulomb explosion imaging of small molecules. *Science*, 244(4903):426–431, 1989. doi: 10.1126/science.244.4903.426. URL `http://www.sciencemag.org/cgi/doi/10.1126/science.244.4903.426`.

[133] Z Vager, T Graber, E P Kanter, and D ZAJFMAN. Direct observation of nuclear rearrangement in molecules. *Phys. Rev. Lett.*, 70(23):3549–3552, jun 1993. doi: 10.1103/PhysRevLett.70.3549. URL `https://link.aps.org/doi/10.1103/PhysRevLett.70.3549`.

[134] Henrik Stapelfeldt, E Constant, and P B Corkum. Wave-packet structure and dynamics measured by coulomb explosion. *Phys. Rev. Lett.*, 74(19):3780–3783, 1995. doi: 10.1103/PhysRevA.58.426.

[135] Henrik Stapelfeldt, Eric Constant, Hirofumi Sakai, and Paul B. Corkum. Time-resolved coulomb explosion imaging: A method to measure structure and dynamics of molecular nuclear wave packets. *Phys. Rev. A*, 58:426–433, 1998. doi: 10.1103/PhysRevA.58.426. URL `https://doi.org/10.1103/PhysRevA.58.426`.

[136] W. C. Röntgen. Über eine neue Art von Strahlen. *Annalen der Physik*, 300(1):12–17, 1898. ISSN 1521-3889. doi: 10.1002/andp.18983000103. URL `http://dx.doi.org/10.1002/andp.18983000103`.

[137] David Attwood. *Soft x-rays and extreme ultraviolet radiation: principles and applications.* Cambridge University Press, University of California, Berkeley, 2000. ISBN 0521652146.

[138] Jens Als-Nielsen and Des McMorrow. *Elements of Modern X-ray Physics.* John Wiley & Sons, Chichester, West Sussex, United Kingdom, 2001. ISBN 978-0-471-49858-2.

[139] Robin Santra. Concepts in x-ray physics. *J. Phys. B*, 42(2):023001, January 2009. doi: 10.1088/0953-4075/42/2/023001. URL `http://iopscience.iop.org/article/10.1088/0953-4075/42/2/023001`.

[140] J. D. Watson and F. H. C. Crick. Molecular structure of nucleic acids: A structure for deoxyribose nucleic acid. *Nature*, 171(4356):737–738, 1953. doi: 10.1038/171737a0. URL `http://dx.doi.org/10.1038/171737a0`.

[141] B Erk, D Rolles, L Foucar, B Rudek, S W Epp, M Cryle, C Bostedt, S Schorb, J Bozek, A Rouzee, A Hundertmark, T Marchenko, M Simon, F Filsinger, L Christensen, S De, S Trippel, Jochen Küpper, Henrik Stapelfeldt, S Wada, K Ueda, M Swiggers, M Messerschmidt, C D Schroter, R Moshammer, I Schlichting, J Ullrich, and A Rudenko. Ultrafast charge rearrangement and nuclear dynamics upon inner-shell multiple ionization of small polyatomic molecules. *Phys. Rev. Lett.*, 110(5):053003, January 2013. doi: 10.1103/PhysRevLett.110.053003. URL `http://prl.aps.org/abstract/PRL/v110/i5/e053003`.

[142] Benjamin Erk, Rebecca Boll, Sebastian Trippel, Denis Anielski, Lutz Foucar, Benedikt Rudek, Sascha W Epp, Ryan Coffee, Sebastian Carron, Sebastian Schorb, Ken R Ferguson, Michele Swiggers, John D Bozek, Marc Simon, Tatiana Marchenko, Jochen

Küpper, Ilme Schlichting, Joachim Ullrich, Christoph Bostedt, Daniel Rolles, and Artem Rudenko. Imaging charge transfer in iodomethane upon x-ray photoabsorption. *Science*, 345(6194):288–291, July 2014. doi: 10.1126/science.1253607.

[143] T. Jahnke, H. Sann, T. Havermeier, K. Kreidi, C. Stuck, M. Meckel, M. Schöffler, N. Neumann, R. Wallauer, S. Voss, A. Czasch, O. Jagutzki, A. Malakzadeh, F. Afaneh, Th. Weber, H. Schmidt-Böcking, and R. Dörner. Ultrafast energy transfer between water molecules. *Nat. Phys.*, 6(2):139–142, January 2010. doi: 10.1038/nphys1498. URL `http://www.nature.com/doifinder/10.1038/nphys1498`.

[144] B K McFarland, J P Farrell, S Miyabe, F Tarantelli, A Aguilar, N Berrah, C Bostedt, J D Bozek, P H Bucksbaum, J C Castagna, R N Coffee, J P Cryan, L Fang, R Feifel, K J Gaffney, J M Glownia, T J Martinez, M Mucke, B Murphy, A Natan, T Osipov, V S Petrovic, S Schorb, Th Schultz, L S Spector, M Swiggers, I Tenney, S Wang, J L White, W White, and M Gühr. Ultrafast x-ray auger probing of photoexcited molecular dynamics. *Nat. Commun.*, 5:4235, 2014. doi: 10.1038/ncomms5235. URL `http://www.nature.com/doifinder/10.1038/ncomms5235`.

[145] Oliver Gessner and Markus Gühr. Monitoring ultrafast chemical dynamics by time-domain x-ray photo- and auger-electron spectroscopy. *Acc. Chem. Res.*, 49(1):138–145, jan 2016. doi: 10.1021/acs.accounts.5b00361. URL `http://pubs.acs.org/doi/abs/10.1021/acs.accounts.5b00361`.

[146] T Jahnke. Interatomic and intermolecular Coulombic decay: the coming of age story. *J. Phys. B*, 48(8):082001, 2015. doi: 10.1088/0953-4075/48/8/082001. URL `http://doi.org/10.1088/0953-4075/48/8/082001`.

[147] L S Cederbaum, J Zobeley, and F Tarantelli. Giant intermolecular decay and fragmentation of clusters. *Phys. Rev. Lett.*, 79(24):4778–4781, December 1997. doi: 10.1103/PhysRevLett.79.4778. URL `https://doi.org/10.1103/PhysRevLett.79.4778`.

[148] Melanie Mucke, Markus Braune, Silko Barth, Marko Förstel, Toralf Lischke, Volker Ulrich, Tiberiu Arion, Uwe Becker, Alex Bradshaw, and Uwe Hergenhahn. A hitherto unrecognized source of low-energy electrons in water. *Nat. Phys.*, 6:143–146, 2010. doi: 10.1038/nphys1500. URL `https://www.nature.com/articles/nphys1500`.

[149] X. Ren, E. Wang, A. D. Skitnevskaya, A. B. Trofimov, G. Kirill, and A. Dorn. Experimental evidence for ultrafast intermolecular relaxation processes in hydrated biomolecules. *Nat. Phys.*, 79:1745, 2018. doi: 10.1038/s41567-018-0214-9. URL `https://doi.org/10.1038/s41567-018-0214-9`.

[150] Petr Slavíček, Bernd Winter, Lorenz S. Cederbaum, and Nikolai V. Kryzhevoi. Proton-transfer mediated enhancement of nonlocal electronic relaxation processes in X-ray

irradiated liquid water. *J. Am. Chem. Soc.*, 136(52):18170–18176, June 2014. doi: 10.1021/ja5117588. URL `https://doi.org/10.1021/ja5117588`.

[151] Clemens Richter, Daniel Hollas, Clara Magdalena Saak, Marko Förstel, Tsveta Miteva, Melanie Mucke, Olle Björneholm, Nicolas Sisourat, Petr Slavicek, and Uwe Hergenhahn. Competition between proton transfer and intermolecular Coulombic decay in water. *Nat. Commun.*, 9:4988, 2018. doi: 10.1038/s41467-018-07501-6. URL `https://www.nature.com/articles/s41467-018-07501-6`.

[152] Stephan Thürmer, Milan Ončák, Niklas Ottosson, Robert Seidel, Uwe Hergenhahn, Stephen E. Bradforth, Petr Slavíček, and Bernd Winter. On the nature and origin of dicationic, charge-separated species formed in liquid water on X-ray irradiation. *Nat. Chem.*, 5:590–596, 2013. doi: 10.1038/nchem.1680. URL `https://doi.org/10.1038/nchem.1680`.

[153] A Sugishima, K Nagaya, H Iwayama, M Yao, J Adachi, Y Kimura, M Yamazaki, and A Yagishita. Dissociation dynamics of c_6h_6 and c_6h_5f molecules following carbon 1*s* and fluorine 1*s* photoionization studied by three-dimensional momentum imaging method. *J. Chem. Phys.*, 131(11):114309, September 2009. doi: 10.1063/1.3224117. URL `http://scitation.aip.org/content/aip/journal/jcp/131/11/10.1063/1.3224117`.

[154] Rebecca Boll, Benjamin Erk, Ryan Coffee, Sebastian Trippel, Thomas Kierspel, Cédric Bomme, John D. Bozek, Mitchell Burkett, Sebastian Carron, Ken R. Ferguson, Lutz Foucar, Jochen Küpper, Tatiana Marchenko, Catalin Miron, Minna Patanen, Timur Osipov, Sebastian Schorb, Marc Simon, Michelle Swiggers, Simone Techert, Kiyoshi Ueda, Christoph Bostedt, Daniel Rolles, and Artem Rudenko. Charge transfer in dissociating iodomethane and fluoromethane molecules ionized by intense femtosecond x-ray pulses. *Struct. Dyn.*, 3:043207, 2016. doi: 10.1063/1.4944344. URL `https://doi.org/10.1063/1.4944344`.

[155] C Bomme, R Guillemin, T Marin, L Journel, T Marchenko, D Dowek, N Trcera, B Pilette, A Avila, H Ringuenet, R K Kushawaha, and M Simon. Double momentum spectrometer for ion-electron vector correlations in dissociative photoionization. *Rev. Sci. Instrum.*, 84(10):103104, oct 2013. doi: 10.1063/1.4824194. URL `http://scitation.aip.org/content/aip/journal/rsi/84/10/10.1063/1.4824194`.

[156] D T Ha, M A Huels, M Huttula, S Urpelainen, and E Kukk. Experimental and *ab initio* study of the photofragmentation of DNA and RNA sugars. *Phys. Rev. A*, 84 (3):033419, sep 2011. doi: 10.1103/PhysRevA.84.033419. URL `https://doi.org/10.1103/PhysRevA.84.033419`.

[157] Helena Levola, Eero Itala, Kim Schlesier, Kuno Kooser, Sanna Laine, Joakim Laksman, Dang Trinh Ha, Elisabeth Rachlew, Marta Tarkanovskaja, Katrin Tanzer, and Edwin Kukk. Ionization-site effects on the photofragmentation of chloro- and bromoacetic acid molecules. *Phys. Rev. A*, 92(6):063409, December 2015. doi: 10.1103/PhysRevA.92.063409. URL `http://link.aps.org/doi/10.1103/PhysRevA.92.063409`.

[158] Dang Trinh Ha, Y Wang, M Alcami, E Itaelae, K Kooser, S Urpeainen, M A Huels, E Kukk, and F Martín. Fragmentation dynamics of doubly charged methionine phase. *J. Phys. Chem. A*, 118(8):1374–1383, 2014. doi: 10.1021/jp4113238. URL `http://eutils.ncbi.nlm.nih.gov/entrez/eutils/elink.fcgi?dbfrom=pubmed&id=24517120&retmode=ref&cmd=prlinks`.

[159] E Kukk, D T Ha, Y Wang, D G Piekarski, S Diaz-Tendero, K Kooser, E Itala, H Levola, M Alcami, E Rachlew, and F Martín. Internal energy dependence in x-ray-induced molecular fragmentation: An experimental and theoretical study of thiophene. *Phys. Rev. A*, 91(4):043417, April 2015. doi: 10.1103/PhysRevA.91.043417. URL `http://link.aps.org/doi/10.1103/PhysRevA.91.043417`.

[160] O. Geßner, A. M. D. Lee, J. P. Shaffer, H. Reisler, S. V. Levchenko, A. I. Krylov, Jonathan G. Underwood, H. Shi, A. L. L. East, D. M. Wardlaw, E. t. H. Chrysostom, C. C. Hayden, and Albert Stolow. Femtosecond multidimensional imaging of a molecular dissociation. *Science*, 311(5758):219–222, 2006. doi: 10.1126/science.1120779.

[161] Renaud Guillemin, Cédric Bomme, Thierry Marin, Loic Journel, Tatiana Marchenko, Rajesh K Kushawaha, Nicolas Trcera, Maria Novella Piancastelli, and Marc Simon. Complex decay patterns in atomic core photoionization disentangled by ion-recoil measurements. *Phys. Rev. A*, 84(6):063425, December 2011. doi: 10.1103/PhysRevA.84.063425. URL `http://link.aps.org/doi/10.1103/PhysRevA.84.063425`.

[162] Thomas Kierspel, Cédric Bomme, Michele Di Fraia, Joss Wiese, Denis Anielski, Sadia Bari, Rebecca Boll, Benjamin Erk, Jens S. Kienitz, Nele L. M. Müller, Daniel Rolles, Jens Viefhaus, Sebastian Trippel, and Jochen Küpper. Photophysics of indole upon x-ray absorption. *Phys. Chem. Chem. Phys.*, 20:20205, 2018. doi: 10.1039/C8CP00936H. URL `https://dx.doi.org/10.1039/C8CP00936H`.

[163] R Guillemin, P Decleva, M Stener, C Bomme, T Marin, L Journel, T Marchenko, R K Kushawaha, K Jänkälä, N Trcera, K P Bowen, D W Lindle, M N Piancastelli, and M Simon. Selecting core-hole localization or delocalization in cs_2 by photofragmentation dynamics. *Nat. Commun.*, 6:6166, 2015. doi: 10.1038/ncomms7166. URL `http://www.nature.com/doifinder/10.1038/ncomms7166`.

[164] Daniele Toffoli, Robert R Lucchese, M Lebech, J C Houver, and D Dowek. Molecular frame and recoil frame photoelectron angular distributions from dissociative

photoionization of no2. *J. Chem. Phys.*, 126(5):054307, feb 2007. doi: 10.1063/1.2432124. URL `http://scitation.aip.org/content/aip/journal/jcp/126/5/10.1063/1.2432124`.

[165] Wolfgang 1931 Demtröder. *Atoms, Molecules and Photons An Introduction to Atomic-, Molecular- and Quantum Physics.* Graduate Texts in Physics: SpringerLink: Bücher. Springer, third edition edition, 2018. doi: 10.1007/978-3-662-55523-1.

[166] Richard N. Zare. *Angular Momentum.* John Wiley & Sons, New York, NY, USA, 1988. ISBN 0471858927.

[167] W. Gordy and R. L. Cook. *Microwave Molecular Spectra.* John Wiley & Sons, New York, NY, USA, 3 edition, 1984.

[168] C. D. Lin, Anh-Thu Le, Cheng Jin, and Hui Wei. *Attosecond and Strong-Field Physics: Principles and Applications.* Cambridge University Press, 2018. doi: 10.1017/9781108181839.

[169] S. Carles, F. Lecomte, J. P. Schermann, and C. Desfrançois. Gas-phase experimental and theoretical studies of adenine, imidazole, pyrrole, and water non-covalent complexes. *J. Phys. Chem. A*, 104:10662–10668, 2000. doi: 10.1021/jp002157j. URL `https://doi.org/10.1021/jp002157j`.

[170] B. L. Blaney and G. F Ewing. Van der waals molecules. *Annu. Rev. Phys. Chem.*, 27:553–586, 1976. doi: 10.1146/annurev.pc.27.100176.003005. URL `https://www.annualreviews.org/doi/pdf/10.1146/annurev.pc.27.100176.003005`.

[171] O. F. Hagena and W. Obert. Cluster formation in expanding supersonic jets: Effect of pressure, temperature, nozzle size, and test gas. *J. Chem. Phys.*, 56(5):1793–1802, 1972. doi: 10.1063/1.1677455. URL `http://link.aip.org/link/?JCP/56/1793/1`.

[172] C. Bobbert, S. Schutte, C. Steinbach, and U. Buck. Fragmentation and reliable size distributions of large ammonia and water clusters. *European Phys. J. D*, 19(2):183–192, 2002.

[173] I. Pócsik. Lognormal distribution as the natural statistics of cluster systems. *Z. Phys. D*, 20:395–397, 1991. doi: 10.1007/BF01544020. URL `https://doi.org/10.1007/BF01544020`.

[174] Frank Filsinger, Jochen Küpper, Gerard Meijer, Jonas L. Hansen, Jochen Maurer, Jens H. Nielsen, Lotte Holmegaard, and Henrik Stapelfeldt. Pure samples of individual conformers: The separation of stereo-isomers of complex molecules using electric fields. *Angew. Chem. Int. Ed.*, 48:6900–6902, 2009. doi: 10.1002/anie.200902650. URL `http://onlinelibrary.wiley.com/doi/10.1002/anie.200902650/abstract`.

[175] J. Stark and G. Wendt. Beobachtungen über den effekt des elektrischen feldes auf spektrallinien. ii. längseffekt. *Ann. Phys.*, 348(7):983–990, 1914. ISSN 1521-3889. doi: 10.1002/andp.19143480703. URL `http://dx.doi.org/10.1002/andp.19143480703`.

[176] E. Schrödinger. An undulatory theory of the mechanics of atoms and molecules. *Phys. Rev.*, 28(6):1049–1070, December 1926. doi: 10.1103/PhysRev.28.1049.

[177] M. Born and R. Oppenheimer. Zur Quantentheorie der Molekeln. *Ann. Physik*, 84: 457–484, 1927. doi: 10.1002/andp.19273892002.

[178] C. Eckart. Some studies concerning rotating axes and polyatomic molecules. *Phys. Rev.*, 47:552, 1935. doi: 10.1103/PhysRev.47.552.

[179] Y.-P. Chang, F. Filsinger, B. Sartakov, and J. Küpper. CMIstark: Python package for the Stark-effect calculation and symmetry classification of linear, symmetric and asymmetric top wavefunctions in dc electric fields. *Comp. Phys. Comm.*, 185:339–349, 2014. doi: 10.1016/j.cpc.2013.09.001. URL `http://www.sciencedirect.com/science/article/pii/S0010465513003019`. Current version available from GitHub.

[180] M Abd El Rahim, R Antoine, M Broyer, D Rayane, and Ph Dugourd. Asymmetric top rotors in electric fields: influence of chaos and collisions in molecular beam deflection experiments. *J. Phys. Chem. A*, 109(38):8507–8514, September 2005. doi: 10.1021/jp053127p. URL `http://www.ncbi.nlm.nih.gov/pubmed/16834247`.

[181] D. R. Borst, T. M. Korter, and D. W. Pratt. On the additivity of bond dipole moments. Stark effect studies of the rotationally resolved electronic spectra of aniline, benzonitrile, and aminobenzonitrile. *Chem. Phys. Lett.*, 350:485–490, 2001. doi: 10.1016/S0009-2614(01)01344-6. URL `http://dx.doi.org/10.1016/S0009-2614(01)01344-6`.

[182] H Kallmann and F Reiche. Über den Durchgang bewegter Moleküle durch inhomogene Kraftfelder. *Z. Phys.*, 6:352–375, January 1921. doi: 10.1007/BF01327996. URL `http://dx.doi.org/10.1007/BF01327996`.

[183] Jens S. Kienitz, Karol Długołęcki, Sebastian Trippel, and Jochen Küpper. Improved spatial separation of neutral molecules. *J. Chem. Phys.*, 147(2):024304, 2017. doi: 10.1063/1.4991479. URL `https://doi.org/10.1063/1.4991479`.

[184] Jens S. Kienitz. *Orientation of state selected OCS molecules in mixed strong dc and laser fields.* Dissertation, Universität Hamburg, Hamburg, Germany, 2016.

[185] Daniel A. Horke, Yuan-Pin Chang, Karol Długołęcki, and Jochen Küpper. Separating para and ortho water. *Angew. Chem. Int. Ed.*, 53:11965–11968, 2014. doi: 10.1002/anie.

201405986. URL http://onlinelibrary.wiley.com/doi/10.1002/anie.201405986/abstract.

[186] Comsol. Multiphysics 5, 2015. http://www.comsol.com/release/5.0.

[187] P. Lambropoulos. Topics on multiphoton processes in atoms. volume 12 of *Advances in Atomic and Molecular Physics*, pages 87 – 164. Adv. Phys., 1976. doi: https://doi.org/10.1016/S0065-2199(08)60043-3. URL http://www.sciencedirect.com/science/article/pii/S0065219908600433.

[188] Misha Yu Ivanov, Michael Spanner, and Olga Smirnova. Anatomy of strong field ionization. *J. Mod. Opt.*, 52(2-3):165–184, 2005. doi: 10.1080/09500340412331301470. URL https://doi.org/10.1080/09500340412331301470.

[189] P. B. Corkum. Plasma perspective on strong-field multiphoton ionization. *Phys. Rev. Lett.*, 71:1994–1997, 1993. doi: 10.1103/PhysRevLett.71.1994. URL https://journals.aps.org/prl/abstract/10.1103/PhysRevLett.71.1994.

[190] C. D. Lin, Anh-Thu Le, Cheng Jin, and Hui Wei. *Attosecond and Strong-Field Physics: Principles and Applications*. Cambridge University Press, 2018. doi: 10.1017/9781108181839.010.

[191] W. Becker, F. Grasbon, R. Kopold, D. B. Milošević, G. G. Paulus, and H. Walther. Above-threshold ionization: From classical features to quantum effects. *Adv. Atom. Mol. Opt. Phys.*, 48:35–98, 2002. doi: 10.1016/S1049-250X(02)80006-4. URL http://adsabs.harvard.edu/abs/2002AAMOP..48...35B.

[192] Christer Z. Bisgaard and Lars Bojer Madsen. Tunneling ionization of atoms. *Am. J. Phys.*, 72(2):249–254, 2004. doi: 10.1119/1.1603274. URL https://doi.org/10.1119/1.1603274.

[193] L.V. Keldysh. Ionization in the field of a strong electromagnetic wave. *J. Exp. Theor. Phys.*, 20(5):1307–1314, 1965. URL http://www.jetp.ac.ru/cgi-bin/dn/e_020_05_1307.pdf.

[194] S V Popruzhenko. Keldysh theory of strong field ionization: history, applications, difficulties and perspectives. *J. Phys. B*, 47(20):204001, 2014. doi: 10.1088/0953-4075/47/20/204001. URL http://stacks.iop.org/0953-4075/47/i=20/a=204001.

[195] M. V. Ammosov, N. B. Delone, and V. P. Krainov. Tunnel ionization of complex atoms and of atomic ions in an alternating electromagnetic field. *Soviet Physics - JETP*, 64(6):1191–1194, 1986. URL http://www.jetp.ac.ru/cgi-bin/e/index/e/64/6/p1191?a=list.

[196] F H M Faisal. Multiple absorption of laser photons by atoms. *J. Phys. B*, 6(4):L89, 1973. doi: 10.1088/0953-4075/49/22/220501. URL http://stacks.iop.org/0022-3700/6/i=4/a=011.

[197] Howard R. Reiss. Effect of an intense electromagnetic field on a weakly bound system. *Phys. Rev. A*, 22:1786–1813, Nov 1980. doi: 10.1103/PhysRevA.22.1786. URL `https://link.aps.org/doi/10.1103/PhysRevA.22.1786`.

[198] Elettra Web Page, 2017. URL `https://vuo.elettra.eu/services/elements/WebElements.html`. Atomic Calculation of Photoionization Cross-Sections and Asymmetry Parameters.

[199] A. Thompson, I. Lindau, D. Attwood, Y. Liu, E. Gullikson, P. Pianetta, M. Howells, A. Robinson, K.-J. Kim, J. Scofield, J. Kirz, J. Underwood, J. Kortright, G. Williams, and H. Winick. *X-Ray Data Booklet.* Center for X-Ray Optics and Advanced Light Source, Lawrence Berkeley National Laboratory, Berkeley, CA, 2009. URL `http://xdb.lbl.gov/`.

[200] Svante Svensson, Bengt Eriksson, Nils Mårtensson, Göran Wendin, and Ulrik Gelius. Electron shake-up and correlation satellites and continuum shake-off distributions in x-ray photoelectron spectra of the rare gas atoms. *J. Electron. Spectrosc. Relat. Phenom.*, 47:327–384, January 1988. doi: 10.1016/0368-2048(88)85020-5. URL `https://doi.org/10.1016/0368-2048(88)85020-5`.

[201] Burhop. *The Auger Effect and Other Radiationless Transitions.* Cambridge University Press, 1952. ISBN 9781107641105.

[202] J Zobeley, R Santra, and L S Cederbaum. Electronic decay in weakly bound heteroclusters: Energy transfer versus electron transfer. *J. Chem. Phys.*, 115(11):5076–5088, 2001. doi: 10.1063/1.1395555. URL `https://doi.org/10.1063/1.1395555`.

[203] André T. J. B. Eppink and David H. Parker. Velocity map imaging of ions and electrons using electrostatic lenses: Application in photoelectron and photofragment ion imaging of molecular oxygen. *Rev. Sci. Instrum.*, 68(9):3477–3484, 1997. doi: 10.1063/1.1148310. URL `http://link.aip.org/link/?RSI/68/3477/1`.

[204] Cameron J. Dasch. One-dimensional tomography: a comparison of Abel, onion-peeling, and filtered backprojection methods. *Applied Optics*, 31(8):1146, 1992. ISSN 0003-6935. doi: 10.1364/AO.31.001146. URL `https://www.osapublishing.org/abstract.cfm?URI=ao-31-8-1146`.

[205] I. Ali, R. Dörner, O. Jagutzki, S. Nüttgens, V. Mergel, L. Spielberger, Kh. Khayyat, T. Vogt, H. Bräuning, K. Ullmann, R. Moshammer, J. Ullrich, S. Hagmann, K.-O. Groeneveld, C.L. Cocke, and H. Schmidt-Böcking. Multi-hit detector system for complete momentum balance in spectroscopy in molecular fragmentation processes. *Nucl. Instrum. Meth. B*, 149(4):490–500, 1999. ISSN 0168-583X. doi: 10.1016/S0168-583X(98)00916-1. URL `http://dx.doi.org/10.1016/S0168-583X(98)00916-1`.

[206] Arthur Zhao, Martin van Beuzekom, Bram Bouwens, Dmitry Byelov, Irakli Chakaberia, Chuan Cheng, Erik Maddox, Andrei Nomerotski, Peter Svihra, Jan Visser, Vaclav Vrba, and Thomas Weinacht. Coincidence velocity map imaging using Tpx3Cam, a time stamping optical camera with 1.5 ns timing resolution. *Rev. Sci. Instrum.*, 88 (11):113104, 2017. doi: 10.1063/1.4996888. URL `https://doi.org/10.1063/1.4996888`.

[207] Ahmed Al-Refaie, Melby Johny, Jonathan Correa, David Pennicard, Peter Svihra, Andrei Nomerotski, Sebastian Trippel, and Jochen Küpper. PymePix: A python library for SPIDR readout of Timepix3. *J. Instrum.*, 14(10):P10003, 2019. doi: 10.1088/1748-0221/14/10/P10003. URL `https://iopscience.iop.org/article/10.1088/1748-0221/14/10/P10003/meta`.

[208] Craig S. Slater, Sophie Blake, Mark Brouard, Alexandra Lauer, Claire Vallance, C. Sean Bohun, Lauge Christensen, Jens H. Nielsen, Mikael P. Johansson, and Henrik Stapelfeldt. Coulomb-explosion imaging using a pixel-imaging mass-spectrometry camera. *Phys. Rev. A*, 91:053424, May 2015. doi: 10.1103/PhysRevA.91.053424. URL `https://link.aps.org/doi/10.1103/PhysRevA.91.053424`.

[209] A Nomerotski, M Brouard, E Campbell, A Clark, J Crooks, J Fopma, J J John, A J Johnsen, C Slater, R Turchetta, C Vallance, E Wilman, and W H Yuen. Pixel imaging mass spectrometry with fast and intelligent pixel detectors. *J. Instrum.*, 5 (7):C07007, July 2010. doi: 10.1088/1748-0221/5/07/C07007. URL `https://doi.org/10.1088/1748-0221/5/07/C07007`.

[210] J H D Eland. The dynamics of three-body dissociations of dications studied by the triple coincidence technique PEPIPICO. *Mol. Phys.*, 61(3):725–745, June 1987. doi: 10.1080/00268978700101421. URL `http://www.tandfonline.com/doi/abs/10.1080/00268978700101421`.

[211] Leszek J Frasinski. Covariance mapping techniques. *J. Phys. B*, 49(15):152004, 2016. doi: 10.1088/0953-4075/49/15/152004. URL `https://doi.org/10.1088%2F0953-4075%2F49%2F15%2F152004`.

[212] L J Frasinski, K Codling, and P A Hatherly. Covariance mapping: a correlation method applied to multiphoton multiple ionization. *Science*, 246(4933):1029–1031, November 1989. doi: 10.1126/science.246.4933.1029. URL `http://www.sciencemag.org/cgi/doi/10.1126/science.246.4933.1029`.

[213] James D. Pickering, Kasra Amini, Mark Brouard, Michael Burt, Ian J. Bush, Lauge Christensen, Alexandra Lauer, Jens H. Nielsen, Craig S. Slater, and Henrik Stapelfeldt. Communication: Three-fold covariance imaging of laser-induced coulomb explosions. *J. Chem. Phys.*, 144:161105, 2016. doi: 10.1063/1.4947551. URL `https://doi.org/10.1063/1.4947551`.

[214] Frank Filsinger, Jochen Küpper, Gerard Meijer, Lotte Holmegaard, Jens H. Nielsen, Iftach Nevo, Jonas L. Hansen, and Henrik Stapelfeldt. Quantum-state selection, alignment, and orientation of large molecules using static electric and laser fields. *J. Chem. Phys.*, 131:064309, 2009. doi: 10.1063/1.3194287. URL `http://scitation.aip.org/content/aip/journal/jcp/131/6/10.1063/1.3194287`.

[215] Sarah White, Jason W. Szewczyk, James M. Turner, Eldon E. Baird, and Peter B. Dervan. Recognition of the four Watson−Crick base pairs in the DNA minor groove by synthetic ligands. *Nature*, 391:468–471, 1998. doi: 10.1038/35106. URL `http://dx.doi.org/10.1038/35106`.

[216] Yung-Sheng Yen, Ying-Chan Hsu, Jiann T. Lin, Che-Wei Chang, Chao-Ping Hsu, and Da-Jong Yin. Pyrrole-based organic dyes for dye-sensitized solar cells. *J. Phys. Chem. C*, 112(32):12557–12567, 2008. doi: 10.1021/jp801036s. URL `https://doi.org/10.1021/jp801036s`.

[217] Feng Tan, Longchao Cong, Xiaona Li, Qian Zhao, Hongxia Zhao, Xie Quan, and Jingwen Chen. An electrochemical sensor based on molecularly imprinted polypyrrole/graphene quantum dots composite for detection of bisphenol A in water samples. *Sens. Actuator B Chem.*, 233:599–606, October 2016. doi: 10.1016/j.snb.2016.04.146. URL `http://linkinghub.elsevier.com/retrieve/pii/S0925400516306281`.

[218] H Lippert, H.-H Ritze, I V Hertel, and W W Radloff. Femtosecond time-resolved hydrogen-atom elimination from photoexcited pyrrole molecules. *Chem. Phys. Lett.*, 5:1423–1427, 2004. doi: 10.1002/cphc.200400079. URL `https://doi.org/10.1002/cphc.200400079`.

[219] Irmgard Frank and Konstantina Damianos. Excited state dynamics in pyrrole-water clusters: First principles simulation. *Chem. Phys.*, 343:347–352, 2008. doi: 10.1016/j.chemphys.2007.08.029. URL `https://doi.org/10.1016/j.chemphys.2007.08.029`.

[220] Andrzej L Sobolewski and Wolfgang Domcke. Photoinduced charge separation in indole–water clusters. *Chem. Phys. Lett.*, 329(1-2):130–137, October 2000. doi: 10.1016/S0009-2614(00)00983-0. URL `http://linkinghub.elsevier.com/retrieve/pii/S0009261400009830`.

[221] Thomas Kierspel. *Imaging structure and dynamics using controlled molecules.* Dissertation, Universität Hamburg, Hamburg, Germany, 2016.

[222] Gareth M. Roberts, Craig A. Williams, Hui Yu, Adam S. Chatterley, Jamie D. Young, Susanne Ullrich, and Vasilios G. Stavros. Probing ultrafast dynamics in photoexcited

pyrrole: timescales for $^1\pi\sigma^*$ mediated H-atom elimination. *Faraday Disc.*, 163:95–115, 2013. doi: 10.1039/c2fd20140b. URL `http://pubs.rsc.org/en/content/articlepdf/2013/fd/c2fd20140b`.

[223] Oliver M. Kirkby, Michael A. Parkes, Simon P. Neville, Graham A. Worth, and Helen H. Fielding. Non-radiative relaxation dynamics of pyrrole following excitation in the range 249.5–200 nm. *Chem. Phys. Lett.*, 683:179–185, 2017. doi: 10.1016/j.cplett.2017.04.035. URL `https://doi.org/10.1016/j.cplett.2017.04.035`.

[224] Sebastian Trippel, Melby Johny, Thomas Kierspel, Jolijn Onvlee, Helen Bieker, Hong Ye, Terry Mullins, Lars Gumprecht, Karol Długołęcki, and Jochen Küpper. Knife edge skimming for improved separation of molecular species by the deflector. *Rev. Sci. Instrum.*, 89:096110, September 2018. doi: 10.1063/1.5026145. URL `https://doi.org/10.1063/1.5026145`.

[225] Use Nygaard, J.Tormod Nielsen, Jørgen Kirchheiner, Gudrun Maltesen, Chang S, J. Rastrup-Andersen, and G.Ole Sørensen. Microwave spectra of isotopic pyrroles: Molecular structure, dipole moment and ^{14}N quadrupole coupling constants of pyrrole. *J. Mol. Struct.*, 3(6):491–506, 1969. doi: 10.1016/0022-2860(69)80031-1. URL `https://doi.org/10.1016/0022-2860(69)80031-1`.

[226] Frank Filsinger, Undine Erlekam, Gert von Helden, Jochen Küpper, and Gerard Meijer. Selector for structural isomers of neutral molecules. *Phys. Rev. Lett.*, 100: 133003, 2008. doi: 10.1103/PhysRevLett.100.133003. URL `http://dx.doi.org/10.1103/PhysRevLett.100.133003`.

[227] Jens H. Nielsen, Paw Simesen, Christer Z. Bisgaard, Henrik Stapelfeldt, Frank Filsinger, Bretislav Friedrich, Gerard Meijer, and Jochen Küpper. Stark-selected beam of ground-state OCS molecules characterized by revivals of impulsive alignment. *Phys. Chem. Chem. Phys.*, 13:18971–18975, 2011. doi: 10.1039/c1cp21143a. URL `https://dx.doi.org/10.1039/c1cp21143a`.

[228] Cosmin I Blaga, Junliang Xu, Anthony D DiChiara, Emily Sistrunk, Kaikai Zhang, Pierre Agostini, Terry A Miller, Louis F DiMauro, and C D Lin. Imaging ultrafast molecular dynamics with laser-induced electron diffraction. *Nature*, 483(7388):194–197, March 2012. doi: 10.1038/nature10820. URL `https://www.nature.com/articles/nature10820`.

[229] Jie Yang, Markus Guehr, Xiaozhe Shen, Renkai Li, Theodore Vecchione, Ryan Coffee, Jeff Corbett, Alan Fry, Nick Hartmann, Carsten Hast, Kareem Hegazy, Keith Jobe, Igor Makasyuk, Joseph Robinson, Matthew S. Robinson, Sharon Vetter, Stephen Weathersby, Charles Yoneda, Xijie Wang, and Martin Centurion. Diffractive imaging of coherent nuclear motion in isolated molecules. *Phys. Rev. Lett.*, 117:153002, October

2016. doi: 10.1103/PhysRevLett.117.153002. URL `https://link.aps.org/doi/10.1103/PhysRevLett.117.153002`.

[230] V May and O Kühn. *Charge and energy transfer dynamics in molecular systems*. Wiley-VCH, 2004.

[231] C. Y. Ng. *Vacuum Ultraviolet Photoionization and Photodissociation of Molecules and Clusters*. World Scientific Publishing Co. Pte. Ltd, 1991. ISBN 981-02-0430-2. doi: 10.1142/1244. URL `https://www.worldscientific.com/worldscibooks/10.1142/1244`.

[232] Bruce C. Garrett, David A. Dixon, Donald M. Camaioni, Daniel M. Chipman, Mark A. Johnson, Charles D. Jonah, Gregory A. Kimmel, John H. Miller, Thomas N. Rescigno, Peter J. Rossky, Sotiris S. Xantheas, Steven D. Colson, Allan H. Laufer, Douglas Ray, Paul F. Barbara, David M. Bartels, Kurt H. Becker, Kit H. Bowen, Stephen E. Bradforth, Ian Carmichael, James V. Coe, L. Rene Corrales, James P. Cowin, Michel Dupuis, Kenneth B. Eisenthal, James A. Franz, Maciej S. Gutowski, Kenneth D. Jordan, Bruce D. Kay, Jay A. LaVerne, Sergei V. Lymar, Theodore E. Madey, C. William McCurdy, Dan Meisel, Shaul Mukamel, Anders R. Nilsson, Thomas M. Orlando, Nikolay G. Petrik, Simon M. Pimblott, James R. Rustad, Gregory K. Schenter, Sherwin J. Singer, Andrei Tokmakoff, Lai-Sheng Wang, , and Timothy S Zwier. Role of water in electron-initiated processes and radical chemistry: Issues and scientific advances. *Chem. Rev.*, 105:355–390, 2005. doi: 10.1021/cr030453x. URL `https://doi.org/10.1021/cr030453x`.

[233] Dan Lubin and Elsa H. Jensen. Effects of clouds and stratospheric ozone depletion on ultraviolet radiation trends. *Nature*, 377:710–713, 1995. doi: 10.1038/377710a0. URL `https://doi.org/10.1038/377710a0`.

[234] Martin A. Barstow and Jay B. Holberg. *Extreme Ultraviolet Astronomy*. Cambridge University Press, Cambridge, 2003. doi: 10.1017/CBO9780511536144.

[235] Thomas Schultz, Elena Samoylova, Wolfgang Radloff, Ingolf V Hertel, Andrzej L Sobolewski, and Wolfgang Domcke. Efficient deactivation of a model base pair via excited-state hydrogen transfer. *Science*, 306(5702):1765–8, December 2004. ISSN 1095-9203. doi: 10.1126/science.1104038. URL `http://www.ncbi.nlm.nih.gov/pubmed/15576616`.

[236] Dominik Marx, Mark E. Tuckerman, Jürg Hutter, and Michele Parrinello. The nature of the hydrated excess proton in water. *Nature*, 397:601–604, 1999. doi: 10.1038/17579. URL `https://doi.org/10.1038/17579`.

[237] Amir Golan, Ksenia B. Bravaya, Romas Kudirka, Oleg Kostko, Stephen R Leone, Anna I. Krylov, and Musahid Ahmed. Ionization of dimethyluracil dimers leads to

facile proton transfer in the absence of hydrogen bonds. *Nat. Chem.*, 4:323–329, 2012. doi: 10.1038/nchem.1298. URL `https://doi.org/10.1038/nchem.1298`.

[238] D. A. Horke, H. M. Watts, A. D. Smith, E. Jager, E. Springate, O. Alexander, C. Cacho, R. T. Chapman, and R. S. Minns. Hydrogen bonds in excited state proton transfer. *Phys. Rev. Lett.*, 117(16):163002, October 2016. doi: 10.1103/PhysRevLett.117.163002. URL `http://link.aps.org/doi/10.1103/PhysRevLett.117.163002`.

[239] M Mudrich, A C LaForge, A Ciavardini, P O'Keeffe, C Callegari, M Coreno, A Demidovich, M Devetta, M Di Fraia, M Drabbels, P Finetti, O Gessner, C Grazioli, A Hernando, D M Neumark, Y Ovcharenko, P Piseri, O Plekan, K C Prince, R Richter, M P Ziemkiewicz, T Möller, J Eloranta, M Pi, M Barranco, and F Stienkemeier. Ultrafast relaxation of photoexcited superfluid He nanodroplets. *Nat. Commun.*, 11:112, 2020. doi: 10.1038/s41467-019-13681-6. URL `https://doi.org/10.1038/s41467-019-13681-6`.

[240] Mario Barbatti, Adélia J. A. Aquino, Jaroslaw J. Szymczak, Dana Nachtigallová, Pavel Hobza, and Hans Lischka. Relaxation mechanisms of UV-photoexcited DNA and RNA nucleobases. *PNAS*, 107(50):21453–21458, 2010. doi: 10.1073/pnas.1014982107. URL `https://www.pnas.org/content/107/50/21453`.

[241] Shenyue Xu, Dalong Guo, Xinwen Ma, Xiaolong Zhu, Wentian Feng, Shuncheng Yan, Dongmei Zhao, Yong Gao, Shaofeng Zhang, Xueguang Ren, Yongtao Zhao, Zhongfeng Xu, Alexander Dorn, Lorenz S. Cederbaum, and Nikolai V. Kryzhevoi. Damaging intermolecular energy and proton transfer processes in alpha-particle-irradiated hydrogen-bonded systems. *Angew. Chem. Int. Ed.*, 57(52):17023–17027, 2018. doi: 10.1002/anie.201808898. URL `https://onlinelibrary.wiley.com/doi/abs/10.1002/anie.201808898`.

[242] Chun-Rong Wang, Jenny Nguyen, and Qing-Bin Lu. Bond breaks of nucleotides by dissociative electron transfer of nonequilibrium prehydrated electrons: A new molecular mechanism for reductive DNA damage. *J. Am. Chem. Soc.*, 131:11320–11322, 2009. doi: 10.1021/ja902675g. URL `https://doi.org/10.1021/ja902675g`.

[243] K. Grygoryeva, J. Rakovský, Ivo Vinklárek, O. Votava, M. Fárník, , and Viktoriya Poterya. Vibrationally mediated photodissociation dynamics of pyrrole. *AIP Adv.*, 9: 0351511–0351517, 2019. doi: 10.1063/1.5091974. URL `https://aip.scitation.org/doi/pdf/10.1063/1.5091974?class=pdf`.

[244] Alrik. J. van den Brom, Makis Kapelios, Theofanis N. Kitsopoulos, N. Hendrik Nahler, BrÃd Cronin, and Michael N. R Ashfold. Photodissociation and photoionization of pyrrole following the multiphoton excitation at 243 and 364.7 nm. *Phys. Chem. Chem. Phys.*, 7:5704–899, 2005. doi: 10.1039/B415766D. URL `http://dx.doi.org/10.1039/B415766D`.

[245] Václav Profant, Viktoriya Poterya, Michal Fárník, Petr Slavíček, and Udo Buck. Fragmentation dynamics of size-selected pyrrole clusters prepared by electron impact ionization: Forming a solvated dimer ion core. *J. Phys. Chem. A*, 111:12477–12486, 2007. doi: 10.1021/jp0751561. URL `https://doi.org/10.1021/jp0751561`.

[246] Sebastian Trippel, Terry Mullins, Nele L. M. Müller, Jens S. Kienitz, Karol Długołęcki, and Jochen Küpper. Strongly aligned and oriented molecular samples at a kHz repetition rate. *Mol. Phys.*, 111:1738, 2013. doi: 10.1080/00268976.2013.780334. URL `http://dx.doi.org/10.1080/00268976.2013.780334`.

[247] A. Roberts, P. Svihra, A. Al-Refaie, H. Graafsma, J. Küpper, K. Majumdar, K. Mavrokoridis, A. Nomerotski, D. Pennicard, B. Philippou, S. Trippel, C. Touramanis, and J. Vann. First demonstration of 3D optical readout of a TPC using a single photon sensitive Timepix3 based camera. *J. Instrum.*, 14(06):P06001–P06001, June 2019. doi: 10.1088/1748-0221/14/06/p06001. URL `https://doi.org/10.1088/1748-0221/14/06/P06001`.

[248] S Hankin, D Villeneuve, P Corkum, and D Rayner. Intense-field laser ionization rates in atoms and molecules. *Phys. Rev. A*, 64(1):013405, 2001. doi: 10.1103/PhysRevA.64.013405. URL `https://doi.org/10.1103/PhysRevA.64.013405`.

[249] Joss Wiese, Jean-François Olivieri, Andrea Trabattoni, Sebastian Trippel, and Jochen Küpper. Strong-field photoelectron momentum imaging of OCS at finely resolved incident intensities. *New J. Phys.*, 21:083011, August 2019. doi: 10.1088/1367-2630/ab34e8.

[250] R. H. Page, Y. R. Shen, and Y. T. Lee. High-resolution photoionization spectrum of water molecules in a supersonic beam. *J. Chem. Phys.*, 88:5362–5376, 1988. doi: 10.1063/1.454058. URL `https://doi.org/10.1063/1.454058`.

[251] P. M. Paul, E. S. Toma, P. Breger, G. Mullot, F. Augé, Ph. Balcou, H. G. Muller, and P. Agostini. Observation of a train of attosecond pulses from high harmonic generation. *Science*, 292(5522):1689–1692, 2001. ISSN 0036-8075. doi: 10.1126/science.1059413. URL `http://science.sciencemag.org/content/292/5522/1689`.

[252] M. Hentschel, R. Kienberger, C. Spielmann, G. A. Reider, N. Milosevic, T. Brabec, P. Corkum, U. Heinzmann, M. Drescher, and F. Krausz. Attosecond metrology. *Nature*, 414:509–513, 2001. doi: 10.1038/35107000. URL `https://doi.org/10.1038/35107000`.

[253] P. B. Corkum and F. Krausz. Attosecond Science. *Nat. Phys.*, 3:381–387, 2007. doi: 10.1038/nphys620. URL `https://www.nature.com/articles/nphys620`.

[254] Thomas Schultz and Marc Vrakking, editors. *Attosecond and XUV Physics: Ultrafast Dynamics and Spectroscopy.* Wiley-VCH, Boschstr. 12, 69469 Weinheim, Germany, 1

edition, 2014. ISBN 9783527411245. doi: 10.1002/9783527677689. URL `doi.org/10.1002/9783527677689`.

[255] G Sansone, F Kelkensberg, J F Pérez-Torres, F Morales, M F Kling, W Siu, O Ghafur, P Johnsson, M Swoboda, E Benedetti, F Ferrari, F Lepine, J L Sanz-Vicario, S Zherebtsov, I Znakovskaya, A L'Huillier, M Yu Ivanov, M Nisoli, F Martín, and M J J Vrakking. Electron localization following attosecond molecular photoionization. *Nature*, 465(7299):763, 2010. doi: 10.1038/nature09084. URL `http://www.nature.com/nature/journal/v465/n7299/full/nature09084.html`.

[256] A. Baltuska, T. Udem, M. Uiberacker, M. Hentschel, E. Goulielmakis, C. Gohle, R. Holzwarth, V. S. Yakoviev, A. Scrinzi, T. W. Hänsch, and F. Krausz. Attosecond control of electronic processes by intense light fields. *Nature*, 421:611–615, 2003.

[257] M Uiberacker, Th Uphues, M Schultze, A J Verhoef, V Yakovlev, M F Kling, J Rauschenberger, N M Kabachnik, H Schröder, M Lezius, K L Kompa, H G Muller, M J J Vrakking, S Hendel, U Kleineberg, U Heinzmann, M Drescher, and F Krausz. Attosecond real-time observation of electron tunnelling in atoms. *Nature*, 446(7136): 627–632, April 2007. doi: 10.1038/nature05648. URL `http://www.nature.com/doifinder/10.1038/nature05648`.

[258] S. N. Yurchenko, S. Patchkovskii, I. V. Litvinyuk, P. B. Corkum, and G. L. Yudin. Laser-induced interference, focusing, and diffraction of rescattering molecular photoelectrons. *Phys. Rev. Lett.*, 93:223003, Nov 2004. doi: 10.1103/PhysRevLett.93.223003. URL `https://link.aps.org/doi/10.1103/PhysRevLett.93.223003`.

[259] J. Itatani, J. Levesque, D. Zeidler, H. Niikura, H. Pépin, J. C. Kieffer, P. B. Corkum, and D. M. Villeneuve. Tomographic imaging of molecular orbitals. *Nature*, 432:867–871, 2004. doi: 10.1038/nature03183. URL `https://dx.doi.org/10.1038/nature03183`.

[260] Andrea Trabattoni, Joss Wiese, Umberto De Giovannini, Jean-Francóis Olivieri, Terry Mullins, Jolijn Onvlee, Sang-Kil Son, Biagio Frusteri, Angel Rubio, Sebastian Trippel, and Jochen Küpper. Setting the photoelectron clock through molecular alignment. *Nat. Commun.*, 11:2546, May 2020. doi: 10.1038/s41467-020-16270-0. URL `https://doi.org/10.1038/s41467-020-16270-0`.

[261] B Wolter, M G Pullen, A T Le, M Baudisch, K Doblhoff-Dier, A Senftleben, M Hemmer, C D Schroter, J Ullrich, T Pfeifer, R Moshammer, S Gräfe, O Vendrell, C D Lin, and J Biegert. Ultrafast electron diffraction imaging of bond breaking in di-ionized acetylene. *Science*, 354(6310):308–312, oct 2016. doi: 10.1126/science.aah3429. URL `http://www.sciencemag.org/lookup/doi/10.1126/science.aah3429`.

[262] P. B. Corkum, M. Y. Ivanov, and J. S. Wright. Subfemtosecond processes in strong laser fields. *Annu. Rev. Phys. Chem.*, 48:387–406, 1997. doi: 10.1146/annurev.

physchem.48.1.387. URL `http://www.annualreviews.org/doi/10.1146/annurev.physchem.48.1.387`.

[263] D. T. Strickland, Y. Beaudoin, P. Dietrich, and P. B. Corkum. Optical studies of inertially confined molecular iodine ions. *Phys. Rev. Lett.*, 68:2755–2758, 1992. doi: 10.1103/PhysRevLett.68.2755. URL `https://link.aps.org/doi/10.1103/PhysRevLett.68.2755`.

[264] L. J. Frasinski, K. Codling, P. Hatherly, J. Barr, I. N. Ross, and W. T. Toner. Femtosecond dynamics of multielectron dissociative ionization by use of a picosecond laser. *Phys. Rev. Lett.*, 58(23):2424, 1987. doi: 10.1103/PhysRevLett.58.2424. URL `https://link.aps.org/doi/10.1103/PhysRevLett.58.2424`.

[265] Szczepan Chelkowski, Tao Zuo, Osman Atabek, and André D. Bandrauk. Dissociation, ionization, and coulomb explosion of H_2^+ in an intense laser field by numerical integration of the time-dependent schrödinger equation. *Phys. Rev. A*, 52:2977–2983, 1995. doi: 10.1103/PhysRevA.52.2977. URL `https://link.aps.org/doi/10.1103/PhysRevA.52.2977`.

[266] S Chelkowski and A D Bandrauk. Two-step coulomb explosions of diatoms in intense laser fields. *J. Phys. B*, 28:L723–L731, 1995. doi: 10.1088/0953-4075/28/23/004. URL `https://doi.org/10.1088%2F0953-4075%2F28%2F23%2F004`.

[267] André D. Bandrauk and Jonathan Ruel. Charge-resonance-enhanced ionization of molecular ions in intense laser pulses: Geometric and orientation effects. *Phys. Rev. A*, 59:2153–2162, 1999. doi: 10.1103/PhysRevA.59.2153. URL `https://link.aps.org/doi/10.1103/PhysRevA.59.2153`.

[268] D. Pavičić, A. Kiess, T. W. Hänsch, and H. Figger. Intense-laser-field ionization of the hydrogen molecular ions ${H_2}^+$ and ${D_2}^+$ at critical internuclear distances. *Phys. Rev. Lett.*, 94:163002, 2005. doi: 10.1103/PhysRevLett.94.163002. URL `https://link.aps.org/doi/10.1103/PhysRevLett.94.163002`.

[269] T. K. Kjeldsen, L. B. Madsen, and J. P. Hansen. Ab initio studies of strong-field ionization of arbitrarily oriented ${H_2}^+$ molecules. *Phys. Rev. A*, 74:035402, 2006. doi: 10.1103/PhysRevA.74.035402. URL `https://link.aps.org/doi/10.1103/PhysRevA.74.035402`.

[270] G. Lagmago Kamta and A. D. Bandrauk. Effects of molecular symmetry on enhanced ionization by intense laser pulses. *Phys. Rev. A*, 75:041401, 2007. doi: 10.1103/PhysRevA.75.041401. URL `https://link.aps.org/doi/10.1103/PhysRevA.75.041401`.

[271] Akiyoshi Hishikawa, Atsushi Iwamae, and Kaoru Yamanouchi. Ultrafast structural deformation of NO_2 in intense laser fields studied by mass-resolved momentum

imaging. *J. Chem. Phys.*, 111:8871–8878, 1999. doi: 10.1063/1.480233. URL `https://doi.org/10.1063/1.480233`.

[272] Masakuni Ueyama, Hirokazu Hasegawa, Akiyoshi Hishikawa, and Kaoru Yamanouchi. Concerted and sequential coulomb explosion processes of N_2O in intense laser fields by coincidence momentum imaging. *J. Chem. Phys.*, 123:154305, 2005. doi: 10.1063/1.2032988. URL `https://doi.org/10.1063/1.2032988`.

[273] Akiyoshi Hishikawa, Atsushi Iwamae, and Kaoru Yamanouchi. Ultrafast deformation of the geometrical structure of CO_2 induced in intense laser fields. *Phys. Rev. Lett.*, 83:1127–1130, 1999. doi: 10.1103/PhysRevLett.83.1127. URL `https://link.aps.org/doi/10.1103/PhysRevLett.83.1127`.

[274] Irina Bocharova, Reza Karimi, Emmanuel F. Penka, Jean-Paul Brichta, Philippe Lassonde, Xiquan Fu, Jean-Claude Kieffer, A. Bandrauk, Igor Litvinyuk, Joseph Sanderson, and F Légaré. Charge resonance enhanced ionization of CO_2 probed by laser coulomb explosion imaging. *Phys. Rev. Lett.*, 107:063201, 2011. doi: 10.1103/PhysRevLett.107.063201. URL `https://link.aps.org/doi/10.1103/PhysRevLett.107.063201`.

[275] Sonia Erattupuzha, Cody L Covington, Arthur Russakoff, Erik Lötstedt, Seyedreza Larimian, Václav Hanus, Sergiy Bubin, Markus Koch, Stefanie Gräfe, Andrius Baltuška, Xinhua Xie, Kaoru Yamanouchi, Kálmán Varga, and Markus Kitzler. Enhanced ionisation of polyatomic molecules in intense laser pulses is due to energy upshift and field coupling of multiple orbitals. *J. Phys. B*, 50(12):125601, 2017. doi: 10.1088/1361-6455/aa7098. URL `https://doi.org/10.1088%2F1361-6455%2Faa7098`.

[276] C Cornaggia. Electronic dynamics of charge resonance enhanced ionization probed by laser-induced alignment in C_2H_2. *J. Phys. B*, 49:19LT01, 2016. doi: 10.1088/0953-4075/49/19/19lt01. URL `https://doi.org/10.1088%2F0953-4075%2F49%2F19%2F19lt01`.

[277] Xinhua Xie, Stefan Roither, Markus Schöffler, Huailiang Xu, Sergiy Bubin, Erik Lötstedt, Sonia Erattuphuza, Atsushi Iwasaki, Daniil Kartashov, Kálmán Varga, Gerhard G. Paulus, Andrius Baltuška, Kaoru Yamanouchi, and Markus Kitzler. Role of proton dynamics in efficient photoionization of hydrocarbon molecules. *Phys. Rev. A*, 89:023429, 2014. doi: 10.1103/PhysRevA.89.023429. URL `https://link.aps.org/doi/10.1103/PhysRevA.89.023429`.

[278] Erik Lötstedt, Tsuyoshi Kato, and Kaoru Yamanouchi. Enhanced ionization of acetylene in intense laser fields. *Phys. Rev. A*, 85:041402, 2012. doi: 10.1103/PhysRevA.85.041402. URL `https://link.aps.org/doi/10.1103/PhysRevA.85.041402`.

[279] Erik Lötstedt, Tsuyoshi Kato, and Kaoru Yamanouchi. Efficient ionization of one-dimensional acetylene investigated by time-dependent hartree-fock calculations. *Phys. Rev. A*, 86:023401, 2012. doi: 10.1103/PhysRevA.86.023401. URL `https://link.aps.org/doi/10.1103/PhysRevA.86.023401`.

[280] Arthur Russakoff, Sergiy Bubin, Xinhua Xie, Sonia Erattupuzha, Markus Kitzler, and Kálmán Varga. Time-dependent density-functional study of the alignment-dependent ionization of acetylene and ethylene by strong laser pulses. *Phys. Rev. A*, 91:023422, 2015. doi: 10.1103/PhysRevA.91.023422. URL `https://link.aps.org/doi/10.1103/PhysRevA.91.023422`.

[281] K. Boyer, B. D Thompson, A. McPherson, and C. K Rhodes. Evidence for coherent electron motions in multiphoton x-ray production from Kr and Xe clusters. *J. Phys. B*, 27(18):4373–4389, 1994. doi: 10.1088/0953-4075/27/18/030. URL `https://doi.org/10.1088%2F0953-4075%2F27%2F18%2F030`.

[282] Melby Johny, Constant A. Schouder, Ahmed Al-Refaie, Lanhai He, Joss Wiese, Henrik Stapelfeldt, Sebastian Trippel, and Jochen Küpper. Water as radiation protection agent for ionized pyrrole, 2020. URL `https://arxiv.org/pdf/2010.00453.pdf`. submitted.

[283] P. J. Linstrom and W. G. Mallard, editors. *NIST Chemistry WebBook, NIST Standard Reference Database Number 69*. National Institute of Standards and Technology, Gaithersburg MD, 20899, May 2017. doi: 10.18434/T4D303. URL `http://webbook.nist.gov`.

[284] Gilad Marcus, Wolfram Helml, Xun Gu, Yunpei Deng, Robert Hartmann, Takayoshi Kobayashi, Lothar Strueder, Reinhard Kienberger, and Ferenc Krausz. Sub-femtosecond K-shell excitation with a few-cycle infrared laser field. *Phys. Rev. Lett.*, 108(2):023201, 2012. doi: 10.1103/physrevlett.108.023201. URL `https://doi.org/10.1103/physrevlett.108.023201`.

[285] Yunpei Deng, Zhinan Zeng, Zhengmao Jia, Pavel Komm, Yinhui Zheng, Ge Xiaochun, Ruxin Li, and Gilad Marcus. Ultrafast excitation of an inner-shell electron by laser-induced electron recollision. *Phys. Rev. Lett.*, 116:073901, 2016. doi: 10.1103/physrevlett.116.073901. URL `https://doi.org/10.1103/physrevlett.116.073901`.

[286] Nagitha Ekanayake, Travis Severt, Muath Nairat, Nicholas P. Weingartz, Benjamin M. Farris, Balram Kaderiya, Peyman Feizollah, Bethany Jochim, Farzaneh Ziaee, Kurtis Borne, Kanaka Raju P., Kevin D. Carnes, Daniel Rolles, Artem Rudenko, Benjamin G. Levine, James E. Jackson, Itzik Ben-Itzhak, and Marcos Dantus. H_2 roaming chemistry and the formation of H_3^+ from organic molecules in strong laser fields. *Nat. Commun.*,

9(1):1–11, 2018. doi: 10.1038/s41467-018-07577-0. URL `https://doi.org/10.1038/s41467-018-07577-0`.

[287] Osama Mohamad, Brock .J Sishc, Janapriya Saha, Arnold Pompos, Asal Rahimi, Michael Story, Anthony Davis, and D.W. Kim. Carbon ion radiotherapy: A review of clinical experiences and preclinical research, with an emphasis on DNA damage/repair. *Cancers*, 9(12):66, 2017. doi: 10.3390/cancers9060066. URL `https://doi.org/10.3390/cancers9060066`.

[288] Terry Mullins, Evangelos T. Karamatskos, Joss Wiese, Jolijn Onvlee, Andrey Yachmenev, Arnaud Rouzée, Sebastian Trippel, and Jochen Küpper. Toward three-dimensional field-free alignment of arbitrary asymmetric top molecules, 2020. in preparation.

[289] P. B. Corkum, C. Ellert, M. Mehendale, P. Dietrich, S. Hankin, S. Aseyev, D. Rayner, and D. Villeneuve. Molecular science with strong laser fields. *Faraday Disc.*, 113: 47–59, 1999. URL `http://dx.doi.org/10.1039/a903428e`.

[290] Xinhua Xie, Katharina Doblhoff-Dier, Huailiang Xu, Stefan Roither, Markus S. Schöffler, Daniil Kartashov, Sonia Erattupuzha, Tim Rathje, Gerhard G. Paulus, Kaoru Yamanouchi, Andrius Baltuška, Stefanie Gräfe, and Markus Kitzler. Selective control over fragmentation reactions in polyatomic molecules using impulsive laser alignment. *Phys. Rev. A*, 112:163003, 2014. doi: 10.1103/PhysRevLett.112.163003. URL `https://link.aps.org/doi/10.1103/PhysRevLett.112.163003`.

[291] Jens Viefhaus, Frank Scholz, Sascha Deinert, Leif Glaser, Markus Ilchen, Joern Seltmann, Peter Walter, and Frank Siewert. The variable polarization XUV beamline P04 at PETRA III: Optics, mechanics and their performance. *Nucl. Instrum. Meth. A*, 710:151–154, 2013. doi: 10.1016/j.nima.2012.10.110. URL `http://www.sciencedirect.com/science/article/pii/S0168900212012831`.

[292] L Strüder, Sascha Epp, Daniel Rolles, Robert Hartmann, Peter Holl, Gerhard Lutz, Heike Soltau, Rouven Eckart, Christian Reich, Klaus Heinzinger, Christian Thamm, Artem Rudenko, Faton Krasniqi, K Kühnel, Christian Bauer, Claus-Dieter Schroeter, Robert Moshammer, Simone Techert, Danilo Miessner, Matteo Porro, Olaf Haelker, Norbert Meidinger, Nils Kimmel, Robert Andritschke, Florian Schopper, Georg Weidenspointner, Alexander Ziegler, Daniel Pietschner, Sven Herrmann, Ullrich Pietsch, Albert Walenta, Wolfram Leitenberger, Christoph Bostedt, Thomas Moeller, Daniela Rupp, Marcus Adolph, Heinz Graafsma, Helmut Hirsemann, Klaus Gaertner, Rainer Richter, Lutz Foucar, Robert L Shoeman, Ilme Schlichting, and Joachim Ullrich. Large-format, high-speed, x-ray pnccds combined with electron and ion imaging spectrometers in a multipurpose chamber for experiments at 4th generation light sources. *Nucl. Instrum. Meth. A*, 614(3):483–496, Jan 2010. doi: 10.1016/j.nima.2009.12.053.

[293] Utuq Ablikim, Cédric Bomme, Timur Osipov, Hui Xiong, Razib Obaid, René C. Bilodeau, Nora G. Kling, Ileana Dumitriu, Sven Augustin, Shashank Pathak, Kirsten Schnorr, David Kilcoyne, Nora Berrah, and Daniel Rolles. A coincidence velocity map imaging spectrometer for ions and high-energy electrons to study inner-shell photoioinization of gas-phase molecules. *Rev. Sci. Instrum.*, 90(5):055103, 2019. doi: 10.1063/1.5093420. URL `https://doi.org/10.1063/1.5093420`.

[294] S. Trippel. XFEL beamtime report: Charge transfer and photofragmentation in hydrogen bonded pyrrole-water clusters upon site-specific x-ray photoionization, 2019.

[295] J Ullrich, R Moshammer, R Dörner, O Jagutzki, V Mergel, H Schmidt-Böcking, and L Spielberger. Recoil-ion momentum spectroscopy. *J. Phys. B*, 30(13):2917–2974, jul 1997. doi: 10.1088/0953-4075/30/13/006. URL `http://iopscience.iop.org/article/10.1088/0953-4075/30/13/006`.

Acronyms

ATI above threshold ionization.

CCD charge-coupled device.

CEI Coulomb explosion imaging.

CFEL centre for free-electron laser science.

CMOS complementary metal-oxide-semiconductor.

DNA Deoxyribonucleic acid.

ETMD electron-transfer mediated decay.

EuXFEL European XFEL.

FEL free-electron laser.

FWHM full width half maximum.

HOMO highest occupied molecular orbital.

ICD interatomic Coulombic decay.

IP ionization potential.

IR infrared.

LCLS Linac Coherent Light source.

LIED laser-induced electron diffraction.

MCP micro-channel plate.

MFPAD Molecular-Frame Photo Angular Distributions.

PEPIPCO Photoelectron-Photoion-Photoion Coincidence.

PETRA III Positron-Electron Tandem Ring Accelerator 3rd generation synchrotron source.

PIPICO Photoion Photoion coincidence.

PTMCS proton-transfer mediated charge separation.

RFPAD Recoil-Frame Photo Angular Distributions.

SPIDER	Speedy PIxel Detector Readout.
TOF-MS	time-of-flight mass spectra.
UV	ultraviolet.
VMIS	velocity map imaging spectrometer.

Acknowledgments

Within these years of my doctoral research, I enjoyed all the opportunities to expand my knowledge. It may take some time to realize how situations and people can be impactful in a person's life and future. Herewith, I would like to thank all the people who supported me in one or another way during this thesis, and I am deeply grateful to all of them.

First of all, I would like to thank my supervisor, Jochen Küpper, for providing me an opportunity to perform my doctoral research in the Controlled Molecule Imaging group (CMI) at the Center for Free-Electron Laser Science (CFEL). I thank him for his active participation and support in all scientific projects, in the form of valuable ideas, critical discussions on how to improve the experiments, data analysis, or manuscript writing. I really appreciate for trusting me and the opportunities given to spend time abroad for scientific collaborations.

I want to thank Guiseppe Sansone for being my second supervisor and for all the support during this time. You were always encouraging and motivating whenever I met you either in MEDEA meetings or conferences. Furthermore, I want to thank all the members of my dissertation committee.

Next, I would like to thank the European Union project 'Molecular Electron Dynamics investigated by IntensE Fields and Attosecond Pulses' (MEDEA) for funding my salary and travel support for three years. The MEDEA network provided a platform to meet a lot of brilliant minds, professors and researchers, and to be introduced to a large number of technical and scientific subjects.

My special thanks go to Sebastian Trippel. His scientific expertise and laboratory skills are impressive, and I am very privileged to work under his guidance and to learn from him. I enjoyed very much all the fruitful scientific discussions, experiments, data analysis, preparing manuscripts, and of course, all exhausting beam times. I am extremely thankful for all the help and support you provided during my tough times. It was fun working with you, and you nailed it many times by bringing ice creams and beers to motivate me to work during the last moment beam preparations !!.

Another person whom I am grateful for is Jolijn Onvlee. You are smart, a good scientist, and a very good collaborator, and I have learned a lot from you, through scientific discussions and all sorts of guidance while writing. Thank you very much for proofreading manuscripts and the thesis. Your support was immense during my tough times. Other big thanks go to Thomas Kierspel, who introduced me to the FEL molbeam machine and the beam time experiments. I would like to acknowledge the nice bunch of people whom I got a chance to work with as well as for all helpful discussions and feedback: Thomas Kierspel, Jolijn Onvlee, Joss Wiese, Helen Bieker, Lanhai He, Ahmed Al-Refaie, Thomas Sharples, Terry Mullins. A special mention to Helen Bieker for all the help and nice times I had with you, especially the Yosemite trip and lunch meetings. Thanks, Nicole Teschmidt, for being my chai partner and good friend, when I felt like an alien in the very beginning. I would also like to thank all the Ph.D. co-strugglers in CMI for a wonderful time. Thank you, Karol Długołęcki, for all technical support during the machine setup and during many beamtimes. I want to thank Stefanie Kerbstadt for proofreading chapters of my thesis and translation of the abstract into the german version. Also, I want to thank Mathew Robinsson for your comments on my thesis. All past and present members of CMI, thanks for being great people to work with as well as providing wonderful memories that I would not forget. I would like to thank Barbora for her amazing support.

Additionally, I would like to thank Henrik Stapelfedt for providing me chance to perform a secondment in his lab and for the fruitful discussions. Also, would like to thank all members of Femtolab, Aarhus for the nice hospitality during my two months visit and awesome π o'clock coffee breaks. A special thanks to Constant Schouder, with whom I performed the Timepix experimental campaign and the collaboration was very inspiring. Thanks to Constant Schouder, Bjarke Hübschmann, and Adam Chatterley for their efforts to share insights into the He-nano droplet machine and alignment techniques. Also, I would like to thank all the beamtime collaborators.

For the amazing friendship and keeping me sane all this time, I want to say a big shout out to my friends: Sreevi, Vandana, Ajay, Noby, Gabriella, Fernando, Gudrun, Aghul, Ankita, Ananya, Disha, Viji, and Haritha.

A very special thanks to my family, whom I missed very much during the past 4.5 years. I love you so much. My parents, Valsamma and Johny, provided wings to dreams and always stood for me. My siblings, Alphy and Elvis, thanks for everything, and always talking to me on every weekend and let us keep the spirit of leg-pulling forever.

Last but not least, I want to thank Mathews Tharian Deepak for being with me. You are always a good listener and have smart ideas to get rid of my stress and make me happy. Thanks for never complaining about my universal excuse, 'I am stressed about my Ph.D' for my laziness of making plans for our wedding or simply any plans.

List of publications

Publications related to this thesis:

2020 *Molecular sunscreen: water protects pyrrole from radiation damage*
Melby Johny, Constant Schouder, Ahmed Al-Refaie, Joss Wiese, Lanhai He, Henrik Stapelfeldt, Sebastian Trippel, and Jochen Küpper
to be resubmitted (2020), *arXiv*:2010.00453.

2020 *Observation of an enhanced core-shell ionization in pyrrole*(H_2O) *dimer in the strong-field regime*
Melby Johny, Constant Schouder, Ahmed Al-Refaie, Joss Wiese, Henrik Stapelfeldt, Sebastian Trippel, and Jochen Küpper
in preparation (2020)

2019 *PymePix: a python library for SPIDR readout of Timepix3*
Ahmed Al-Refaie, **Melby Johny**, Jonathan Correa, David Pennicard, Peter Svihra, Andrei Nomerotski, Sebastian Trippel, and Jochen Küpper
Journal of Instrumentation **14**, P10003 (2019), *arXiv*:1905.07999.

2019 *Spatial separation of pyrrole and pyrrole-water clusters*
Melby Johny, Jolijn Onvlee, Thomas Kierspel, Helen Bieker, Sebastian Trippel, and Jochen Küpper
Chemical Physics Letters **721**, 149 (2019), *arXiv*:1901.05267

2018 *Knife edge skimming for improved separation of molecular species by the deflector*
Sebastian Trippel, **Melby Johny**, Thomas Kierspel, Jolijn Onvlee, Helen Bieker, Hong Ye, Terry Mullins, Lars Gumprecht, Karol Długołęcki, and Jochen Küpper
Review of Scientific Instruments **89**, 096110 (2018), *arXiv*:1802.04053

Other publications I have contributed during my PhD study:

2020 *Photophysics of pure water dimer following strong-field ionization*
Helen Bieker, Jolijn Onvlee, **Melby Johny**, Sebastian Trippel, Daniel Horke, and Jochen Küpper
in preparation (2020)

2020 *COMO: the Permanent Endstation for Cooled Dense and Long-Pulsed Molecular Beam Source at the European X-ray Free-Electron Laser*
Lanhai He, **Melby Johny**, Thomas Kierspel, Sebastian Trippel, and Jochen Küpper
in preparation (2020)

2020 *Spatial Separation of Methanol and Methanol Dimer through Stark Deflection*
Thomas R. Sharples, **Melby Johny**, Helen Bieker, Martin J. Paterson, Sebastian

Trippel, and Jochen Küpper
in preparation (2020)

2020 *Laser-induced Coulomb explosion imaging of $C_6H_5Br_2$ and C_6H_5Br-I_2 dimers in Helium nanodroplets*
Constant Schouder, Bjarke Hübschmann, Adam S. Chatterley, **Melby Johny**, Ahmed Al-Refaie, Florent Calvo, Jochen Küpper, and Henrik Stapelfeldt
in preparation (2020)

2020 *Time-Resolved Relaxation and Fragmentation of Polycyclic Aromatic Hydrocarbons Investigated in the Ultrafast XUV-IR Regime*
Jason W. L. Lee, *et. int.*, (41 authors), and Melanie Schnell
under review (2020)

2019 *Pure Molecular Beam of Water Dimer*
Helen Bieker, Jolijn Onvlee, **Melby Johny**, Lanhai He, Thomas Kierspel, Sebastian Trippel, Daniel Horke, and Jochen Küpper
The Journal of Physical Chemistry A **123**, 37486 (2019), *arXiv*:1904.08716

Other publication:

2017 *Modulating the Phe–Phe dipeptide aggregation landscape via covalent attachment of an azobenzene photoswitch*
Melby Johny, Kanchustambham Vijayalakshmi, Ankita Das, Palas Roy, Aseem Mishra, and Jyotishman Dasgupta
Chemical Communications **53**, 9348 (2017)

Eidesstattliche Versicherung / Declaration on oath

Hiermit versichere ich an Eides statt, die vorliegende Dissertationschrift selbst verfasst und keine anderen als die angegebenen Hilfsmittel und Quellen benutzt zu haben.

Die eingereichte schriftliche Fassung entspricht der auf dem elektronischen Speichermedium.

Die Dissertation wurde in der vorgelegten oder einer ähnlichen Form nicht schon einmal in einem früheren Promotionsverfahren angenommen oder als ungenügend beurteilt.

Hamburg, den 04.12.2020 Unterschrift: ______________________

Melby Johny